Doctoral Dissertation

Study on Generation Mechanism of Rogue Wave Phenomenon in Optical Fiber Based on Soliton's Eigenvalue

Rambukwelle Weerasekara Mudiyanselage Gihan Kanishka Bandara Weerasekara

January 2017

Department of Electrical, Electronic and Information Engineering
Graduate School of Engineering
Osaka University

All that is necessary for faith is the belief that by doing our best we shall come nearer to success and that success in our aims.....is worth attaining.

– Rosalind Elsie Franklin
(U. K. chemist and X-ray crystallographer, 1920–1958)

Preface

Randomly generated extraordinary amplitude nonlinear wave in fluid dynamics can be characterized by rogue waves. An optical analog of oceanic rogue waves, so-called optical rogue waves, were firstly observed inside optical fibers in 2007. Since the publication of a pioneering paper by Solli *et al.* in 2007, investigations of optical rogue waves have become increasingly common and have formed the basis for a new subfield in optics. In practical situations, large undesired fluctuations have been found in case of generating optical rogue waves, which are quite difficult to suppress using external means. Optical rogue waves are characterized by their " L-shaped " statistics, reflecting the fact that most waves have low amplitudes, but high-amplitude waves can also form with low probability.

Because of the nonlinear process called modulational instability (MI), a perturbed continuous wave (CW) is divided into a pulse train containing higher-order solitons while propagating inside anomalous dispersion fiber. Moreover, when third-order dispersion (TOD) exists, generated higher-order solitons split into quasi-solitons, which correspond to the multiple eigenvalues of the higher-order soliton and dispersive waves. Quantitative description has been undertaken in this study for generating optical rogue waves from soliton collision and fusion.

This dissertation presents a study of optical rogue wave phenomena generated in optical fiber using soliton's eigenvalues. The thesis contents are based on research the author conducted during a doctoral course at the Department of Electrical, Electronic and Information Engineering, Osaka University, Japan. This dissertation is organized as explained below.

Chapter 1 presents a general introduction of the dissertation, with explanation of the background and the purpose of this study. In recent years, research on rogue wave has been conducted actively in various fields including light waves other than hydrodynamic context. In this framework, the motivation of this work is clarified. The aim of the research is also explained.

In Chapter 2, the fundamental concepts related to optical rogue waves are presented. Concepts of optical solitons such as fundamental and higher-order soliton solutions are discussed at the beginning of this chapter. MI is discussed as a main nonlinear phenomenon initiating optical rare and strong events inside optical fiber. Soliton fission, fusion, and collision processes are described to inspire ideas of such concepts. An eigenvalue equation associated with nonlinear Schrödinger equation (NLSE) is discussed as an evaluation method for optical rogue wave generation.

Chapter 3 is devoted to characterization of optical rogue waves for an NLSE-based model. After brief discussion of the generation of optical rogue waves in the NLSE-based model, effects of TOD for optical rogue wave generation are demonstrated numerically. The optical rogue wave generation mechanism for the NLSE-based model is evaluated by using the eigenvalues of the solitons. Finally, the stability of solitons against TOD is demonstrated numerically as a proof-of-

evaluation.

In Chapter 4, soliton collision generated optical rogue waves for a higher-order NLSE (HNLSE) based model is demonstrated. TOD can be considered within an integrable framework for this model. An eigenvalue equation associated with HNLSE is solved to evaluate the soliton collision behavior. Numerical demonstrations of the effects of TOD on optical rogue wave generation for the HNLSE-based model are conducted using the achieved numerical peak power calculations and eigenvalue evaluations. Generation mechanisms of optical rogue waves for a wider TOD parameter range are demonstrated for the HNLSE-based model. Numerical demonstrations of the stability of solitons for the HNLSE-based model are conducted at the end of this chapter.

Chapter 5 examines the concept of soliton fusion phenomenon and discusses the dependency on the initial soliton pulse parameters. After introducing the fundamental concepts, the effects of temporal spacing and frequency separation for soliton fusion are demonstrated. Next, the effects of frequency separation and phase difference for soliton fusion are demonstrated. Fusion events for different soliton parameters are presented to inspire brief ideas. The authenticity assessment of numerical simulation results is discussed before the conclusion. Finally, the achieved soliton parameter range for soliton fusion phenomena is summarized.

Finally, Chapter 6 presents conclusions reached from the results and implications of the entire thesis, with a summary of all results.

All results presented in this dissertation have been published in OSA Optics Express, Elsevier Optics Communications, Advanced Optics 2014, Nonlinear Photonics 2015, OptoElectronics and Communication Conference (OECC 2016), and domestic conferences in Japan, which are presented in the list of publications.

Rambukwelle Weerasekara Mudiyanselage
Gihan Kanishka Bandara Weerasekara

Osaka, Japan
January 2017

Acknowledgments

This research was conducted during my tenure of the doctoral course at the Division of Information and Communications Technology, in Department of Electrical, Electronic and Information Engineering, Graduate School of Engineering, Osaka University, under the supervision of Prof. Akihiro Maruta.

First, I would like to express my deepest appreciation to Prof. Akihiro Maruta for his professional instruction, continual encouragement, stimulating discussions, and overall kindness during my studies in Japan. His keen insight and creative ideas have always indicated pertinent ways to construct the framework supporting this research. I have learned many valuable things though my collaboration with him, all of which have helped me to build a strong foundation for my future career. His brilliance and guidance have played a crucially important role on the realization of this work. I will always admire and respect him. It is difficult to imagine a better supervisor for my Ph.D. studies.

I am deeply grateful to emeritus Prof. Ken-ichi Kitayama and former Assistant Prof. Yuki Yoshida of the Department of Electrical, Electronic and Information Engineering, Graduate School of Engineering, Osaka University for unceasingly providing me with sufficient scientific background and advice related to my research, spending their time on carefully listening to my presentations, and helping me tremendously at every step forward. I will always be indebted to them for their patience and support.

Special thanks are extended also to Prof. Kyo Inoue and Associate Prof. Tomoo Ushio of the Department of Electrical, Electronic and Information Engineering, Graduate School of Engineering, Osaka University for accepting their roles as official reviewers of this thesis. Their immeasurable knowledge and experience have added significantly to the credibility of this work.

I am greatly indebted to Prof. Seiichi Sampei, Prof. Tetsuya Takine, Prof. Noboru Babaguchi, Prof. Atsuko Miyaji, and Prof. Takashi Washio of the Department of Electrical, Electronic and Information Engineering, Graduate School of Engineering, Osaka University. All academic lectures and invaluable guidance at the Department of Electrical, Electronic and Information Engineering, Graduate School of Engineering, Osaka University have helped me to construct the framework for this research. In addition, special thanks go to Associate Prof. Koji Igarashi, of the Division of Electrical, Electronic and Information Engineering, Graduate School of Engineering, Osaka University for all the thoughtful and pertinent comments that I received related to my research at any chance presented.

I express my sincere appreciation to the lecturers of the Department of Electrical, Electronic and Information Engineering, Graduate School of Engineering, Osaka University. I am also grateful to Dr. Marc Eberhard, a lecturer at Aston University of the UK, for his collaboration

and inspiring discussions. He gave me helpful and valuable suggestions based on his wealth of experience in nonlinear optics. This work was partially supported by λ-reach project conducted by the National Institute of Information and Communications Technology, Japan and collaborative research with Mitsubishi Electric Corporation. I am greatly thankful for those projects.

I extend my gratitude to all past and present colleagues of the Photonic Network Laboratory of the Division of Information and Communications Technology in the Department of Electrical, Electronic and Information Engineering, Graduate School of Engineering, Osaka University. They have always offered me encouragement and friendship both in research and private life. Special thanks also go to Dr. Takahiro Kodama, Mr. Naohide Kamitani, Mr. Akihiro Tokunaga, Dr. Ryosuke Matsumoto, Dr. Nikolaos Panteleimon, Dr. Masaki Shiraiwa, Mr. Hiroki Terauchi, Mr. Masaya Nakazawa, and Mr. Daisuke Hisano, who provided me with valuable suggestions, and who devoted much time to me in fruitful discussions. Among all colleagues, my deepest appreciation is dedicated to Mr. Akihiro Tokunaga. He has always given me professional instruction, constant encouragement, and many valuable discussions. I have learned many valuable things through my collaboration with him. Particularly, I thank our former secretary Ms. Ai Yamamoto for her patience and support.

I wish also to acknowledge the Ministry of Education, Culture, Sports, Science, and Technology (MEXT), Japan for funding my studies in Japan for seven years. I am as profoundly indebted to the Nikki Saneyoshi and Kato Asao Scholarship Foundations for their financial support and for making the realization of this thesis possible.

In addition, I would like to thank my family and all friends that I made over the years during my studies in Japan, both inside and outside of the scientific community, for making this thesis experience more pleasant and enjoyable. Their company and support was helpful to face the challenges and stress. Eventually it gave me the confidence and the stamina to complete the doctoral course. Particularly, I would like to thank Mr. Akalanka Silva for accepting my requests to review my English drafts without hesitation, and my wife Dayalini Weerasekara for her sincere support, patience, and understanding, which have empowered me to complete this thesis.

Finally, I would like to dedicate this thesis to my mother Pushpa Weerasekara and my father Upali Weerasekara, my wife Dayalini Weerasekara, and my two sisters Chathurka and Helanka Weerasekara for their unwavering love, patience, and support throughout my life. They have been sources of great strength, enabling me to complete this work.

Contents

Chapter 1

Introduction

1.1 Rogue Wave Phenomenon

Rogue waves are a wave phenomenon that is localized temporally and spatially, exhibiting waves of extraordinary amplitude far beyond that of background waves. The phenomenon itself has received a great deal of attention because of its emergence in various fields, ranging from fluid dynamics and oceanography. Existence of rogue waves or the freak wave stories encountered with the unexpected and unusually large waves in the ocean have been proffered and shared among seafarers for many years. After being ignored or dismissed for decades, rogue waves have emerged as dominant oceanographic research subject. The current literature includes various conjectured mechanisms aimed at explaining some factors underlying the occurrence of rogue waves. Rogue waves might appear for a multiplicity of reasons. Indeed, no universally accepted definition for rogue waves exists [1]. Rogue waves in the ocean reach around 30 meters height. Such huge waves will sink ships during their voyages. Such disasters occur worldwide, not only shallow and deep water, but also in coastal areas [1], where rogue waves can cause floods suddenly.

Rogue waves represent a frightening and life-threatening phenomenon for seafarers. Many cases have been reported of such waves striking passenger ships, container ships, oil tankers, fishing boats, and offshore and coastal structures, sometimes with catastrophic consequences. It is believed that more than 22 ships have been lost solely because of rogue waves between 1969 and 1994, as presented in Fig. 1.1 [2], [3]. On April 16, 2005, the cruise ship Norwegian Dawn, sailing through moderately choppy waters off the southeastern U. S. coast in a waning storm, was hit suddenly by a colossal wave more than 20 meters height. The huge wave loomed unexpectedly from the ocean's surface, and hammered the ship as presented in Fig. 1.2. The wave pressure damaged several windows on the ninth and tenth decks. Several decks were flooded. Nevertheless, the extensive damage was not life-threatening in this incident: four passengers were injured slightly.

Moreover, more than 131 cases of rogue wave disasters have been reported during 2006–2010 [5]. Unfortunately, events associated with loss of life and damage are also included among these reports. Among the 131 cases of disasters, maximum peak power exceeded twice the significant wave power in 78 cases. Significant wave power is the mean peak power of the highest third of the detected peak power of some point [6]. In nonlinear theory of the hydrodynamic context,

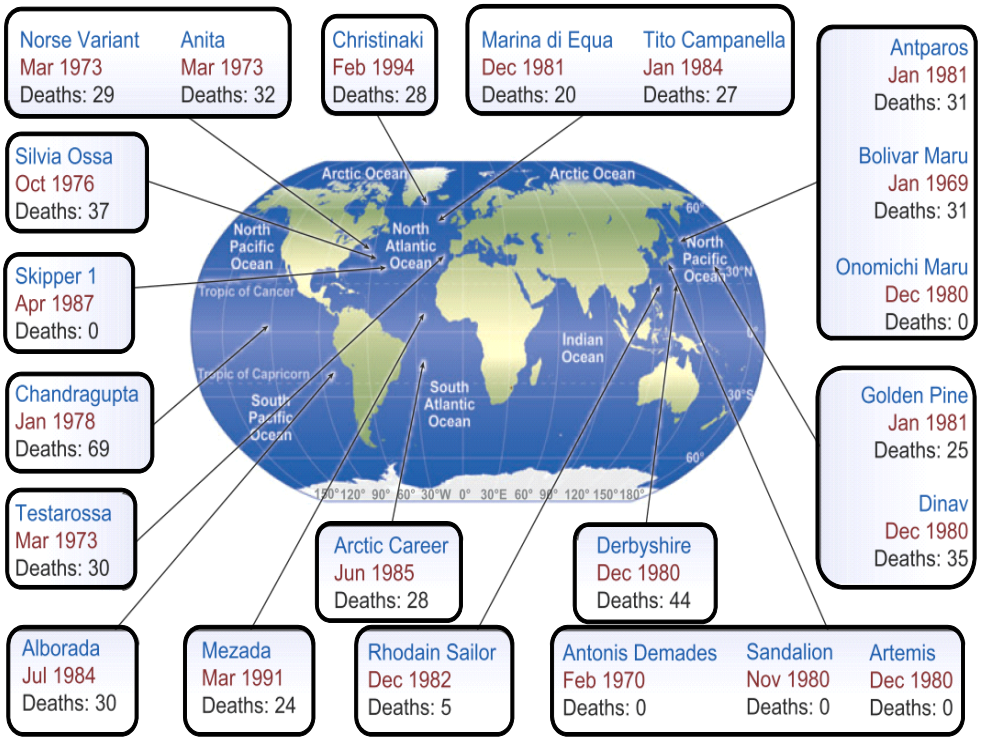

Fig. 1.1: Locations of 22 ships presumed lost after collisions with rogue waves between 1969 and 1994 (in Ref. [3]).

Fig. 1.2: Damaged cruise ship (in Ref. [4]).

the waves grow exponentially by Benjamin–Feir instability [7]. Growth of instability increases exponentially in the initial state. It then saturates with continued pulse development and finally attenuates to the initial state. In other words, in the nonlinear theory of the conservative systems, all waves invariably appear from nowhere and disappear without any trace. Zakharov has reported that a nonlinear Schrödinger equation (NLSE) is useful to represent wave phenomena in the deep sea, showing also that solitons can exist even in the deep sea [8].

Research of rogue wave phenomena has been conducted actively in various fields outside of the

hydrodynamic context, including light wave research, since the publication of a pioneering paper by Solli *et al.* [9]. Rogue waves in optics were observed when analyzing supercontinuum (SC) generation in fiber systems, which launched a new subfield in optics. Optical rogue waves share the main characteristics of oceanic rogue waves. In SC generation, the initial light in a narrow band of frequencies converted into ultra-broadband light. According to pioneering measurements by Solli *et al.* [9], temporally and spatially localized extraordinary high-amplitude peaks different from the average background level in the chaotic spectrum were observed as the first step. An area of broad interest has emerged among studies of this quickly emerged novel subject: analyzing optical rogue waves. Rogue waves can be generated by several mechanisms. Soliton collision and fusion generated optical rogue waves are mainly emphasized [10]– [13]. Collision of Akhmediev breather (AB)s [14] and wave turbulence [14], [15] are also regarded as optical rogue wave generation mechanisms. Soliton solutions and ABs are two well-known classes of solutions of NLSE [16]. Wave turbulence is a classical nonlinear phenomenon observed in various physical systems [17], dealing with the statistical behavior of numerous weakly interacting waves with random phases. Moreover, Peregrine solitons [18] and Kuznetsov–Ma solitons [19], [20] have been reported as prototypes to describe optical rogue waves. The Peregrine soliton and the Kuznetsov–Ma solitons are also the analytical solutions of the NLSE. Peregrine soliton can also be seen as the limiting case of the space–periodic AB when the period tends to infinity. On the other hand, the Peregrine soliton can also be seen as the limiting case of the time–periodic Kuznetsov–Ma soliton when the period tends to infinity. Recently, these soliton solutions have been found in various nonlinear evolution equations [21], [22]. The strict definition of rogue waves remains an open question. The mean height of the highest third of detected optical intensities is called the significant wave height (SWH). Recently, SWH is used to define optical rogue wave phenomena in many technical papers. Wave events of amplitude greater than twice the SWH are qualified by the extreme wave criterion [23].

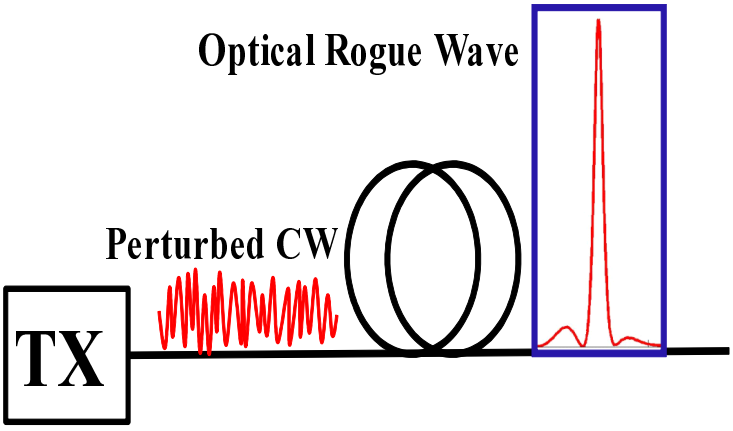

Fig. 1.3: Basic concept of optical rogue wave generation.

Modulational instability (MI) is a main nonlinear phenomenon generating optical rare and strong events inside optical fiber [24]. MI itself, a complex nonlinear process exhibiting emergent behavior and strong sensitivity to initial conditions [25], [26], plays a central role in the appearance of rogue waves in many optical scenarios [26]– [27]. Anomalous events nevertheless

arise because of sensitivity to the initial conditions. As portrayed schematically in Fig. 1.3, when some perturbed continuous wave (CW) is launched as the initial waveform into an anomalous dispersion fiber, a localized wave is formed because of MI. In the case of SC generation [28]– [30], rogue waves can appear as rare solitons, possessing anomalously large red-shifted energy and peak intensity. Because of MI, perturbed CW is divided into pulse train contained higher-order soliton in anomalous dispersion fiber. Moreover, when third-order dispersion (TOD) exists, a generated higher-order soliton will split into quasi-solitons corresponding to multiple eigenvalues of the higher-order soliton and dispersive waves. Convective effects caused by TOD play a major role in the interplay between linear and nonlinear effects in the formation of extraordinary optical intensities. Higher-order linear and nonlinear terms engender influence on optical rogue waves in strong manner. Presence of TOD in optical fibers turns the system to be unstable and generate optical rogue waves. Detailed descriptions related to MI are presented in chapter 2.

In practical situations, large undesirable fluctuations are found when generating optical rogue waves. They are quite difficult to suppress through external means. The probability density function (PDF) constructed by chaotic wave field, in optics is analogous to the “ L-shaped ” PDF of network traffic distribution. Most waves have low amplitudes, but high-amplitude waves can also form with low probability, as represented by “ L-shaped ” statistics. Early detection of a rogue wave phenomenon gives remarkable value to escape from disasters. Storms and typhoons allow advance prediction by a few days or a few hours. Nevertheless, unfortunately, the science of rogue waves in optics has supported prediction by only a few seconds until recently. Recent studies in optics have confirmed some situations and generation mechanisms of optical rogue waves. Related studies have emerged as an area of broad interest to researchers [31]. Analogy between localized structures in optics and extreme waves on the ocean has opened up many avenues for exploration and inspiration. There is now an effort underway worldwide to study these extreme events in optics.

1.2 Research Trends of Rogue Waves in Various Fields

The initial idea of optical rogue waves in the process of SC generation has expanded and enriched by new approaches. Recently optical rogue waves have been discovered in lasers, appearing in wide aperture cavities, in plasmas and in various other optical systems such as multimode optical systems [31]. Chaotic pulses have also been observed experimentally in fiber ring lasers [32] and various mode-locked laser (MLL) configurations [33]- [35]. This particular type is an example of a laser-generated optical rogue wave. Regarding multimode optical systems, optical rogue waves have been characterized by different degrees of nonlinearity, all having in common the excitation of many spatial modes experimentally.

First, SC-generated optical rogue waves are considered herein. In SC generation, light in a narrow band of frequencies is initially converted into ultra-broadband light, which has received a great deal of attention in recent years for its complex physics and wealth of potential applications [37], [38]. The experimental apparatus for SC generation in pioneering paper by Solli *et al.* is addressed here [9]. A schematic of the experimental apparatus is presented in Fig. 1.4. The SC source consists of a master oscillator, a fiber amplifier, and a 15 m length of highly nonlinear microstructured fiber. The master oscillator is a mode-locked ytterbium-doped fiber laser. The

output pulses from MLL are amplified to a desired level in a large-mode-area ytterbium-doped-fiber amplifier. Picosecond pulses at a wavelength of 1064 nm with a repetition rate of 20 MHz were launched into the highly nonlinear microstructured fiber as the initial seed pulses. The output is red-pass-filtered at 1450 nm. A critically important challenge to observing rogue waves is the lack of real-time instruments that can capture numerous extremely short random events in a single shot. To capture thousands of events with high resolution, wavelength-to-time transformation for real-time detection is accomplished using a highly dispersive optical fiber producing about -1300 ps/nm of group velocity dispersion (GVD). This technique was inspired by the concept of photonic time-stretch analog-to-digital conversion [39]. Adjacent pulses do not overlap in time after being stretched. Then the stretched signal is fed into a fast photodetector (PD) and captured using a real-time 20 GSa/s oscilloscope. Real-time oscilloscope records sequences of 15000 pulses with high temporal resolution in a single-shot measurement.

Figs. 1.5(a) and (b) respectively depict a representative single-shot time traces and histograms for three average power levels 0.8 μW (red), 3.2 μW (blue), and 12.8 μW (green). The noise floor of the measurement process is shown as a grey shaded area in each histogram. A histogram of each measurement display has a clear " L-shaped " profile with the vast majority of events buried in this low intensity range, and the rogue events reach intensities of at least 30-40 times the average value. In other words, typical events are apparently occurring much more frequently than the rare extreme events.

It is noteworthy that MLL is an attractive source of ultrashort optical pulses for many applications. Actually, it is an ideal platform for the fundamental exploration of complex dissipative nonlinear dynamics and an attractive source of rogue wave generation [36]. Rare events of extremely high optical intensity are recorded experimentally at the output of a mode-locked fiber laser. The probability distribution of these intensity fluctuations depends strongly on the cavity parameters and features an " L-shaped " distribution.

The experimental setup is presented in Fig. 1.6. The fiber ring laser cavity has dual 980 nm pumping of a 2 m long erbium doped fiber (EDF, normal dispersion D = -12.5 ps nm^{-1}km^{-1}). The maximum injected power is 800 mW. The ring includes a polarization-insensitive optical isolator (ISO) that ensures unidirectional laser emission at $\lambda \sim 1.5\mu$m. It also consists of a polarization controller (PC) made of small fiber loops (PC1), a 3% output coupler (OC), a polarization beam splitter (PBS), a four port 80:20 coupler, and a second polarization controller (PC2). The overall cavity length is 12 m, yielding a round trip time of 58 ns. The cavity operates at an anomalous path averaged chromatic dispersion (D = +10 ps/nm/km). The laser output is fed into a 45 GHz PD, with the electrical signal is recorded using a 20 GHz, 40 GSa/s real-time oscilloscope (WaveMaster 820Zi-A; LeCroy Corp.), which has a rise time of 22 ps.

The histogram displayed in Fig. 1.7(a) is for the recorded maximum optical intensity fluctuation for 4.9×10^6 events with pumping power of 600 mW. SWH is 41.9 mV for this case. Fig. 1.7(b) depicts the histogram for optical intensity record of a chaotic bunch of pulses when the PC is tilted by just 4 degrees. The long-tailed histogram presented in Fig. 1.7(b) displays numerous high-intensity events, thereby revealing the generation of rogue waves in the cavity. SWH of 81.2 mV histogram is obtainable and the extreme events are apparent up to three times the SWH. The yellow dotted line presented in Fig. 1.7(b) represents the classical distribution. The histogram shows a large deviation above the classical distribution. These transient waves appear

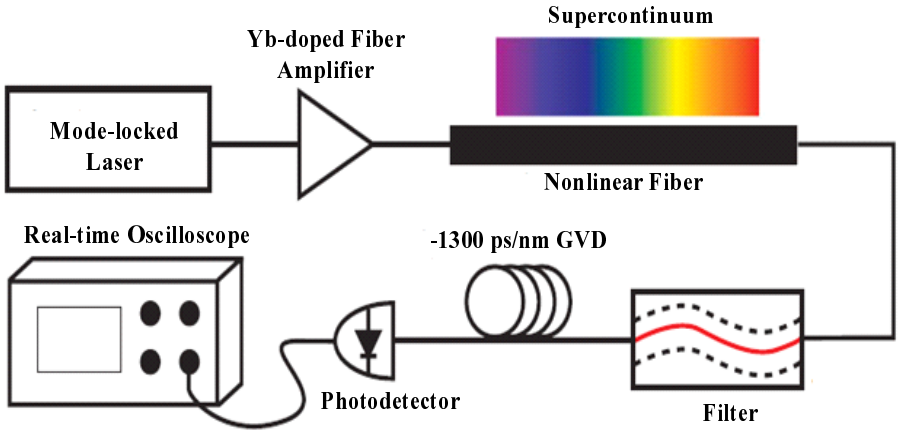

Fig. 1.4: Schematic showing the experimental apparatus used for SC generation (in Ref. [9]).

unexpectedly and disappear without a trace. Ultimately, the degrees of freedom of the nonlinear cavity transfer function, which are activated by adjusting the orientations of the polarization controllers, allow optimization of the occurrence of rogue wave phenomena.

Moreover, fiber fuse is a phenomenon known as a damage mechanism observed in waveguides. The fiber fuse itself can also be regarded as an adverse effect because it generates high peak power of optical rogue waves. Specific type of catastrophic destruction of an optical fiber core from the point of initiation toward the laser light source can be discovered because of this disturbance phenomenon [40], [41]. Damage is manifested by the periodic-like bullet-shaped cavities left in the core and filled with oxygen [42]. The effect can be initiated either by bringing the fiber output end into contact with absorbent materials, by bending the fiber and/or simply by heating the fiber with a flame from the end or in the middle of the fiber [41], [43]. Aside from the fiber fuse phenomenon, optical rogue waves can destroy optical fiber transmission devices such as amplifiers because of the high peak power.

1.3 Purpose of the study

The optical analog of oceanic rogue waves, named optical rogue waves, has recently been identified inside optical fibers, as described earlier. The main objective of this dissertation is exploration of optical rogue wave generation mechanisms. Soliton eigenvalue analysis was conducted as the analytical method. Different nonlinear evolution models can be considered when analyzing optical rogue waves. Actually, NLSE has played a pivotal role as the simplest universal nonlinear model [44]. However, it is necessary to go beyond the standard NLSE-based model to explain optical rogue wave phenomena because of NLSE limitations. Various types of dynamical and statistical behaviors are apparent for nonlinear models of different types [45]– [49]. In this dissertation, optical rogue wave behavior for NLSE and integrable higher-order NLSE (HNLSE) are investigated. In terms of generality, NLSE-based and HNLSE-based models resemble practical nonlinear evolution models.

Effects of higher-order dispersion terms must be considered for the pulses with narrow pulse width, such as optical rogue waves. To observe the crucially important role of higher-order dis-

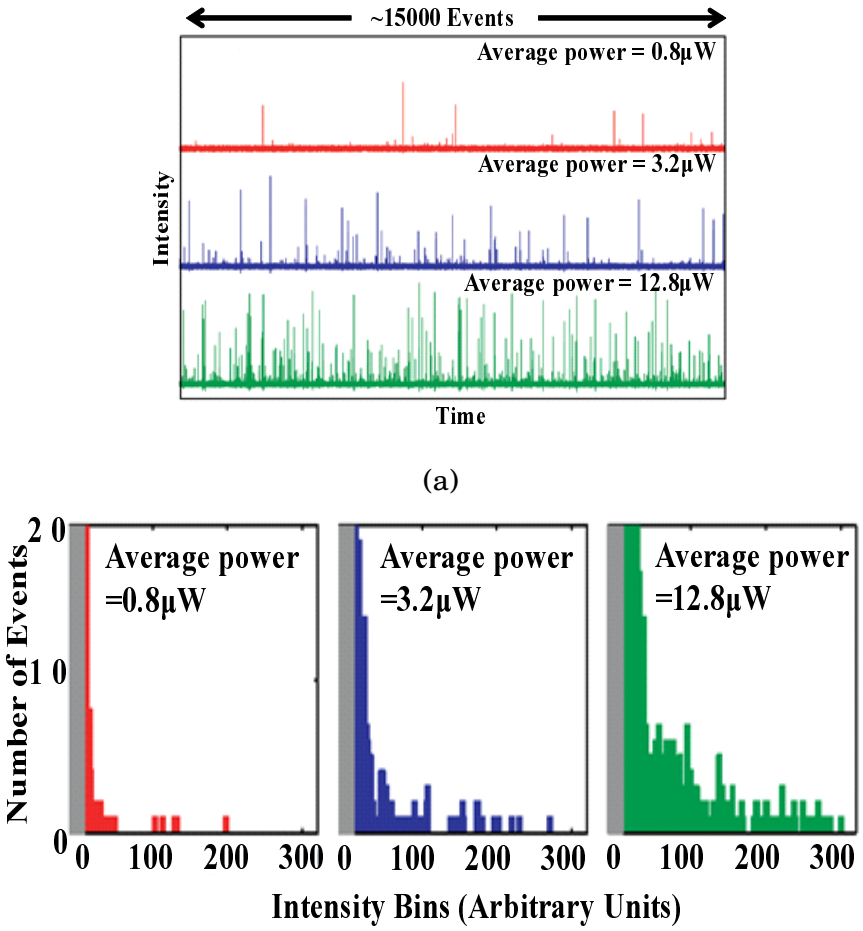

Fig. 1.5: (a) Single-shot time traces including roughly 15000 pulses each and (b) associated histograms (in Ref. [9]).

persion terms, effects of TOD have been evaluated. Moreover, investigations of optical rogue waves have confirmed the existence of TOD in optical fibers engenders generation of these extreme waves [50]– [52]. The effects of TOD on optical rogue waves also differ from model to model. Because of the non-integrability of NLSE-based model, analyses related to the effect of TOD stand only for small TOD coefficients [53]. Although optical rogue wave investigations flourish in different fields, the effect of large TOD on optical rogue waves becomes indispensable. To observe effects of large TOD on optical rogue waves, an HNLSE-based model is used for an integrable model. Optical rogue wave generation processes are also an open question in different nonlinear models [54]. Soliton's eigenvalue analysis tool was used to explore the soliton collision generated optical rogue waves for both NLSE-based and HNLSE-based models.

In addition to soliton-collision-generated optical rogue waves, soliton fusion generated optical rogue waves also exist in fiber systems. The phenomenon itself has been analyzed using various nonlinear evolution models [55]– [64]. Initial conditions for a pair of soliton pulses strongly influence pulse interactions [65]. In fact, soliton fusion has been observed in different fields. More complex and interesting one from a practical perspective is rogue wave structure. Amplitude

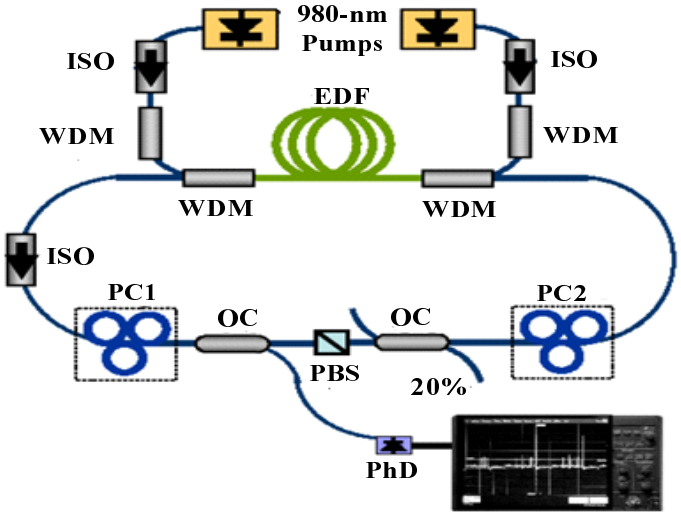

Fig. 1.6: Experimental apparatus of MLL (in Ref. [36]).

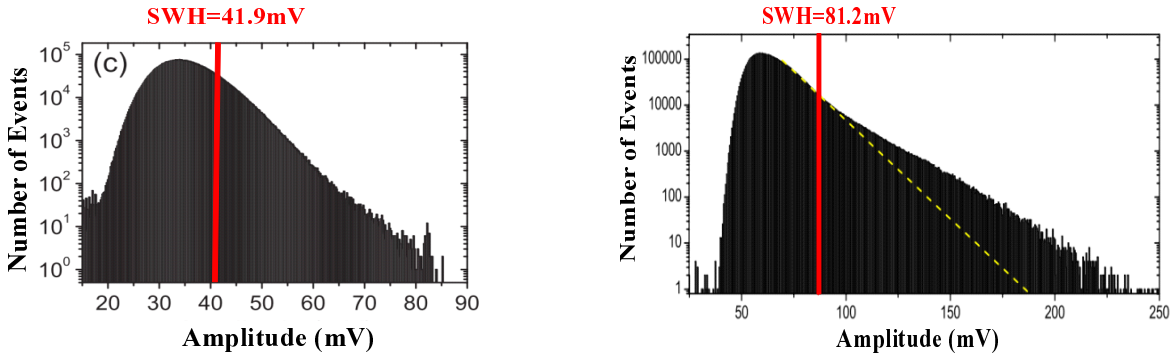

(a) (b)

Fig. 1.7: (a) Histogram for the pumping power of 600 mW and (b) the achieved histogram after tilting one polarization controller by 4 degrees (in Ref. [36]).

maintenance for long propagation after merging of two solitons is the most remarkable property of soliton fusion generated optical rogue waves. The effects of initial parameters of a pair of soliton pulses such as initial pulse spacing, frequency separation, and phase difference are analyzed to validate the soliton fusion generated optical rogue waves. Firstly, the effects of temporal spacing and frequency separation are analyzed. Next, the effects of frequency separation and phase difference are analyzed to ascertain pulse spacing parameters with which the soliton fusion phenomenon occurs.

The mathematical and physical analogies relating optical rogue waves are considered in each chapter. Early detection of rogue wave phenomena is extremely important. The main goal of this dissertation is to validate the soliton collision and fusion generated optical rogue waves to suppress this adverse effect on optical fiber systems.

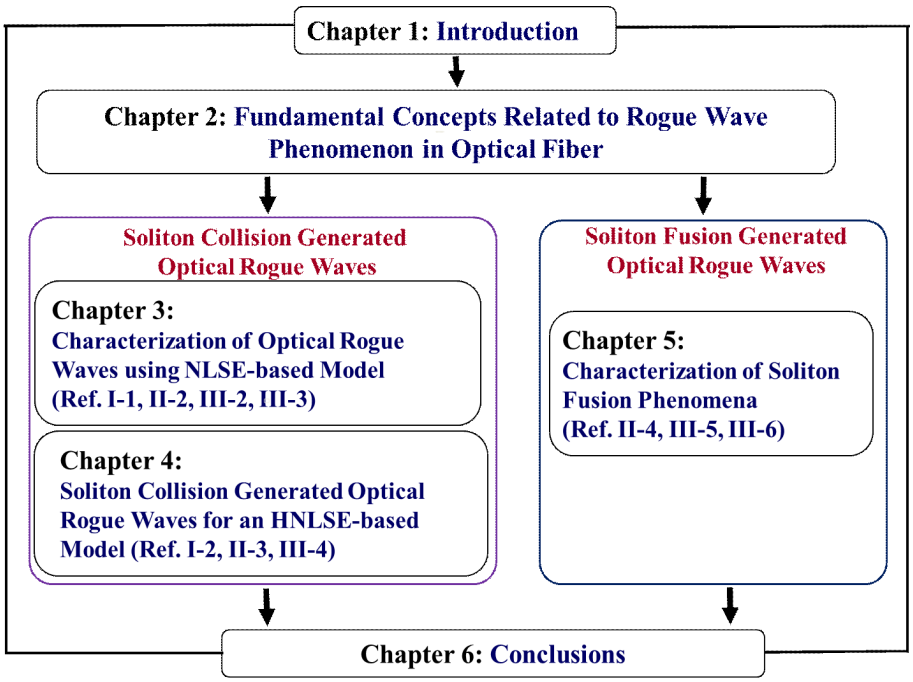

Fig. 1.8: Thesis organization.

1.4 Thesis organization

This thesis explains a study of optical rogue wave generation mechanisms in optical fiber based on soliton eigenvalues. Six chapters are organized as presented schematically in Fig. 1.8.

Chapter 2 presents fundamental concepts related to optical rogue waves. MI is discussed as a main nonlinear phenomenon to initiate optical rare and strong events inside optical fiber. Soliton fission, fusion, and collision processes are described to inspire ideas related to such concepts. Eigenvalue equations associated with NLSE are discussed as an optical rogue wave generation evaluation method. Finally, concepts related to optical solitons, such as fundamental and higher-order soliton solutions, are discussed.

Chapter 3 is devoted to characterize optical rogue waves for an NLSE-based model. After brief discussion of the generation of optical rogue waves in the NLSE-based model, effects of TOD on optical rogue wave generation are investigated numerically. Generation mechanisms of optical rogue waves for the NLSE-based model are evaluated using the eigenvalues of solitons. Finally, soliton stability against TOD is demonstrated numerically as a proof-of-evaluation of the NLSE-based model.

In Chapter 4, soliton collision generated optical rogue waves for a HNLSE-based model is demonstrated. By using this model, TOD can be considered within the framework of an integrable model. Eigenvalue equations associated with HNLSE are presented as an evaluation method. Numerical demonstrations of the effect of TOD on optical rogue waves for the HNLSE-based model are conducted using peak power calculations and eigenvalues evaluation. Generation mechanisms of optical rogue waves for a wider range of TOD parameter can be explained based on the HNLSE-based model. Numerical demonstrations of soliton stability for the HNLSE-based model are conducted at the end of the chapter.

Chapter 5 emphasizes an explanation of the soliton fusion phenomenon, with discussion of the effects of initial parameters. After introducing the fundamental concepts, numerical models and the effects of temporal spacing and frequency separation of initial pulse pair for soliton fusion are demonstrated. Next, effects of frequency separation and phase difference of initial pulse pair for soliton fusion are demonstrated. Fusion events for different initial parameters are presented briefly to inspire several ideas. The assessment of the authenticity of numerical simulation results is discussed before presenting the conclusion. Finally, the achieved initial parameter range for soliton fusion phenomena is concluded.

Finally, Chapter 6 draws conclusions from the entire thesis and presents a summary of the results.

Chapter 2

Theoretical Background of Rogue Wave Phenomenon in Optical Fiber

2.1 Introduction

Basic concepts related to optical rogue wave generation are presented in this chapter. Fundamental and higher-order soliton solutions take a key role in this research. Therefore, overview of optical solitons is presented at the beginning of this chapter. Modulational instability (MI) is introduced as a nonlinear phenomenon to initiate rare optical events that occur inside optical fiber. Soliton fission, fusion, and collision processes are described to inspire ideas related to such concepts. Eigenvalue equation associated with nonlinear Schrödinger equation (NLSE) is discussed as a method of evaluating optical rogue wave generation. Eigenvalues are determined by solving the matrix form eigenvalue equation.

Concepts of soliton solutions such as fundamental and higher-order soliton are discussed in section 2.2. Section 2.3 presents a detailed description of MI. Moreover, soliton fission and fusion phenomena that occur from soliton interactions are described in this section. In Section 2.4, basic concepts of the eigenvalue equation associated with NLSE are addressed from the viewpoint of evaluation techniques of numerical simulation results. Finally, section 2.5 concludes Chapter 2.

2.2 Overview of Optical Solitons

An optical soliton is a specific pulse that propagates without distortion during long-haul propagation. The pulse shape is maintained by the delicate balance between group velocity dispersion (GVD) and self-phase modulation (SPM) effects along the fiber length. It sometimes follows a periodic evolution pattern. Hasegawa and Tappert found such a stable pulse inside a fiber in 1987 [66]. Many studies have been undertaken for long-haul transmission application [67]– [71].

2.2.1 Fundamental Soliton

First-order soliton $(N = 1)$ corresponding to a single eigenvalue is often called as fundamental soliton. When $u(Z = 0, T)$ is a solution of the NLSE (see Eq. (2.29)) with $\sigma = 0$, eigenvalue ζ is constant irrespective of Z. The eigenvalue for initial value $u(Z = 0, T)$ and eigenfunction

$\Psi_l(Z,T), (l = 1,\ 2)$ are calculable using this property. The discrete eigenvalue of the eigenvalue equation associated with the NLSE (see Eq. (2.30)) can be represented as

$$\zeta_j = \frac{\kappa_j + i\eta_j}{2} , \quad (j = 1, 2, \ldots\ldots, N) . \tag{2.1}$$

Using the eigenvalue given by Eq. (2.1), the following expression presents the asymptotic form of N-order soliton solution.

$$u(Z,T) = \sum_{j=1}^{N} \eta_j \, \mathrm{sech}[\eta_j(T + \kappa_j Z - T_{0j})] \exp\left[-i\kappa_j T + \frac{i}{2}({\eta_j}^2 - {\kappa_j}^2)Z + i\theta_{0j}\right] . \tag{2.2}$$

Here η_j, κ_j, T_{0j}, and θ_{0j} respectively represent the amplitude, frequency, initial position, and the initial phase of the j-th optical soliton. Also, η_j and κ_j are the imaginary and real parts of eigenvalues represented in Eq. (2.1). Next, the hyperbolic-second shape pulse is regarded as the initial waveform.

$$u(Z = 0, T) = A \, \mathrm{sech}(T) . \tag{2.3}$$

Here, A represents the peak amplitude of u. Eigenvalue of of the eigenvalue equation associated with the NLSE (see Eq. (2.30)) for the initial waveform given by Eq. (2.3) can be derived analytically. The number of discrete eigenvalues N satisfies as [72]

$$A - \frac{1}{2} < N \leq A + \frac{1}{2} . \tag{2.4}$$

Here, pure imaginary eigenvalues can be expressed as the following formula.

$$\zeta_j = i\frac{\eta_j}{2} = i\left(A - j + \frac{1}{2}\right) , \quad (j = 1, 2, \ldots\ldots, N) . \tag{2.5}$$

The following relation between A and η_j can be derived using Eq. (2.5).

$$\eta_j = 2(A - j) + 1 , \quad (j = 1, 2, \ldots\ldots, N) . \tag{2.6}$$

When A coincides with an integer number N, the solution for the initial waveform of Eq. (2.3) does not include dispersive waves and becomes the N-order soliton solution. The amplitude of N solitons is given by the following equation,

$$\eta_j = 2(N - j) + 1 = 1, 3, 5, \ldots\ldots, (2N - 1) , \quad (j = 1, 2, \ldots\ldots, N) . \tag{2.7}$$

Fig. 2.1 presents the relation between the amplitude of initial waveform shown in Eq. (2.3) and the achievable imaginary part of eigenvalues. In other words, the number of soliton N is a function of initial amplitude A as shown in Fig. 2.1.

2.2.2 Higher-order Soliton

Higher-order soliton consists of multiple fundamental solitons corresponding to the multiple eigenvalues. When $\kappa_j = 0$ in Eq. (2.2), the soliton solution can be asymptotically written as

$$u_j(Z,T) = \sum_{j=1}^{N} \eta_j \, \mathrm{sech}\left\{\eta_j(T - T_{0j})\right\} \exp\left\{i\left(\frac{{\eta_j}^2}{2}Z + \theta_{0j}\right)\right\} . \tag{2.8}$$

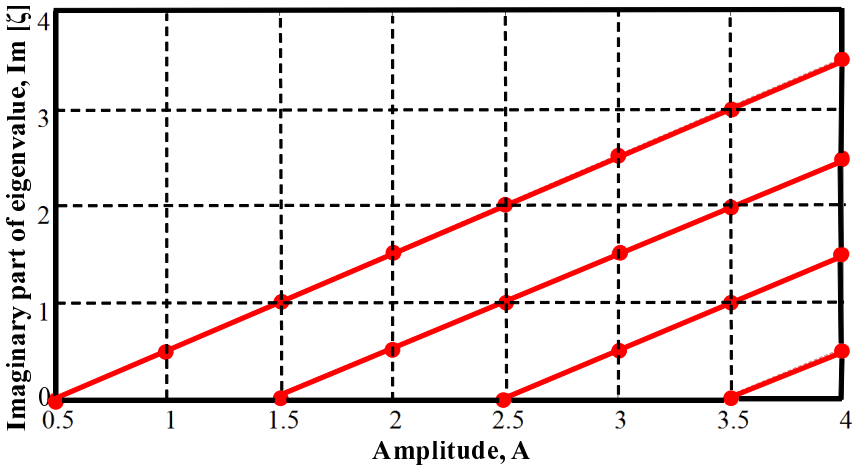

Fig. 2.1: Relation between amplitude of solitons and the achievable imaginary part of eigenvalues.

The waveform is changing periodically by interference among multi solitons which amplitudes are η_j. For this case, the individual phase change is given by $\frac{{\eta_j}^2}{2}Z$. For $N = 2$ case, the phase difference of two solitons can be expressed as $\Delta\theta = \frac{\eta_i^2 - \eta_j^2}{2}Z$. So the waveform is periodically changing with the period of Z_p expressed as

$$Z_p = \frac{2\pi}{\eta_1^2/2 - \eta_2^2/2} = \frac{4\pi}{|\eta_1^2 - \eta_2^2|} \,. \tag{2.9}$$

Z_p is designated as the soliton period. When the initial pulse is given by Eq. (2.3) with $A = 2$, then Z_p can be expressed as

$$Z_p = \frac{4\pi}{3^2 - 1^2} = \frac{\pi}{2} \,. \tag{2.10}$$

Pulse having more than two discrete eigenvalues is called higher-order soliton. It appears in the case of $A > 1.5$ in Eq. (2.3) and its feature is periodically changing waveform. It is quite different from fundamental soliton whose waveform does does not change during the propagation. Figs. 2.2(a) and (b) respectively show temporal evolutions of a fundamental soliton and a higher-order soliton. In Fig. 2.2(b), SPM is dominant in the early stages of propagation and contraction of the pulse dispersion effect becomes dominant soon after and back to the initial soliton pulse waveform after the soliton period. The total energy is $2A^2$ for higher-order soliton given by Eq. (2.3). However, total energy becomes 2η for fundamental soliton solution $u = \eta\,\mathrm{sech}(\eta T)$.

2.3 Occurrence of Localized Waves

2.3.1 Principle of Modulational Instability

Many nonlinear systems exhibit instability in an anomalous dispersion regime and manifest it as a breakup of continuous wave (CW) or quasi-CW radiation into a train of ultra-short pulses as a result of interplay between the nonlinear and dispersive effects [24]. This concept is referred

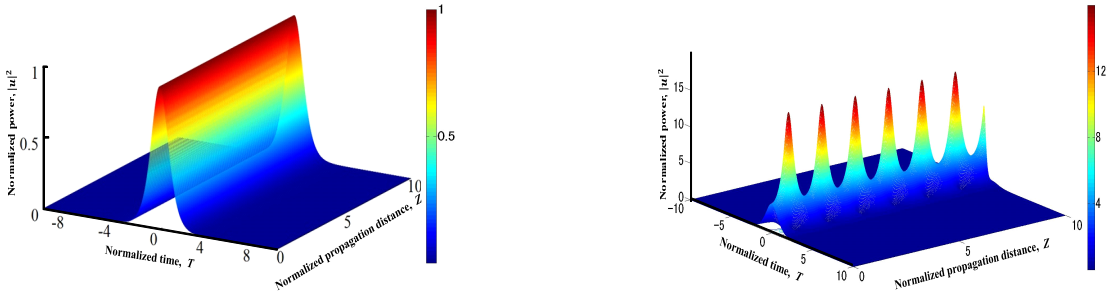

(a) Fundamental soliton for $A = 1$ (b) Higher-order soliton for $A = 2$

Fig. 2.2: Soliton solutions.

to MI and studied during the 1960s in various fields including fluid dynamics [73] and nonlinear optics [74]– [76]. The stability of a steady state depends strongly on whether light experiences a normal or anomalous GVD in optical fiber. In the nonlinear theory of the hydrodynamic context, the waves grow exponentially because of Benjamin–Feir instability [7]. Instability increases exponentially in the initial stage and reaches a saturated level. After reaching that level, it returns gradually to the initial stage. In other words, in a conservative system, all waves appear from nowhere and always disappear without any trace. Many theories can be considered for the formation of optical rare or unexpected events under different conditions. MI, a complex nonlinear process exhibiting emergent behavior and a strong sensitivity to initial conditions [25], [26] serves a crucially important role in the appearance of extraordinary waves in many optical scenarios [9, 26, 28, 77].

MI is theoretically analyzed in this subsection. The behavior of the complex envelope of a light wave propagating in a fiber in the presence of the second and the third order dispersion and nonlinear effects can be expressed as [78]

$$i\frac{\partial u}{\partial Z} - \frac{b}{2}\frac{\partial^2 u}{\partial T^2} + |u|^2 u = i\sigma\frac{\partial^3 u}{\partial T^3} \ , \tag{2.11}$$

where Z, T, and $u(Z,T)$ respectively represent the normalized quantities of propagation distance, time moving frame with the group velocity, and the complex envelope of the electric field. Moreover, $b\ (= \pm 1)$ and σ respectively define the normalized second and third order dispersion coefficients [78]. While $b = 1$ corresponds to normal dispersion case, $b = -1$ corresponds to anomalous dispersion case.

Here, we consider a CW propagation inside an optical fiber. For CW, the amplitude is independent with T at the input end of the fiber at $Z = 0$. Assuming that $u(Z,T)$ remains time-independent during propagation inside the fiber, the steady state solution of Eq. (2.11) is given by,

$$u_{\mathrm{CW}}(Z,T) = \sqrt{P(0)}\exp(i\phi_{NL}) \ . \tag{2.12}$$

Here, $P(0)(= |u(Z=0,T)|^2)$ is the normalized input power at $Z = 0$.

$$\phi_{NL}(Z) = P(0)Z \ , \tag{2.13}$$

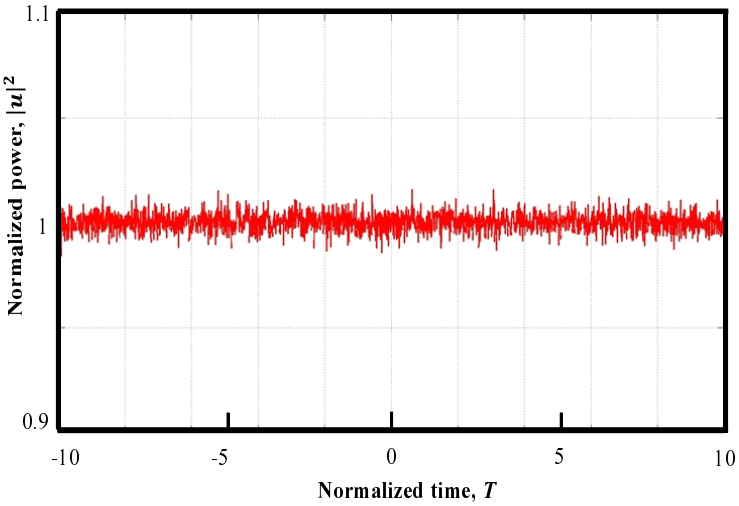

Fig. 2.3: Perturbed CW.

is the nonlinear phase shift induced by SPM. Eq. (2.12) implies that CW is expected to propagate through the fiber unchanged, except for acquisition of a power-dependent phase shift.

Next, stability against small perturbations of the steady state solution Eq. (2.12) is examined. The initial input is illustrated in Fig. 2.3. We assume that the solution of Eq. (2.11) can be expressed as

$$u(Z,T) = \left\{\sqrt{P(0)} + a(Z,T)\right\}\exp(i\phi_{NL}) \ , \tag{2.14}$$

where $a(Z,T)$ represents a small perturbation which satisfies $|a|^2 \ll P(0)$. Substituting Eq. (2.14) in Eq. (2.11) and linearizing in a,

$$i\frac{\partial a}{\partial Z} - \frac{b}{2}\frac{\partial^2 a}{\partial T^2} + P(0)(a+a^*) = i\sigma\frac{\partial^3 a}{\partial T^3} \ , \tag{2.15}$$

can be obtained. The Fourier transform of $a(Z,T)$ can be written as

$$\tilde{a}(Z,\Omega) = \frac{1}{\sqrt{2\pi}}\int_{-\infty}^{\infty} a(Z,T)\exp(-i\Omega T)dT \ . \tag{2.16}$$

Perform Fourier transform to Eq. (2.15), and we obtain

$$\frac{d}{dZ}\begin{Bmatrix} \tilde{a}+\tilde{a}^* \\ \tilde{a}-\tilde{a}^* \end{Bmatrix} = \left[\begin{array}{c|c} 0 & i\left(\frac{b}{2}\Omega^2 - \sigma\Omega^3\right) \\ \hline i\left\{\frac{b}{2}\Omega^2 - \sigma\Omega^3 + 2P(0)\right\} & 0 \end{array}\right]\begin{Bmatrix} \tilde{a}+\tilde{a}^* \\ \tilde{a}-\tilde{a}^* \end{Bmatrix} \ . \tag{2.17}$$

Hereafter we consider $\sigma = 0$ case for simplicity.

(1) When $b = 1$ (normal dispersion), or $b = -1$ (anomalous dispersion) and $|\Omega| > 2\sqrt{P(0)}$,

$$\tilde{a}(Z,\Omega) = \tilde{a}(0,\Omega)\cos\{\theta(Z)\} + i\frac{\sin\{\theta(Z)\}}{\sqrt{1+\frac{4P(0)}{b\Omega^2}}}\left[\tilde{a}(0,\Omega) + \frac{2P(0)}{b\Omega^2}\{\tilde{a}(0,\Omega)+\tilde{a}^*(0,\Omega)\}\right] \ . \tag{2.18}$$

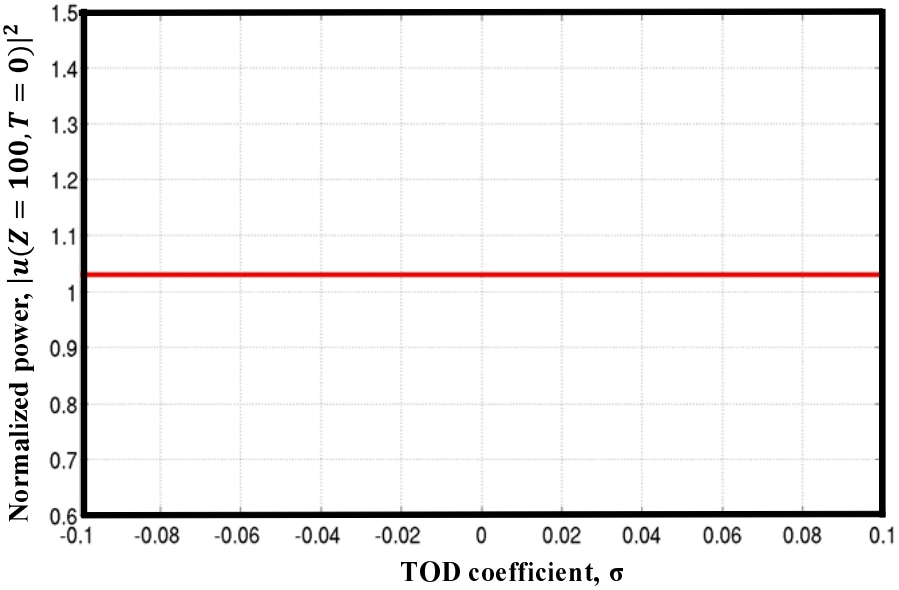

Fig. 2.4: Power of perturbed CW at $Z = 100$ vs. magnitude of TOD coefficient for normal dispersion case.

Here,

$$\theta(Z) = \frac{\Omega^2}{2}\sqrt{1 + \frac{4P(0)}{b\Omega^2}}\; Z\;. \tag{2.19}$$

Therefore,

$$|\tilde{a}(Z,\Omega)|^2 = |\tilde{a}(0,\Omega)|^2 + \frac{\sin^2\{\theta(Z)\}}{2 + \frac{b\Omega^2}{2P(0)}}\left[\frac{2P(0)}{b\Omega^2}\{\tilde{a}(0,\Omega) + \tilde{a}^*(0,\Omega)\}^2 + \{\tilde{a}(0,\Omega)\}^2 + \{\tilde{a}^*(0,\Omega)\}^2\right], \tag{2.20}$$

and $|\tilde{a}(Z,\Omega)|^2$ is a periodic function with the period of

$$Z_p = \frac{4\pi}{\Omega^2\sqrt{1 + \frac{4P(0)}{b\Omega^2}}}\;. \tag{2.21}$$

Then, $|\tilde{a}(Z,\Omega)|^2$ is not increasing exponentially with Z and the CW solution of Eq. (2.11) is stable. $\sigma \neq 0$ case is examined in Fig. 2.4. This shows $|u(Z = 100, T = 0)|^2$ when a perturb CW is launched in a fiber having small third-order dispersion (TOD) coefficient. No instability is observed for these cases. In these cases,

$$\left(\frac{b}{2}\Omega^2 - \sigma\Omega^3\right)\left\{\frac{b}{2}\Omega^3 - \sigma\Omega^3 + 2P(0)\right\} > 0 \tag{2.22}$$

is satisfied.

(2) When $b = -1$ (Anomalous dispersion) and $|\Omega| < 2\sqrt{P(0)}$,

$$\tilde{a}(Z,\Omega) = \tilde{a}(0,\Omega)\cosh\{\theta^{'}(Z)\} - i\frac{\sinh\{\theta^{'}(Z)\}}{\sqrt{\frac{4P(0)}{\Omega^2}-1}}\left[\tilde{a}(0,\Omega) - \frac{2P(0)}{\Omega^2}\{\tilde{a}(0,\Omega)+\tilde{a}^{*}(0,\Omega)\}\right]. \quad (2.23)$$

Here,

$$\theta^{'}(Z) = \frac{\Omega^2}{2}\sqrt{\frac{4P(0)}{\Omega^2}-1}\; Z\,. \quad (2.24)$$

Therefore,

$$|\tilde{a}(Z,\Omega)|^2 = |\tilde{a}(0,\Omega)|^2 + \frac{\sinh^2\{\theta^{'}(Z)\}}{2-\frac{\Omega^2}{2P(0)}}\left[\frac{2P(0)}{\Omega^2}\{\tilde{a}(0,\Omega)+\tilde{a}^{*}(0,\Omega)\}^2 - \left(\{\tilde{a}(0,\Omega)\}^2 + \{\tilde{a}^{*}(0,\Omega)\}^2\right)\right]. \quad (2.25)$$

It is noteworthy that $|\tilde{a}(Z,\Omega)|^2$ is proportional to the factor $\exp[2\theta^{'}(Z)]$ and exponentially increasing with Z for $Z \gg 1$. Therefore, CW solution of Eq. (2.11) is unstable and this instability is called MI.

Fig. 2.5 shows perturbed CW transforms into higher-order soliton pulse train and a dispersive wave with respective to Z. When the TOD is zero, higher-order solitons are generated because MI process propagate through the fiber by changing the temporal waveform and frequency spectrum periodically. However, when considering the non-zero TOD case, higher-order solitons split into multiple quasi-solitons that correspond to multiple eigenvalues of the eigenvalue equation associated with NLSE while they propagate in the fiber.

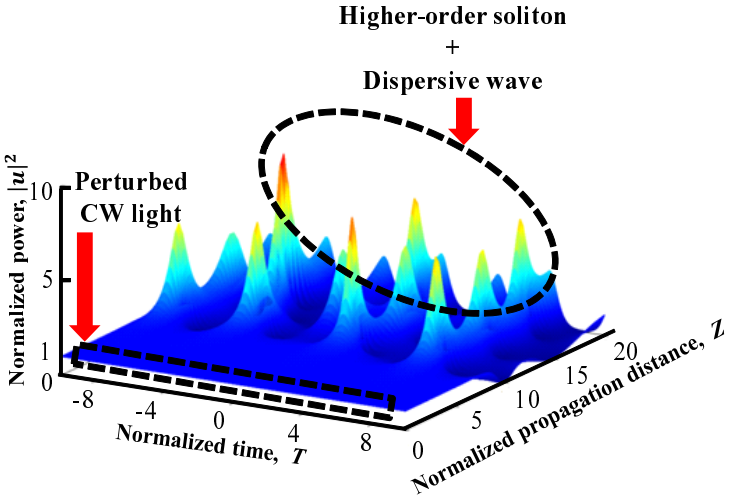

Fig. 2.5: MI process.

2.3.2 Soliton Fission

Soliton fission is a process that breaks higher-order soliton apart because of higher-order dispersive or nonlinear perturbations. Higher-order solitons generated via MI process propagate

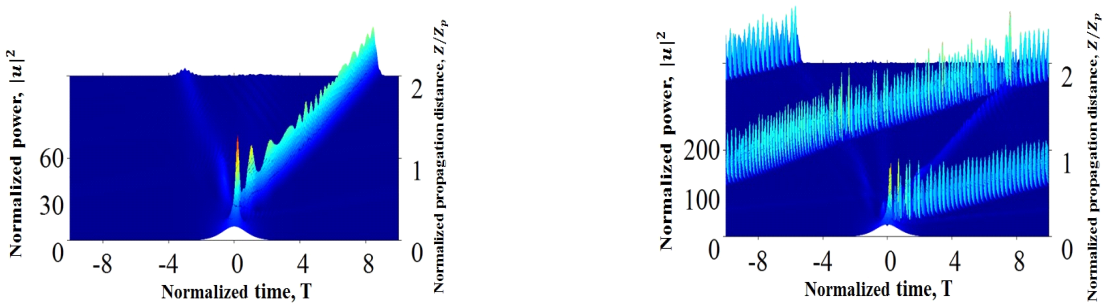

(a) N=3. (b) N=5.

Fig. 2.6: Soliton fission when considering TOD ($\sigma = 0.02$).

inside the fiber by changing the temporal waveform periodically with the period of the soliton period Z_p represented in Eq. (2.9) when TOD is zero. However, when the TOD is non-zero, higher-order solitons split into fundamental solitons that correspond to multiple eigenvalues. This phenomenon is called soliton fission. Figs. 2.6(a) and (b) respectively represent $N = 3$ and $N = 5$ cases. Here N denotes the order of the solitons.

As shown in Figs. 2.6(a) and (b), a higher-order soliton splits into multiple fundamental solitons accompanied by generation of dispersive waves. The fundamental soliton corresponding to the largest eigenvalue $\eta = 5$ can only be observed clearly in Fig. 2.6(a) for $N = 3$ case. However, in practice, fundamental solitons corresponding to eigenvalues $\eta = 1$ and $\eta = 3$ also split and propagate with respect to Z. Solitons corresponding to eigenvalue $\eta = 1$ and $\eta = 3$ are invisible because the amplitudes of those solitons are extremely low compared with $\eta = 5$ soliton. As shown in Fig. 2.6(b), fundamental solitons corresponding to the largest eigenvalue $\eta = 9$ and the second largest eigenvalue $\eta = 7$ are mutually separated and they propagate with respect to Z for $N = 5$ case.

2.3.3 Soliton Interactions

Soliton interactions are occured between co-propagating solitons due to nonlinearity. Soliton fusion is one of wave phenomena caused by soliton interactions between co-propagating solitons with small temporal, frequency, and appropriate phase separation, as presented in Fig. 2.7. Particularly, it has been predicted that solitons can fuse when propagating in nonlinear medium [55]. Merging of solitons into a single pulse during soliton collision is the principal feature of soliton fusion. As a result of soliton fusion, a high-intensity robust light structure arises and propagates over significant distances without recovering to the initial solitons. Soliton fusion is considered as one of optical rogue wave generation mechanisms. Initial conditions in a pair of soliton pulses strongly influence the interactions between pulses. Moreover, energy dissipation of solitons is visible during interaction processes. Some amount of soliton's energy is transferred to dispersive waves. Consequently, soliton fusion will be accelerated as a result of multiple interactions between solitons and dispersive waves [55].

Two simultaneously launched optical solitons with different soliton parameters can be repre-

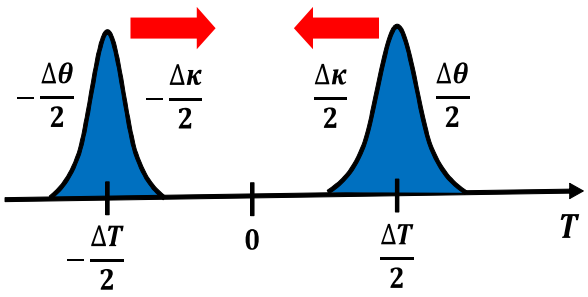

Fig. 2.7: Interactions between solitons.

sented as

$$u(Z=0,T) = \mathrm{sech}(T+\Delta T/2)\exp(i\Delta\nu T/2 + i\Delta\theta/2) + \mathrm{sech}(T-\Delta T/2)\exp(-i\Delta\nu T/2 - i\Delta\theta/2)\ , \tag{2.26}$$

where ΔT, $\Delta\nu$, and $\Delta\theta$ respectively represent the normalized quantities of pulse spacing, frequency separation, and phase difference between those simultaneously launched two optical solitons. When two identical solitons are launched into an optical fiber, they either co-propagate or mutually repulse depending on their parameters. To inspire a brief idea related to soliton interactions, intensity profiles along the propagation distance for soliton collision process are presented schematically in Fig. 2.8 for different pulse spacing and frequency separation. Two fundamental solitons given by Eq. (2.26) are used as the initial waveform for Eq. (2.11) with $b=-1$ and $\sigma=0$. Whereas Fig. 2.8(a) presents the co-propagating solitons for $\Delta T=\Delta\nu=0.5$ and $\Delta\theta=0$ case, Fig. 2.8(b) shows repulsing solitons for $\Delta T=6.0$, $\Delta\nu=0.3$, and $\Delta\theta=0$ case. Co-propagation and repulsion are apparent after the collision according to temporal spacing and frequency separation of two solitons. Two soliton-fission-ejected solitons will meet such interactions rather than quasi-elastic collision when the temporal and frequency separation between two solitons is small. In the repulsion case, two solitary pulses have been found to propagate independently after the collision. Because conditions for the soliton fusion are extremely delicate, the fusion itself is a very rare event.

The total energy of the initial waveform given by Eq. (2.26) can be represented as

$$E_T = \int_{-\infty}^{\infty} |u(Z=0,T)|^2 dT = 1 - \pi\frac{\sinh(\pi\Delta\nu/2)[\sin(\Delta\nu\Delta T+\Delta\theta)-\sin(\Delta\theta)]}{\sinh(\Delta T)[1-\cosh(\pi\Delta\nu)]}\ . \tag{2.27}$$

Soliton collision is accompanied by strong irradiation of a low-intensity dispersive wave. Dispersive wave energy can be given as the difference between the total energy and the soliton's energy. So dispersive wave energy ΔE is given as

$$\Delta E(\Delta T,\Delta\nu,\Delta\theta) = E_T - 2\sum_{i=1}^{N}\eta_i\ , \tag{2.28}$$

where $2\eta_i$ represents the i-th soliton's energy and N stands for the number of solitons.

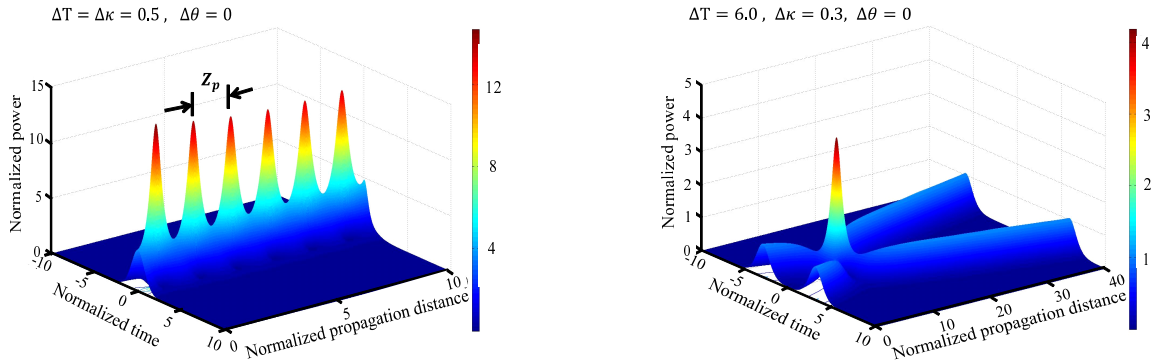

(a) (b)

Fig. 2.8: (a) Co-propagation of solitons for $\Delta T = \Delta\nu = 0.5,\ \Delta\theta = 0$ and (b) repulsion after soliton collision for $\Delta T = 6.0,\ \Delta\nu = 0.3,\ \Delta\theta = 0$.

2.4 Eigenvalue Equation Associated with NLSE

2.4.1 Principle of Eigenvalue Analysis

Recently, eigenvalues have drawn interest in research in the field of optics as an approach to evaluate the numerically and experimentally obtained results [79]. The behavior of the complex envelope of a light wave propagating in a fiber can be represented by widely known NLSE. We set $b = -1$ in Eq. (2.11), the normalized NLSE in the presence of TOD in anomalous dispersion regime can be represented as

$$i\frac{\partial u}{\partial Z} + \frac{1}{2}\frac{\partial^2 u}{\partial T^2} + |u|^2 u = i\sigma\frac{\partial^3 u}{\partial T^3}\ . \tag{2.29}$$

Special kind of nonlinear wave equations are integrable using inverse scattering transform [80]. The normalized NLSE in Eq. (2.29) belongs to this special class when $\sigma = 0$. The inverse scattering transform for the NLSE was firstly reported by Zakharov and Shabat in 1971 [81]. This method is similar to the Fourier transform that is widely used for solving linear partial differential equations. The eigenvalue equation associated to Eq. (2.29) can be represented when $\sigma = 0$ as

$$\begin{aligned} i\frac{\partial \psi_1}{\partial T} + u(Z,T)\psi_2 &= \zeta\psi_1\ , \\ -i\frac{\partial \psi_2}{\partial T} + u^*(Z,T)\psi_1 &= \zeta\psi_2\ , \end{aligned} \tag{2.30}$$

where ζ is complex eigenvalue and $\psi_l(Z,T), (l = 1,2)$ are the eigenfunctions [80]. As long as u is a solution of Eq. (2.29) with $\sigma = 0$, eigenvalue ζ of Eq. (2.30) is invariant with Z, even if the temporal waveform and the frequency spectrum are drastically changed.

2.4.2 Calculation of Eigenvalues

To calculate eigenvalue ζ, Eq. (2.30) is converted to integral equations by performing Fourier transform defined as

$$\tilde{f}(\Omega) = \frac{1}{\sqrt{2\pi}} \int_{-\infty}^{\infty} f(T) \exp(i\Omega T) dT \ . \tag{2.31}$$

Then, Eq. (2.30) is transformed to

$$\begin{cases} \Omega\tilde{\psi}_1(Z,\Omega) + \dfrac{1}{\sqrt{2\pi}} \displaystyle\int_{-\infty}^{\infty} \tilde{u}(Z,\Omega-\Omega')\tilde{\psi}_2(Z,\Omega')d\Omega' = \zeta\tilde{\psi}_1(Z,\Omega) \ , \\ -\Omega\tilde{\psi}_2(Z,\Omega) - \dfrac{1}{\sqrt{2\pi}} \displaystyle\int_{-\infty}^{\infty} \tilde{u}^*(Z,\Omega'-\Omega)\tilde{\psi}_1(Z,\Omega')d\Omega' = \zeta\tilde{\psi}_2(Z,\Omega) \ , \end{cases} \tag{2.32}$$

where $\tilde{u}(Z,\Omega)$ and $\tilde{\psi}_\ell(Z,\Omega)$, $(\ell = 1,2)$ respectively represent the Fourier transform of $u(Z,T)$ and $\psi_\ell(Z,T)$. Furthermore, by discretization $\tilde{u}(Z,\Omega)$ and $\tilde{\psi}_\ell(Z,\Omega)$ in the Ω domain and by replacing the integration by summation over discretized sections, Eq. (2.32) can be converted into a discrete form for a fixed distance as

$$\begin{cases} \Omega_n\tilde{\psi}_1(\Omega_n) + \dfrac{\Delta\Omega}{\sqrt{2\pi}} \displaystyle\sum_{m=1}^{N} \tilde{u}(\Omega_n-\Omega_m)\tilde{\psi}_2(\Omega_m) = \zeta\tilde{\psi}_1(\Omega_n) \ , \\ -\Omega_n\tilde{\psi}_2(\Omega_n) - \dfrac{\Delta\Omega}{\sqrt{2\pi}} \displaystyle\sum_{m=1}^{N} \tilde{u}^*(\Omega_m-\Omega_n)\tilde{\psi}_1(\Omega_m) = \zeta\tilde{\psi}_2(\Omega_n) \ , \end{cases} \tag{2.33}$$

It is noteworthy that Eq. (2.33) can be rewritten as an eigenvalue problem of matrix form as

$$\left[\begin{array}{c|c} \mathbf{A} & \mathbf{B} \\ \hline -\mathbf{B}^* & -\mathbf{A} \end{array}\right] \left[\begin{array}{c} \tilde{\mathbf{\Psi}}_1 \\ \hline \tilde{\mathbf{\Psi}}_2 \end{array}\right] = \zeta \left[\begin{array}{c} \tilde{\mathbf{\Psi}}_1 \\ \hline \tilde{\mathbf{\Psi}}_2 \end{array}\right] \ . \tag{2.34}$$

Here, $\widetilde{\mathbf{\Psi}}_\ell$, $(\ell = 1,2)$ is a column vector with elements of $\widetilde{\psi}_\ell(\Omega_n)$. $\mathbf{A}$ and $\mathbf{B}$ are $N \times N$ square matrices, for which respective elements are given by

$$a_{jk} = \begin{cases} \Omega_j & (j = k) \ , \\ 0 & (\text{otherwise}) \ , \end{cases} \tag{2.35}$$

$$b_{jk} = \begin{cases} \dfrac{1}{\sqrt{2\pi}}\tilde{u}(\Omega_{n_{jk}})\Delta\Omega & (1 \leqq n_{jk} \leqq N) \ , \\ 0 & (\text{otherwise}) \ . \end{cases} \tag{2.36}$$

Here, $n_{jk} = N/2 + j - k + 1$ for even number N and $\Delta\Omega$ $(= \Omega_{n+1} - \Omega_n)$ is the discretization interval in frequency. $\mathbf{B}^*$ is the conjugate transpose of $\mathbf{B}$.

2.5 Conclusions

This chapter introduced basic concepts related to optical rogue waves. At the beginning of the chapter, concepts of optical solitons such as fundamental and higher-order soliton solutions were introduced. Perturbed CW in anomalous dispersion fiber becomes unstable due to MI, which initiate optical rogue wave generation. Starting with the introduction of MI, various concepts related to solitons such as soliton fission, soliton interactions, and soliton fusion phenomenon have been discussed in section 2.3. Eigenvalue equations associated with NLSE were presented in section 2.4. Numerical calculation method of eigenvalues were introduced by solving the matrix form eigenvalue problem.

Chapter 3

Characterization of Optical Rogue Waves using NLSE-based Model

3.1 Introduction

Rogue wave research has been actively conducted based on the nonlinear Schrödinger equation (NLSE)-based model which is one of the simplest nonlinear evolution models. Recent studies have confirmed that the presence of third-order dispersion (TOD) in optical fibers turns the system convectively unstable and generates extraordinary optical intensities. This statistical signature has been observed experimentally and confirmed numerically both in hydrodynamic and optical situations [2], [82]. The effects arising from higher-order dispersion terms such as TOD cannot be ignored for pulses with narrow pulse width. The crucially important role of TOD on the statistics of optical rogue waves is emphasized for the NLSE-based model in this chapter. Moreover, as described in Chapter 1, previous reports have described that the collision of soliton is one of generation mechanisms of optical rogue wave. Since pure solitons cannot exist when TOD exist, terms " soliton " and " quasi-soliton " are used for zero and non-zero TOD cases, respectively. In this chapter, quasi-soliton-collision-generated optical rogue waves are validated. Soliton collision process can be elucidated using the eigenvalues of the eigenvalue equation associated with the NLSE. Invariant property of the eigenvalues during the collision reveals that rogue waves are generated by the collision of two quasi-solitons.

This chapter is organized as follows. In section 3.2, numerical model and optical rogue wave generation in the NLSE-based model are presented as an introductory overview. The effects arising from TOD on extraordinary waves are demonstrated in section 3.3. In section 3.4, quasi-soliton collision generated optical rogue waves are validated. Finally, stability of quasi-soliton against the magnitude of TOD coefficient is explained.

3.2 Optical Rogue Wave Generation in the NLSE-based Model

Optical rogue wave generation using NLSE-based model is addressed in this section. At first, Eq. (2.29) is considered without TOD. To simulate the rogue wave phenomenon numerically, the NLSE is solved by split-step Fourier method (SSFM). Here, $W = 20$ was taken as the width of the time window. Time window is a specified data range that we consider during numerical

simulations instead of considering data from minus infinity to plus infinity. Accurate estimation can be obtained using wide time window with suitable sampling points inside the time window. The number of sampling points in the time window was set as 2^{11}. In addition, $\Delta Z = 10^{-5}$ was taken as the step size to Z-direction. The energy is defined as $E = \int_{-W/2}^{W/2} |u(Z,T)|^2 dT$. The average power is set as $E/W = 1$. In this study, a perturbed continuous wave (CW) was used as the initial condition, as shown in Fig. 2.3. To perturb the CW light, Gaussian noise with a normalized average power level of 10^{-5} was used. The rogue wave phenomenon was investigated by propagating the initial waveform until $Z = 2000$.

Fig. 3.1(a) presents the temporal waveform with respect to Z in the vicinity of the maximum peak power extraordinary wave. A rogue wave event, i.e., a waveform with extraordinary high peak power compared to other waves nearby, is clearly observed at a distance of $Z = 827.47$. When the peak power of a specific wave is greater than two times the significant wave height (SWH), it is called as a rogue wave event. The peak power of the extraordinary localized wave observed at a distance of $Z = 827.47$ is higher than two times the SWH. Therefore, this localized structure emerging in Fig. 3.1(a) can be denoted as a rogue wave event. The contour plot near the optical rogue wave is portrayed in Fig. 3.1(b). In addition, variations of imaginary part of eigenvalues $2\mathrm{Im}[\zeta]$, which was calculated using temporal waveform, are shown in Fig. 3.1(c) as a function of Z. The imaginary parts of the eigenvalues are almost constant around $Z = 827.47$; it can be regarded as collision of two solitons corresponding to two eigenvalues that generate the rogue wave. The imaginary part of eigenvalue corresponds to the amplitude of the soliton as shown in Eq. (2.11) and (2.12) in Chapter 2. Therefore, the imaginary part of the eigenvalue and the achieved soliton amplitude are compared to analyze the generation of rogue waves. Here, the imaginary parts of the eigenvalues are 2.1 and 1.8. Therefore, their sum is 3.9. However, the observed maximum peak power is 13.0. The corresponding amplitude is $\sqrt{13.0} = 3.6$, which is approximately equal to 3.9, which is the sum of the amplitude of two solitons. Therefore, a rogue wave is generated by collision of two solitons for this case. Moreover, soliton collision can be observed clearly in the contour plot near optical rogue wave generation. The maximum peak power of the generated rogue wave was 13 times higher than the average power of the initial waveform for $\sigma = 0$.

3.3 Numerical Demonstration of the Impact of TOD on Optical Rogue Waves

By using a procedure and simulation parameters similar to those for $\sigma = 0$ case, the rogue wave phenomenon for $\sigma \neq 0$ was analyzed. For a precise and quantitative evaluation, the magnitude of TOD was altered finely. The relation between the maximum peak power and the TOD coefficient was considered when an initial pulse propagates until $Z = 2000$. Numerical simulations were conducted for $|\sigma| \leq 0.03$. As shown by the blue solid line in Fig. 3.2, the maximum achieved peak power of the extraordinary wave depends on the magnitude of the TOD coefficient. The peak is maximized around $|\sigma| \simeq 0.02$. The maximum achieved peak power of the optical rogue wave was 61.7 when $\sigma = -0.0186$. For $|\sigma| \leq 0.02$, the maximum achieved peak power increased with $|\sigma|$. However, the maximum achieved peak power decreased when $0.02 < |\sigma| \leq 0.03$. The tendency of

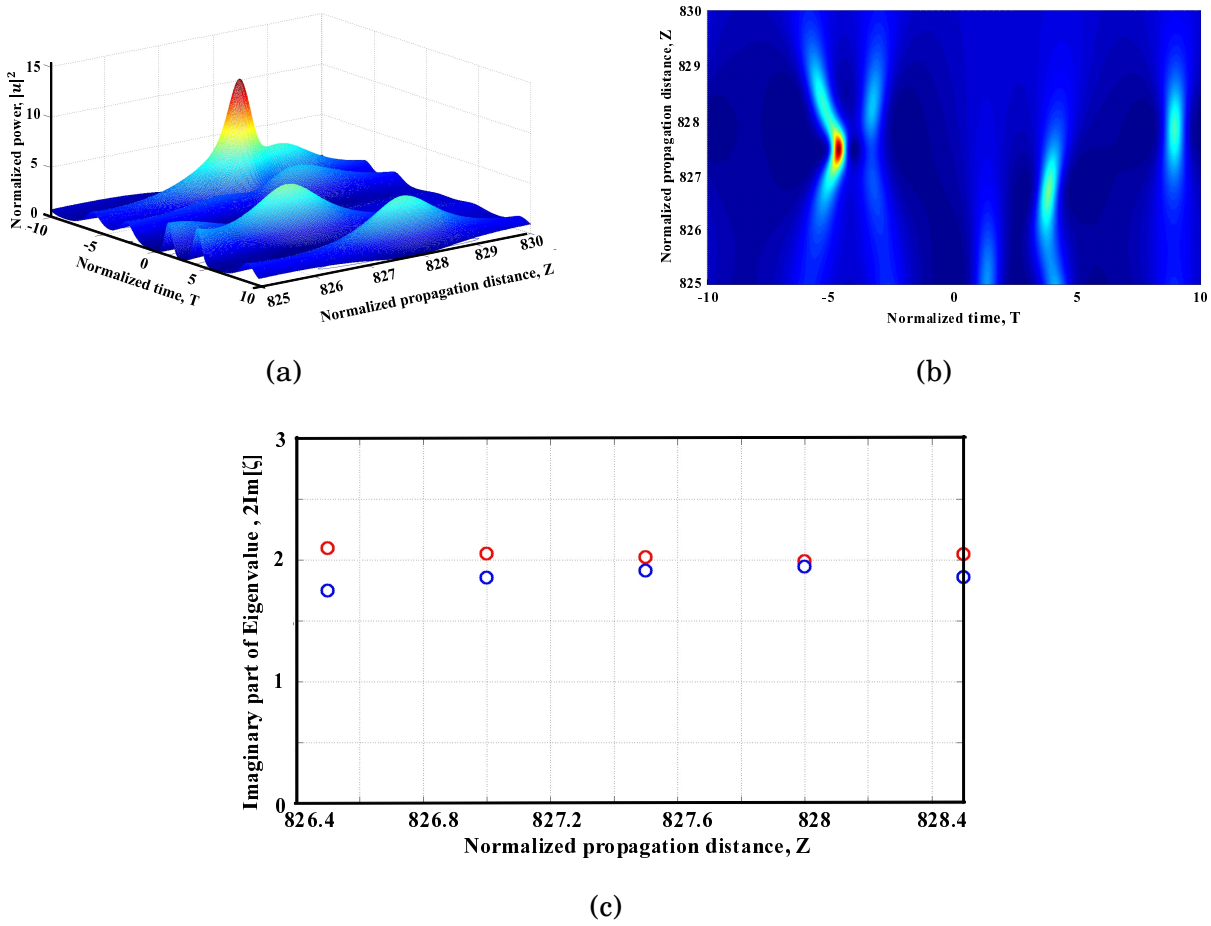

Fig. 3.1: (a) Observed optical rogue wave profile at $Z = 827.47$, (b) contour plot, and (c) variations of imaginary parts of eigenvalues near $Z = 827.47$ for $\sigma = 0$.

the peak power variation is dependent on the magnitude of TOD. Consequently, the maximum peak power is independent of the sign of the TOD. It depends only on the absolute value of TOD.

3.4 Generation Mechanism of NLSE-based Optical Rogue Wave

3.4.1 Numerical Simulation Method

Depending on the magnitude of TOD, the maximum achieved peak power changes according to some special behavior, as shown in Fig. 3.2. This special behavior raises the importance of analyzing the rogue wave phenomenon more precisely. To analyze optical rogue wave phenomena in detail, (a) the $\sigma = 0.015$ case was considered, which is a value of the TOD coefficient at which the maximum peak power is drastically changed. On the other hand, (b) the $\sigma = 0.02$ case was also analyzed, because the maximum peak power at $\sigma = 0.02$ is approximately 60 times higher than that of the initial wave. The following section shows the calculated wave profile, the contour plot of the wave height, and the imaginary part of the eigenvalues, at around the distance at which an extraordinary high peak power wave is observed.

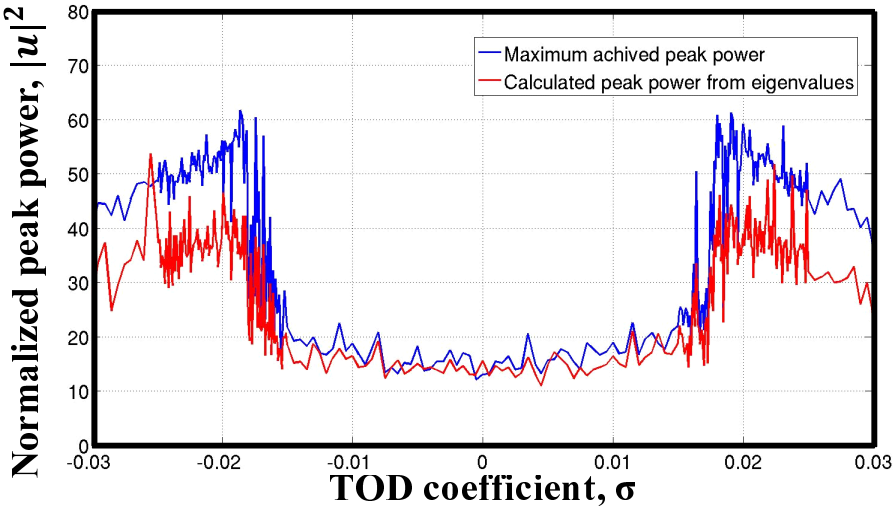

Fig. 3.2: Maximum achieved peak power vs. TOD coefficient.

3.4.2 Numerical Simulation Results

(a) $\sigma = 0.015$ **case**

Rogue wave generation for $\sigma = 0.015$ is analyzed in this subsection. The wave profile at distances around the value at which is extraordinary high peak power is observed is presented in Fig. 3.3(a), and Fig. 3.3(b) presents the contour plot of the wave profile. The maximally achieved value of the peak power was 22.0 at $Z = 1706.37$, which is slightly higher than that in the $\sigma = 0$ case. The imaginary parts of the eigenvalues at each distance, where the optical rogue wave generation is observed, are plotted in Fig. 3.3(c). The imaginary parts of the two eigenvalues are almost constant around $Z = 1706.37$. Those waves are quasi-solitons corresponding to solitons with eigenvalues of 2.5 and 1.8, respectively. Therefore, the sum of the amplitudes of two quasi-solitons is $2.5 + 1.8 = 4.3$. On the other hand, the peak power of the observed optical rogue wave is 22, the amplitude of which is $\sqrt{22.0} = 4.7$. Those amplitude values are almost identical. This means that the rogue wave is generated by collision between two quasi-solitons. Moreover, soliton collision can be observed clearly in the contour plot shown in Fig. 3.3(b).

(b) $\sigma = 0.02$ **case**

Extraordinary wave generation in the $\sigma = 0.02$ case is demonstrated in this subsection. Fig. 3.4(a) presents the wave profile over the distance where a highly localized wave is observed. An optical rogue wave event was clearly distinguished from other background waves at a distance of $Z = 1885.75$. The contour plot of the heights of those waves is presented in Fig. 3.4(b). In addition, the imaginary part of the eigenvalues $2\mathrm{Im}[\zeta]$ of those waves is also shown in Fig. 3.4(c). The maximal peak power, achieved at $Z = 1885.75$, is 59.1, which is extremely high compared to that in $\sigma = 0$ case. The imaginary parts of the two eigenvalues are evaluated as 6.1 and 0.1, respectively, as shown in Fig. 3.4(c), under the assumption that the observed rogue wave is generated by collision between two quasi-solitons. Their sum is $6.1 + 0.1 = 6.2$. On the other

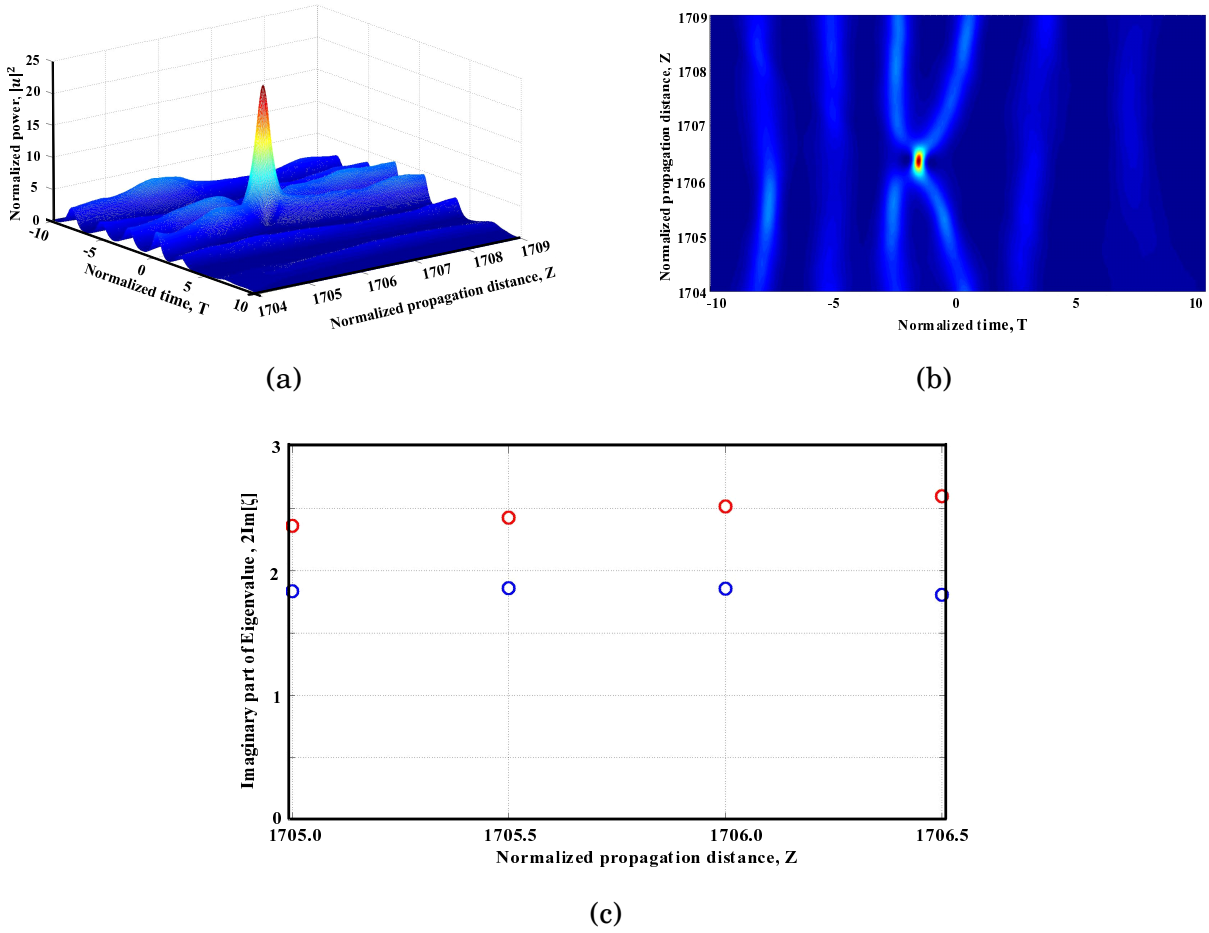

Fig. 3.3: (a) Observed localized wave profile at $Z = 1706.37$, (b) contour plot of the wave height, and (c) the imaginary part of eigenvalues near $Z = 1706.37$ for $\sigma = 0.015$.

hand, the amplitude of the observed optical rogue wave is $\sqrt{59.1} = 7.7$, which differs greatly from the other value. Moreover, quasi-soliton collision is difficult to observe even when optical rogue wave is generated, such that the contour plot apparently indicates the propagation of two single-solitons. Therefore, quasi-soliton collision cannot be attributed to the generation mechanism of optical rogue waves in this context.

The numerical simulation results presented for (a) $\sigma = 0.015$ and (b) $\sigma = 0.02$ show that a rogue wave can be generated because of different mechanisms depending on the magnitude of TOD. Hereinafter, rogue waves generated through quasi-soliton collision processes are specifically addressed. Numerical simulations were performed for $|\sigma| \leq 0.03$, under the same conditions and parameters as those of the previous analysis. Fig. 3.5 shows the imaginary parts of the two largest eigenvalues of the observed rogue wave. For $|\sigma| \leq 0.015$, two similar eigenvalues were observed. However, for $|\sigma| > 0.02$, the largest eigenvalue is much larger than the second largest one. $0.015 < |\sigma| \leq 0.02$ is the transition region of the two regions above.

The red line in Fig. 3.2 represents the calculated maximum peak power from the imaginary part of eigenvalues shown in Fig. 3.5 under the assumption of a quasi-soliton collision generating a rogue wave. For $|\sigma| \leq 0.015$, the calculated values agree with the maximum peak power achieved in the numerical simulation. Therefore, it is reasonable to consider the quasi-soliton

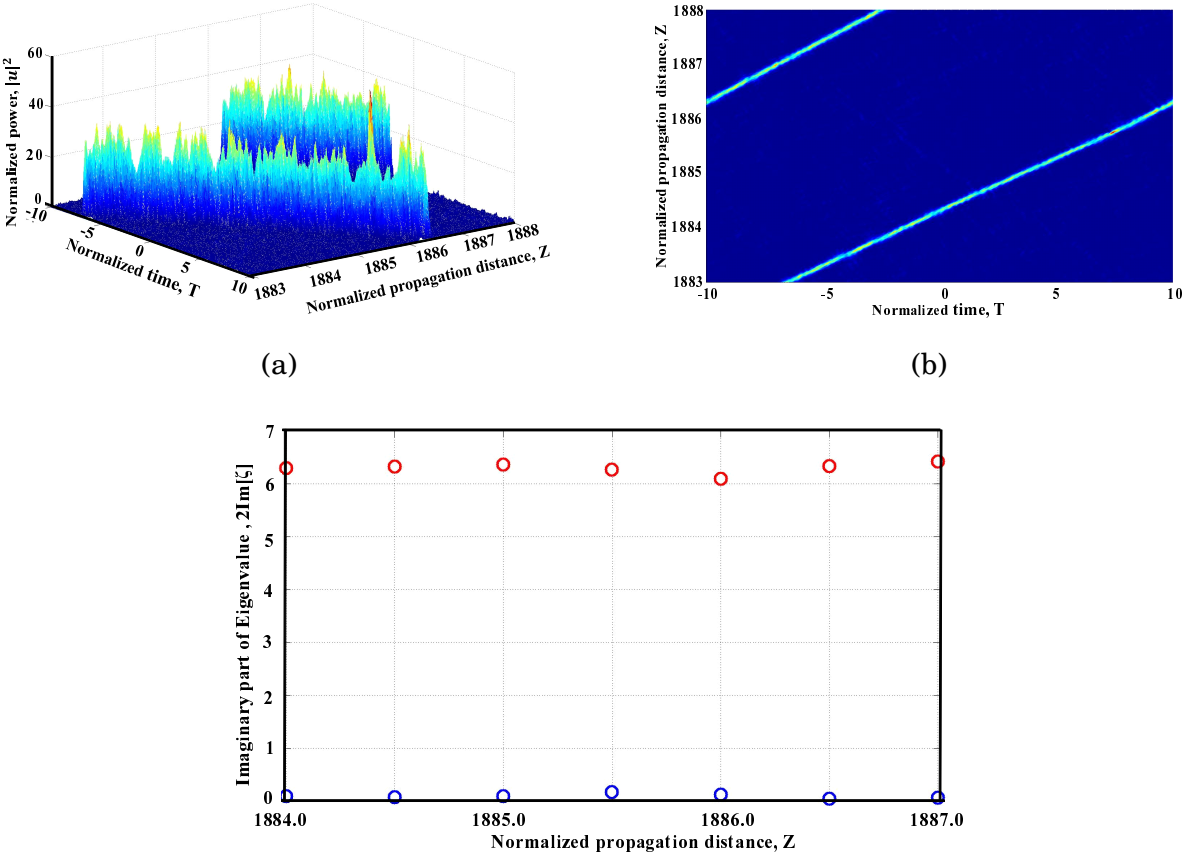

Fig. 3.4: (a) Wave profile around $Z = 1885.75$, (b) contour plot of the wave height, and (c) the imaginary part of the eigenvalue around $Z = 1885.75$. The TOD is $\sigma = 0.02$.

collision as the mechanism of rogue wave generation in this parameter region.

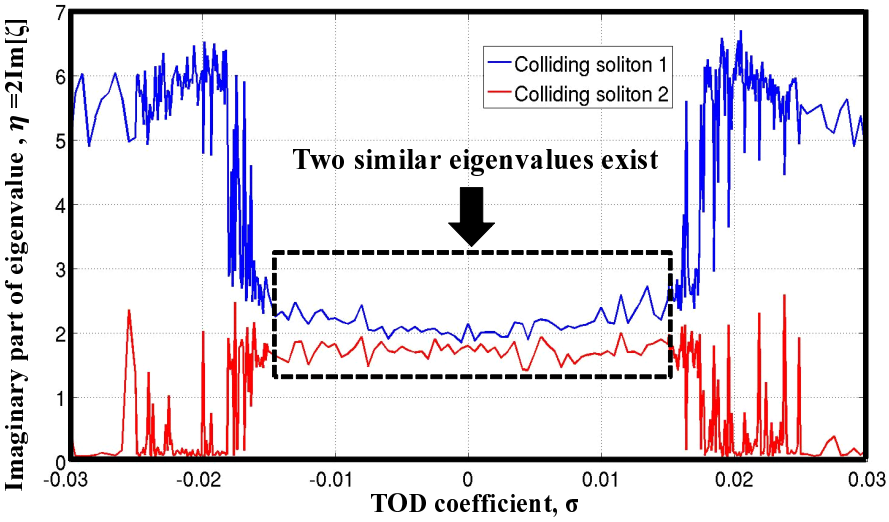

Fig. 3.5: Variations of imaginary parts of the two largest eigenvalues against TOD.

3.5 Stability of Optical Solitons Against TOD for the NLSE-based Model

Higher-order linear and nonlinear terms engender distortion of the pulse shape of optical solitons. The initial appearance of pulse shape is strongly changing during propagation because of dispersion and nonlinear effects. Pure soliton solutions cannot exist when $\sigma \neq 0$ in Eq. (2.29). Weak TOD of $|\sigma| \ll 1$ can be regarded as a perturbation to pure soliton. The soliton which behaves as a solitary wave is called a quasi-soliton. Although eigenvalue ζ in Eq. (2.30) is invariant regardless of u, which is obtained from the NLSE with $\sigma = 0$, the invariant of the eigenvalue is not guaranteed mathematically for $\sigma \neq 0$. In this regard, the relation between the stability of quasi-soliton and the magnitude of TOD was examined. The soliton pulse $u(0, T) = \eta \mathrm{sech}(\eta T)$ was used as an initial waveform, and the stability of the imaginary part of its eigenvalues after propagating over $Z = 20$ was investigated for $\sigma \neq 0$. Here, we define that a quasi-soliton is stable when its eigenvalue change is within 15% of the initial value, and is unstable otherwise. Fig. 3.6 shows the results, where the circle and cross indicate a stable and unstable quasi-solitons, respectively. For $|\sigma| \leq 0.03$, variation is small when the imaginary part of eigenvalue is less than 5. As shown in Fig. 3.5, the maximum value of the imaginary part of the eigenvalue is around 6 for $0.02 < |\sigma| \leq 0.03$. However, the imaginary part of the eigenvalue 6 is unstable for $0.02 < |\sigma| \leq 0.03$ as shown in Fig. 3.6. Therefore, the generation of a rogue wave cannot be explained by the quasi-soliton collision process for $|\sigma| > 0.02$. On the other hand, for $|\sigma| \leq 0.015$, the imaginary part of the eigenvalue becomes less than 5 as shown in Fig. 3.5 and the quasi-soliton is stable as shown in Fig. 3.6. Therefore, quasi-soliton collision can be regarded as the optical rogue wave generation mechanism for $|\sigma| \leq 0.015$. As described above, $0.015 < |\sigma| \leq 0.02$ is the transition region of those two regions.

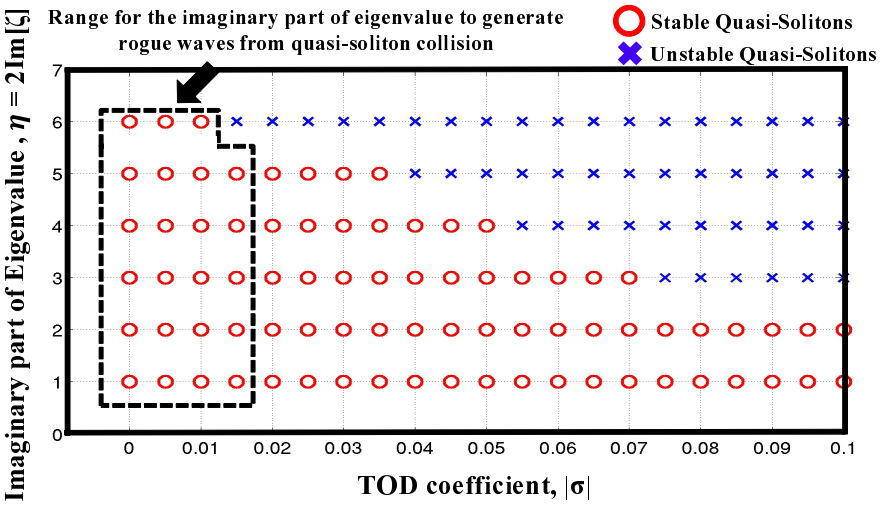

Fig. 3.6: Stability of quasi-solitons for different TOD coefficients.

3.6 Conclusions

Optical rogue wave generation using the simplest nonlinear evolution model has been demonstrated in this chapter. Optical rogue wave phenomena in optical fiber with a small TOD ($|\sigma| \leq 0.03$) were analyzed numerically. The maximally achieved peak power of optical rogue waves depends strongly on the magnitude of the TOD coefficient. For $|\sigma| \leq 0.02$, the maximum achieved peak power increased with $|\sigma|$. However, it decreased when $0.02 < |\sigma| \leq 0.03$. Consequently, the maximum achieved peak power was highest around $|\sigma| \simeq 0.02$. Moreover, it was demonstrated that the quasi-soliton collision process is the cause of optical rogue wave generation, from comparison of the observed peak power of the maximum amplitude rogue wave and the sum of the two largest eigenvalues obtained by solving the eigenvalue equation associated with NLSE. Quasi-soliton collision can be regarded as the cause of optical rogue wave generation mechanism for $|\sigma| \leq 0.015$ in the NLSE-based model. The generation mechanism of optical rogue wave for large TODs is clarified in the next chapter.

Chapter 4

Soliton Collision Generated Optical Rogue Waves for an HNLSE-based Model

4.1 Introduction

As the simplest prototype of the nonlinear evolution model, the nonlinear Schrödinger equation (NLSE) has played a pivotal role in the field of optical rogue waves. However, it is necessary to move beyond the standard NLSE description because of some unavoidable limitations. Dynamical and statistical behaviors of optical rogue waves depend on the type of nonlinear evolution model [45]– [49]. Behaviors of optical rogue waves for integrable higher-order NLSE (HNLSE) is mainly addressed in this chapter. Ablowitz, Kaup, Newell, and Segur (AKNS) have developed a systematic means of constructing integrable HNLSEs [83]. The eigenvalues of the equation associated with HNLSE are independent of the propagation distance. Because of the non-integrability of NLSE perturbed by third-order dispersion (TOD), the analysis of the previous chapter was applicable only for small TOD [53]. The effect of TOD on optical rogue waves also differs from model to model. As the investigation of rogue wave dependence on TOD has flourished in different fields, the effects of large TOD on optical rogue waves have become important. This chapter analyzes the effect of large TODs, different from Chapter 3. In terms of integrability, HNLSE is used to characterize the effect of larger TOD. The generation process of optical rogue waves is also an open question in various nonlinear models [54]. In addition to investigation of the effect of larger TOD, optical rogue wave generation processes are also validated, using an HNLSE model.

This chapter is organized as follows. In section 4.2, the eigenvalue equation associated with integrable HNLSE is presented. The effect of TOD on rogue wave phenomena analyzed by the HNLSE model is presented in section 4.3. The analysis described in section 4.4 reveals the emergence of optical rogue waves and the relation of TOD on their generation mechanisms. Observed rogue wave profiles for different TOD coefficients are presented in this section. In section 4.5, the soliton stability for the integrable HNLSE is discussed. Finally, soliton-collision-generated optical rogue waves are validated by the magnitude of TOD.

4.2 Eigenvalue Equation Associated with HNLSE

Inverse scattering transform (IST) is a method to solve an initial value problem in a wide-range of nonlinear evolution equations such as NLSE, Korteweg-de Vries (KdV) equation, modified Korteweg-de Vries (mKdV) equation, and the sine-Gordon equation [72], [84]. Initial scattering data is obtainable by the incident field, and the scattering data at a given distance can be determined by solving the linear evolution equation. The propagating field is reconstructed from the evolved scattering data. It is then applied to obtain the solutions of the original equations [78], [85]. To solve the different types of nonlinear evolution equations which are integrable by the IST, AKNS have developed procedures to solve a suitable scattering problem [83]. The AKNS formalism provides a model linked to several types of nonlinear evolution equations. The NLSE, the KdV equation, the mKdV equation, the sine-Gordon equation, and the considering integrable HNLSE shown in Eq. (4.2) can all be related to a unique eigenvalue equation in which eigenvalues are invariant with the evolution. A detailed description of IST is presented in appendix A.

The behavior of the complex envelope of a light wave propagating in a fiber can be represented by the widely known NLSE given by Eq. (2.29) in chapter 2. The initial value problem of Eq. (2.29) with no TOD term is solvable using the IST [86]. To analyze the effect of TOD on optical rogue waves, it is necessary to go beyond the standard NLSE description. Here, the complex envelope u in Eq. (2.29) is converted into the following form of U [87]:

$$U(Z,T) = u(Z,T) + 3i\sigma\left[\frac{\partial u(Z,T)}{\partial T} + 2u(Z,T)\int_{-\infty}^{T}|u(Z,T')|^2 dT'\right]. \tag{4.1}$$

First-order terms of parameter σ are only considered when we obtain integrable equation from Eq. (2.29) [88], [89]. An integrable HNLSE can be derived by substituting the conversion given by Eq. (4.1) into Eq. (2.29). The HNLSE can then be expressed as the following evolution equation:

$$i\frac{\partial U}{\partial Z} + \frac{1}{2}\frac{\partial^2 U}{\partial T^2} + |U|^2 U = i\sigma\left(\frac{\partial^3 U}{\partial T^3} + 6|U|^2\frac{\partial U}{\partial T}\right). \tag{4.2}$$

Particularly, the resulting HNLSE shown in Eq. (4.2) is also completely integrable using the IST with the same eigenvalue problem associated with Eq. (2.29) for the $\sigma = 0$ case. The conversion shown in Eq. (4.1) can be found by the fact that HNLSE has conserved quantities such as the energy and the momentum.

Next, the eigenvalue equation that can be solved analytically is briefly reviewed. The eigenvalue equation associated to Eq. (4.2) is represented as

$$\begin{cases} i\dfrac{\partial\psi_1}{\partial T} + U\psi_2 = \zeta\psi_1\,, \\ -i\dfrac{\partial\psi_2}{\partial T} - U^*\psi_1 = \zeta\psi_2\,, \end{cases} \tag{4.3}$$

where $\zeta \equiv (\kappa + i\eta)/2$ is a complex eigenvalue with two real numbers, κ and η, and $\psi_\ell(Z,T)$, $(\ell = 1,2)$ are the eigenfunctions [86]. As long as U is a solution of Eq. (4.2), eigenvalue ζ of Eq. (4.3) is invariant with Z. Eigenvalue ζ is calculable by three steps: (1) performing Fourier transformation of Eq. (4.3), (2) discretization in frequency domain to compute the convolution

integrals originated from the second term on the left-hand side of Eq. (4.3), and (3) solving the resultant matrix form eigenvalue problem using a standard numerical procedure as demonstrated in chapter 2.

4.3 Impact of TOD on Optical Rogue Waves for the HNLSE-based Model

To analyze the role of TOD in optical rogue wave generation, Eq. (4.2) is integrated numerically using the split-step Fourier method (SSFM). As an initial wave, a perturbed continuous wave (CW) of $P_0 = 1$ is used. Gaussian noise with a normalized power of 10^{-5} is superimposed on CW to perturb the CW light. The waveform evolution until $Z = 2000$ is simulated, from which the maximum peak power is extracted to identify a rogue wave. In the numerical calculation, the time window size, the number of sampling point in the time window, and the step size in the propagation direction are assumed to be $W = 40$, $N = 2^{11}$, and $\Delta Z = 10^{-5}$, respectively. A wide time window is used to demonstrate different types of optical rogue waves [90]. To address the generality, the average power $E/W = 1$ is utilized with the energy $E = \int_{-W/2}^{W/2} |U(Z,T)|^2 dT$.

For clarifying the effect of TOD on the HNLSE, Eq. (4.2) is solved for $|\sigma| \leq 0.1$. The magnitude of TOD is altered in an interval of $\Delta\sigma = 0.01$, and the relation between σ and the maximum peak power was calculated. To extract useful information to analyze the characteristics of these extraordinary peaks generated during the propagation, statistical description of complementary cumulative distribution function (CCDF) curve of the achieved peak power was adopted.

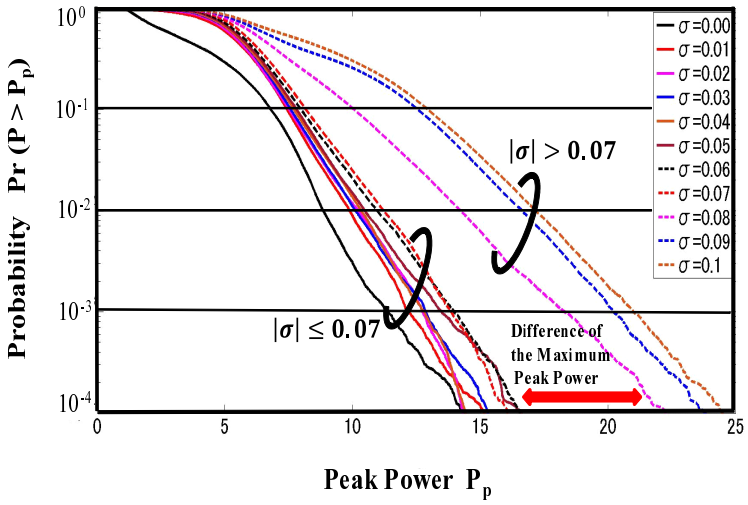

Fig. 4.1: CCDF curves for different TOD coefficients.

A CCDF curve presents the probability of peak power exceeding a given particular power level. Maximum peak power in the time window for each step is calculated during propagation until $Z = 2000$. Calculated maximum peak power in each step is regarded as a statistical data. The CCDF curves represent the probability of maximum peak power for each TOD coefficient. Curves in Fig. 4.1 respectively represent CCDFs for different TOD magnitudes. A notable observation is

that the maximum achieved peak power is increasing gradually with the magnitude of TOD. For $|\sigma| \leq 0.07$, the probability of generating extraordinary peaks guarantees some minimum level of output power. However, for $|\sigma| > 0.07$, the situation differs greatly because the maximum achieved peak power consists of peak excursions that occur much less often or at much lower probability than the average content of the waveform for $|\sigma| \leq 0.07$. Therefore, $|\sigma| \simeq 0.07$ plays as the threshold TOD value.

4.4 Generation Mechanism Evaluated by the HNLSE Model

4.4.1 Numerical Simulation Method

Threshold TOD values allow deep probing into phenomena related to optical rogue waves. Rogue wave phenomena are investigated for some specific TOD magnitudes. To analyze optical rogue wave phenomena in detail, $\sigma = 0.02$ and $\sigma = 0.1$ are analyzed for $|\sigma| \leq 0.07$ region and $|\sigma| > 0.07$ region, respectively.

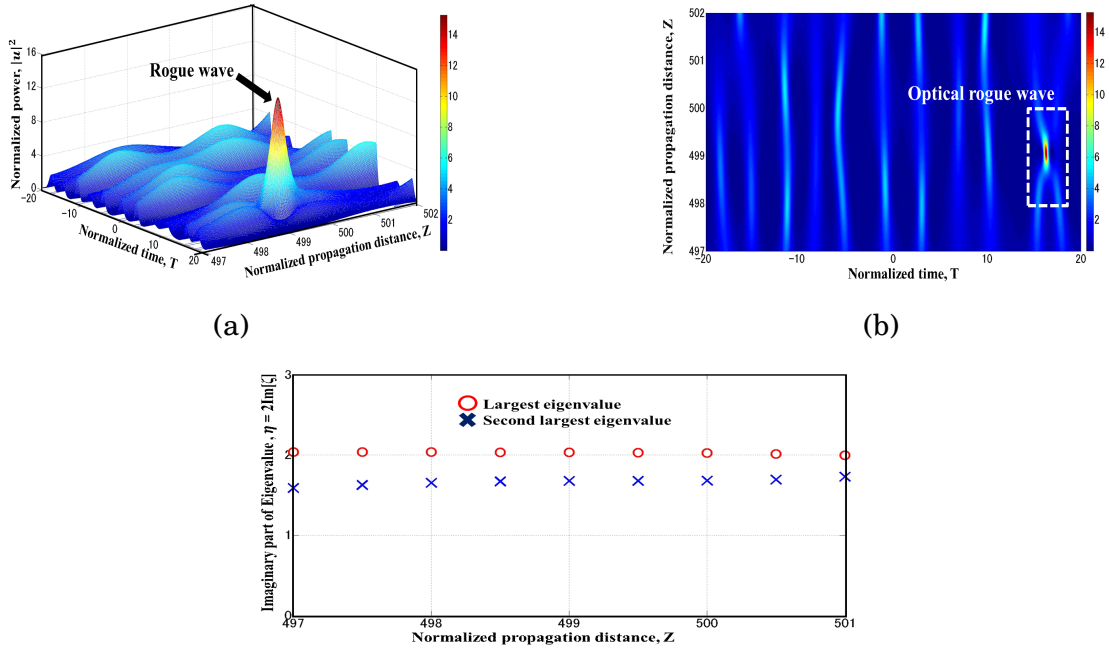

Fig. 4.2: (a) Wave profile, (b) the contour plot of the wave height, and (c) the imaginary part of the eigenvalue. The TOD is $\sigma = 0.02$.

(a) $\sigma = 0.02$ **case**

The rogue wave phenomenon for $\sigma = 0.02$ is demonstrated in this subsection. Fig. 4.2(a) plots the calculated wave profile, where a wave profile with an extraordinary high peak power level is emerged. The contour plot of the wave height is shown in Fig. 4.2(b), where the collision of two pulses is also highlighted. The maximum peak power is achieved as 15.3 at $Z = 499.07$. This extraordinary high peak power clearly indicates a rogue wave event. Fig. 4.2(c) presents the imaginary part of the two largest eigenvalues over the distance where the optical rogue

wave is generated. As shown in Fig. 4.2(c), the imaginary parts of the two eigenvalues are almost constant as 2.1 and 1.7, respectively, around $Z = 499.07$, which correspond to two colliding solitons. The sum of the amplitudes of the two soliton is 3.8 $(= 2.1 + 1.7)$. The observed peak power of the emerged optical rogue wave is 15.3. The corresponding amplitude is $(\sqrt{15.3} =)$ 3.9. The peak power value obtained by the numerical simulations and the sum of the two times the imaginary parts of eigenvalues are almost identical. Several wave profiles extracted from Fig. 4.2(a) are presented in Figs. 4.3(a) - (d). These figures show that rare and strong temporal optical events are initiated by modulational instabilities and are generated by collision of solitons. This convective nature, which is induced mainly by the TOD, renders the system convectively unstable in the $\sigma = 0.02$ case.

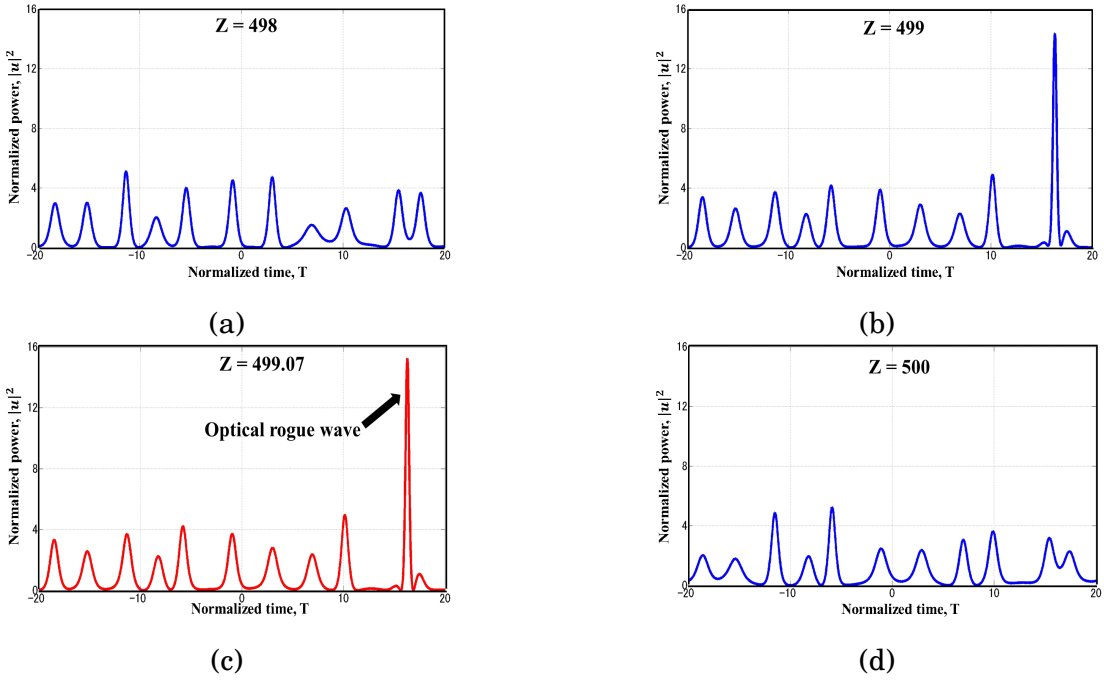

Fig. 4.3: Temporal wave profile at distances where the optical rogue wave is generated.

(b) $\sigma = 0.1$ **case**

Analysis of extraordinary wave generation for $\sigma = 0.1$ is presented in this section. The wave evolution over the distance where a rogue wave is generated is presented in Fig. 4.4(a), which reveals that the generated rogue wave has an extremely short lifetime. According to Fig. 4.4(a), the appearance of the rogue wave is different from the soliton collision generated rogue wave as it appears suddenly without any collision. The maximum peak power of 29.1 was observed at a distance of $Z = 1443.23$, where the wave field looks chaotic. The maximally achieved peak power was several times higher than the power with the highest probability. The peak power of the optical rogue wave was greater than the most probable ones and lower than other peaks in the surroundings. In this case, rogue wave generation is quite difficult to demonstrate because of its extremely short lifetime. Therefore, no soliton collision appears. The observed rogue wave is assumed to be generated through the collision of two solitons. The highest two eigenvalues at distances where the rogue wave is generated were computed using a finite size time window,

the imaginary parts of which are presented in Fig. 4.4(b). The two eigenvalues vary with the propagation distance, suggesting that the observed rogue wave did not occur by the collision of two solitons. To emphasize the difference between the $\sigma = 0.02$ and $\sigma = 0.1$ cases, it is helpful to compare the corresponding temporal power profiles at distances where the optical rogue wave is generated. The details of the evolution of the pulse power profile with the propagation distance are presented in Figs. 4.5(a) - (d). The $\sigma = 0.1$ case shows new dynamics such that soliton collision cannot be observed.

As described above, the HNLSE-based model indicates two kinds of a rogue wave: a rogue wave generated from soliton collision, and that appearing suddenly and disappearing with no trace. This result motivates a more precise analysis of the generation mechanism of optical rogue waves by the HNLSE-based model. In the following section, to evaluate the optical rogue wave generation mechanism quantitatively, we perform simulations assuming various TOD magnitudes with a small interval of $\Delta\sigma = 0.0005$. Moreover, the relation between σ and the maximum peak power was recalculated.

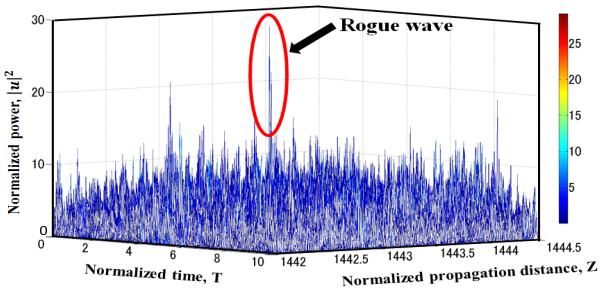

(a)

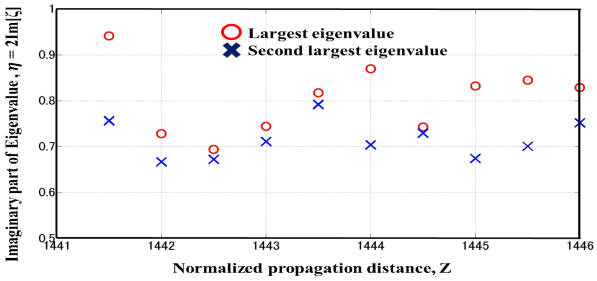

(b)

Fig. 4.4: (a) Observed optical rogue wave at $Z = 1443.23$ and (b) variations of imaginary parts of eigenvalues near $Z = 1443.23$ for $\sigma = 0.1$.

4.4.2 Numerical Simulation Results

The maximum achieved peak power when the TOD is altered with an interval of $\Delta\sigma = 0.0005$ is calculated, the result of which is indicated by the blue solid line in Fig. 4.6. The numerical simulations reveal that the achieved maximum peak power depends only on the absolute value of the TOD, but not on the sign. The maximum achieved peak power of the optical rogue wave is 37.3 when $\sigma = -0.0970$, which is approximately 37 times higher than that when $\sigma = 0$. As shown in Fig. 4.6, the peak power remained almost constant in a range of $|\sigma| \leq 0.075$. The max-

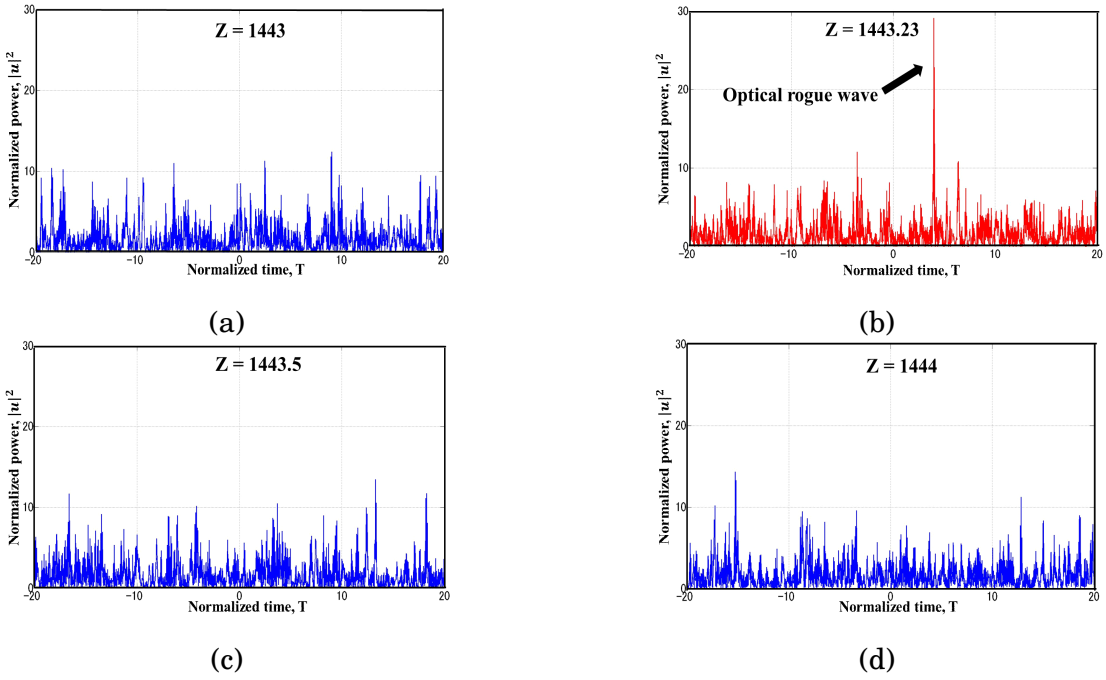

Fig. 4.5: Set of temporal wave profiles near the optical rogue wave at $Z = 1443.23$ for $\sigma = 0.1$.

imum achieved peak power is increasing gradually with the magnitude of TOD for $|\sigma| > 0.075$, representing the same scenario as shown in Fig. 4.1. These results confirm that optical rogue waves emerging from noise-seeded CW light in chaotic nature are induced by the TOD. Consequently, the TOD magnitude strongly influences the dynamics of these rare events. As a next step, the eigenvalues of associated equation to the HNLSE were calculated around the distance where a rogue wave is generated. The red dashed line in Fig. 4.6 represents the calculated peak power of the generating pulse using the largest two eigenvalues in the vicinity of the rogue wave. An excellent agreement is found in Fig. 4.6, between the peak power and the eigenvalues for $|\sigma| \leq 0.075$. For large TOD coefficients, on the other hand, a remarkable difference is shown between them. From these results, it can be concluded that the soliton collision is the dominant mechanism for rogue wave generation when $|\sigma| \leq 0.075$. Furthermore, the power is almost identical in this range. However, for $|\sigma| > 0.075$, rogue wave occurrence is expected to be caused by different physical mechanisms.

4.5 TOD in the HNLSE-based Model

The numerical simulation results in the previous section revealed that the TOD engenders the occurrence of rogue waves. The stability of soliton solutions differs depending on nonlinear evolution models. Particularly, when the higher-order dispersion terms exist in a nonlinear evolution model, the stability of soliton solutions must be considered before validating the results. Therefore, special attention should be devoted to the stability of solitons when the optical rogue wave generation process is described using the HNLSE-based model. The stability of soliton solutions of Eq. (4.2) is discussed in detail in this section. To quantify the stability of solitons in the HNLSE-based model, a numerical simulation was demonstrated for the fundamental soliton

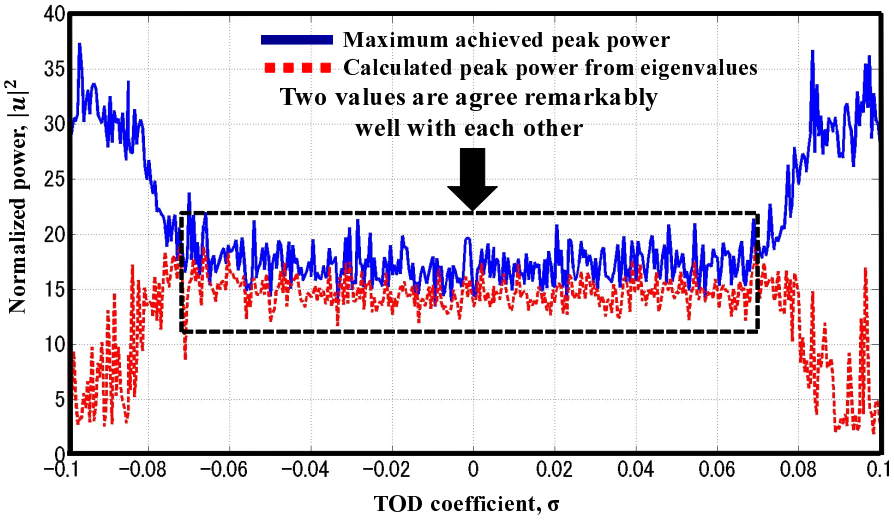

Fig. 4.6: Maximum achieved peak power vs. the TOD coefficient.

solution of Eq. (4.2). The IST is used to solve Eq. (4.2), the solution of which can be expressed as

$$U(Z,T) = \eta \,\mathrm{sech}[\eta(T+\sigma\eta^2 Z)] \exp\left(i\frac{\eta^2}{2}Z\right) \ . \tag{4.4}$$

This soliton solution with various values of amplitude η is used as an initial waveform at $Z = 0$. To emphasize the crucially important role of the TOD on the different amplitude pulses, the variation of the imaginary part of eigenvalues are evaluated when the pulse propagates until $Z = 100$. Here, a soliton with the eigenvalue whose imaginary part varies within 10% of the initial value is regarded as a stable soliton. The result is shown in Fig. 4.7, where a circles and crosses represent stable and unstable solitons, respectively. A salient difference between the HNLSE-based model (Fig. 4.7) and the NLSE-based model (Fig. 3.6) is that soliton solutions with the imaginary part of eigenvalue 6 are stable for small TOD coefficients. Soliton solutions with the imaginary part of eigenvalue 3 are stable for large TOD coefficients [53].

In the following, the two largest eigenvalues at a distance where a rogue wave is generated are examined.Their imaginary parts are shown in Fig. 4.8. In the region $|\sigma| \leq 0.075$, the imaginary part is almost constant around 2. According to Fig. 4.7, solitons with $\eta \leq 2$ is stable for $|\sigma| \leq 0.075$. Therefore, the region $|\sigma| \leq 0.075$ is an excellent agreement, indicating that soliton collision is significant in the generation mechanism of rogue waves in the HNLSE-based model. The magnitude of the TOD within this region strongly affects rogue wave formation dynamics. In the region $|\sigma| > 0.075$, on the other hand, eigenvalue-based prediction differs from the numerical simulation. The rogue wave generation dynamics in this region should be described by mechanisms other than soliton collision.

In the following, a comparison of the NLSE and HNLSE-based models is presented. First, the effect of the TOD shows different behaviors for the NLSE-based model and the HNLSE-based model, as shown in Fig. 4.9. The maximum achieved peak power was remained nearly constant at the range of $|\sigma| \leq 0.075$ for HNLSE-based model, different from the perturbed NLSE-based model. Moreover, soliton collision processes were the dominant optical rogue wave generation

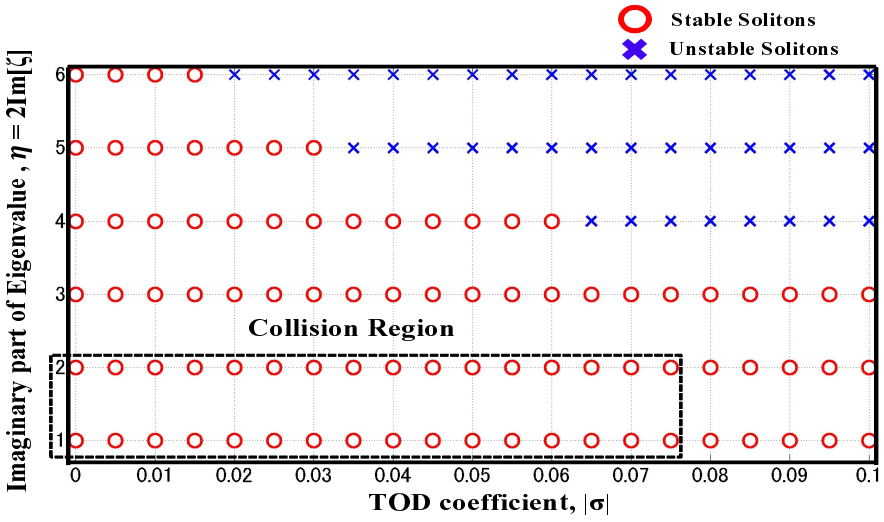

Fig. 4.7: Stability of solitons for different TOD.

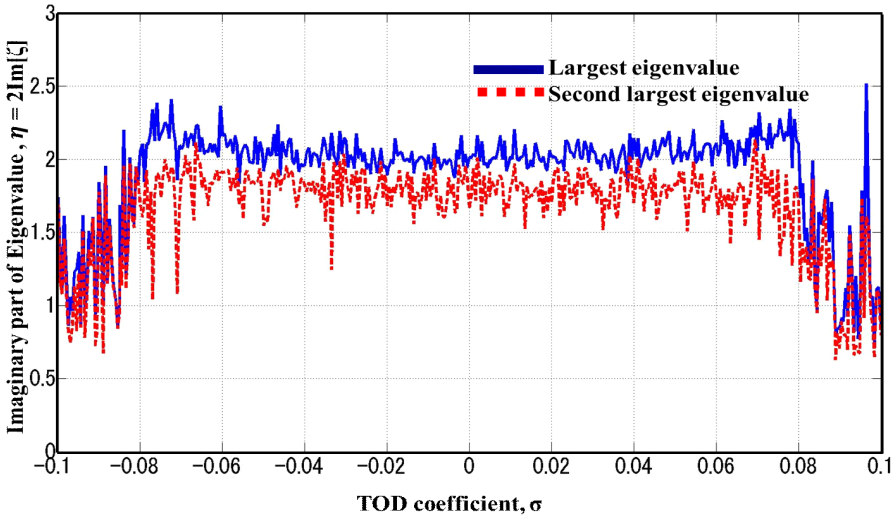

Fig. 4.8: Variations of the imaginary part of the two largest eigenvalues against TOD.

mechanism for $|\sigma| \leq 0.015$ [53] in the perturbed NLSE-based model. The parameter range of the soliton collision generated rogue waves is extended by five times ($|\sigma| \leq 0.075$) in the current HNLSE-based model compared with the previously stated perturbed NLSE-based model as shown in Fig. 4.9 [91].

4.6 Conclusions

In various physical contexts, several models have been developed to describe the rogue wave phenomenon. In order to indicate the crucially important role of the TOD on the dynamics and statistics of rogue waves, numerical simulations were performed based on the HNLSE-based model. The eigenvalues in conditions where rogue waves are generated were used. The impact of TOD shows different behavior in the HNLSE-based model compare to the NLSE-based model

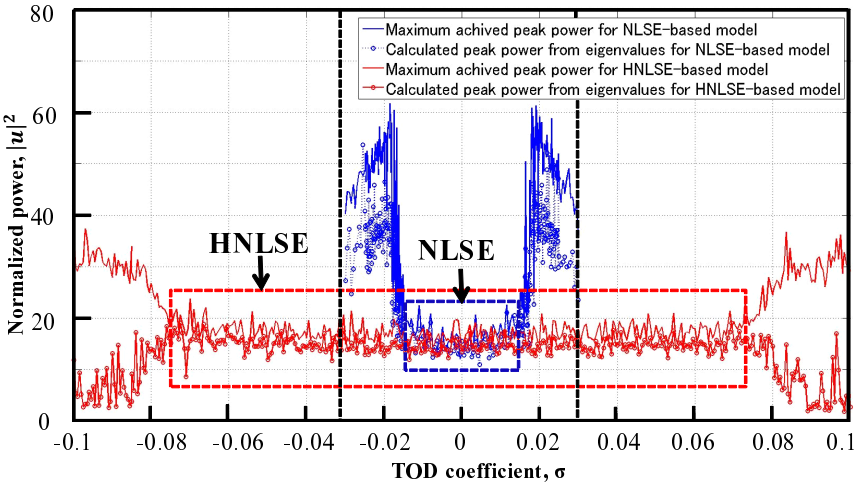

Fig. 4.9: Comparison between NLSE-based and HNLSE-based models.

stated in Chapter 3. Moreover, the parameter range to generate optical rogue waves from the collision of solitons is extended by five times in the HNLSE-based model. Similar behavior can be experienced in fields of nonlinear science different from fiber optics, such as fluid dynamics and plasma physics.

Chapter 5

Characterization of Soliton Fusion Phenomena

5.1 Introduction

Soliton fusion is a wave phenomenon resulting from interactions between co-propagating solitons. The process that two adjacent soliton shape pulses are merged into a single pulse is referred as soliton fusion. A strong soliton gains energy from a weaker soliton and merge into a single pulse when appropriate initial conditions are satisfied. Soliton fusion is strongly dependent on the temporal spacing, the frequency separation, and the phase difference between a pair of soliton pulses at the input. Because conditions for the soliton fusion occurring are extremely delicate, the fusion itself rarely occurs. The necessary condition in terms of soliton parameters has been investigated, based on the eigenvalues of solitons, in generation of high-intensity pulses, where the nonlinear Schrödinger equation (NLSE) was used to describe pulse propagation. Through such studies, soliton fusion has been observed in different fields. A complex and interesting example of soliton fusion is a rogue wave. A peculiar feature of a rogue wave generated from soliton fusion is unchanged amplitude for a long period after two solitons are merged. The objective of this chapter is to demonstrate soliton fusion resulting from interactions between solitons, using the eigenvalue of solitons to validate optical rogue wave generation via soliton fusion.

This chapter explains the concept of the soliton fusion phenomenon, and is organized as follows. In section 5.2, the fundamental concepts, the numerical model, and the effect of temporal spacing and frequency separation for soliton fusion are described. The effects of the frequency separation and the phase difference are presented in section 5.3. Fusion events for different soliton parameters are presented in this section. The authenticity assessment of numerical simulation results is discussed in section 5.4. Finally, the range of soliton parameters for achieving soliton fusion phenomenon is concluded.

5.2 Impact of Temporal Spacing and Frequency Separation on Soliton Fusion

5.2.1 Characterization of Soliton Parameters

The objective of this chapter is to demonstrate the fusion process of a pair of soliton pulses, using the soliton's eigenvalues explained in chapter 2. As characteristics of the soliton fusion process, colliding solitons are combined into a single giant solitary wave that propagates afterward while maintaining its shape and intensity of about the double of the parental solitons. Delicate conditions in terms of the temporal spacing, the frequency separation, and the phase difference are necessary for the soliton fusion occurring. The normalized NLSE in an anomalous dispersion regime can be represented as

$$i\frac{\partial u}{\partial Z} + \frac{1}{2}\frac{\partial^2 u}{\partial T^2} + |u|^2 u = 0 \,, \tag{5.1}$$

where Z, T, and $u(Z,T)$ respectively represent the normalized quantities of the propagation distance, the time in a frame moving with the group velocity, and the complex envelope of the electric field. This NLSE is solved for the initial waveform given by Eq. (2.26), using the split-step Fourier method (SSFM), in order to investigate the conditions for the fusion process. The time window size and the number of sampling points in the numerical calculations are chosen, respectively, as $W = 640$ and $N = 2^{10}$. Collision of solitons is accompanied by strong irradiation of a low-intensity dispersive wave, as stated in Chapter 2. Because of a large value of the group velocity, a part of those dispersive waves quickly pass out from the computational time window. To suppress the reflection of the dispersive waves from the computational window edges, absorbing boundary conditions are used, by application of a slightly increasing loss profile, to cancel out dispersive waves at the edges of the time window. A 30% wide loss profile is added to both sides of the computational window. In the following sections, the numerical simulation results on the effects of the temporal spacing and the frequency separation are demonstrated.

5.2.2 Numerical Simulation Results

To elucidate the effect of the temporal spacing and the frequency separation on the fusion process, numerical simulations are performed by setting $\Delta\theta = 0$ in Eq. (2.26). For simplicity, the condition $\Delta T = \Delta\nu$ is assumed at first. The real and imaginary parts of discrete eigenvalues and energy calculated using Eq. (2.26) with $\Delta T = \Delta\nu$ are depicted in Fig. 5.1. Eq. (2.26) has two discrete eigenvalues in two special cases: $(\kappa, \eta) = (0,1), (0,3)$ for $\Delta T = \Delta\nu = 0$, and $(\pm\Delta\nu/2, 1)$ for $|\Delta\nu| \gg 1$, which are already well known [78, 85]. Here, κ and η represent the real and the imaginary part of the eigenvalue, respectively. However, the other conditions of κ and η had not been investigated. Thus, we conducted numerical simulations to compute the eigenvalues in the unknown conditions the results of which is shown in Fig. 5.1. In the figure, in order to characterize the soliton fusion phenomenon, three particular regions are classified by the black dotted line: (1) co-propagation ($|\Delta\nu| = |\kappa_1 - \kappa_2| < 0.01$), (2) soliton fusion (when the imaginary part of the second largest soliton becomes 0, it is less than 0.03 in the simulation), and (3) repulsion (other than the above two conditions). Here, κ_1 and κ_2 denote the real part of the largest and second largest soliton, respectively. The black solid and broken lines in the

top diagram in Fig. 5.1 respectively represent the asymptotic line at $\Delta\nu/2$ and $-\Delta\nu/2$, which connect the origin. When the temporal spacing and the frequency spacing increase from $\Delta T = \Delta\nu = 0$, the amplitude of the weaker soliton decreases slightly, and is then damped to zero (region 1). The emergence of the dispersive wave represented by Eq. (2.28) can be associated with the dissipation of the weaker soliton. Here, Eq. (2.26) has only one discrete eigenvalue for $1.13 \leq \Delta T \leq 1.56$. Fusion is apparent in this region 2. Furthermore, when temporal spacing and frequency separation becomes larger, the weaker soliton reappears. The amplitude becomes 1 in both soliton in region 3. They propagate independently. The weaker soliton reappears gradually when the radiation of dispersion wave becomes low. Consequently, co-propagating solitons are apparent for $\Delta T < 1.13$ and $1.56 < \Delta T \leq 1.86$. The bifurcation point of the curve can be found at $\Delta T = 1.86$. Generally, sudden qualitative or topological change occurs in the bifurcation point, which is most commonly observed in mathematical studies and dynamic systems [92]. When $\Delta T > 1.86$, the two solitons propagate with different group velocities, as represented in the top diagram in Fig. 5.1. In region 3, repulsion of two solitary pulses emerging from the collision of the two solitons is apparent. Each energy level shown in Fig. 5.1 indicates that irradiation of the dispersive waves is enhanced in region 2 by disappearance of the weaker soliton. A good consistency is apparent in the energy conservation law for all regions. Table 5.1 summarizes the results for the $\Delta T = \Delta\nu$ case.

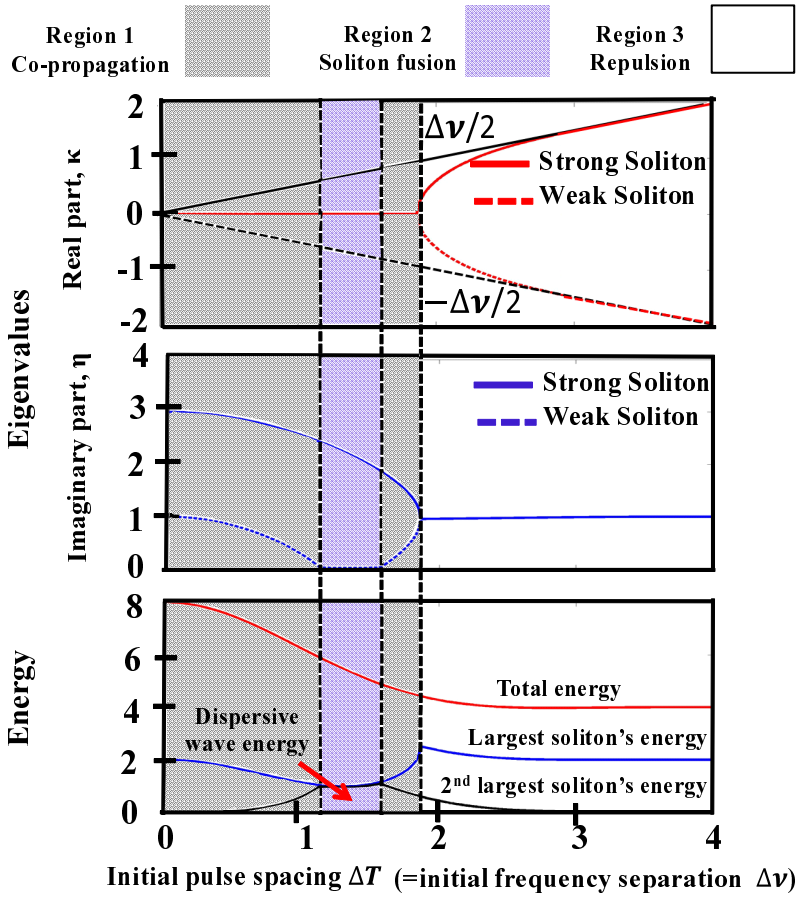

Fig. 5.1: Eigenvalues and energy of each pulse for $\Delta T = \Delta\nu$.

Table 5.1: Overview of the $\Delta T = \Delta\nu$ case.

Region	1	2	3
ΔT	$\lvert\Delta T\rvert < 1.13$ & $1.56 < \lvert\Delta T\rvert \leq 1.86$	$1.13 \leq \lvert\Delta T\rvert \leq 1.56$	$\lvert\Delta T\rvert > 1.86$
No. of solitons	2	1	2
Observed phenomenon	Co-propagation	Fusion	Repulsion

To verify the numerical simulation results obtained using Eq. (2.26) with $\Delta T = \Delta\nu$, two specific cases of $\Delta T = \Delta\nu = 0.8$ in region 1 and $\Delta T = \Delta\nu = 1.3$ in region 2 were examined more precisely. The peak power along the propagation distance in these two specific cases are portrayed in Fig. 5.2, where the peak power largely oscillates with the propagation distance for $\Delta T = 0.8$ because two solitons coexist for this case. For $\Delta T = 1.3$, on the other hand, the peak power approaches 5 while oscillating with the propagation distance. The power calculated from the amplitude is $(2.24)^2 = 5.02$. The calculated power from the amplitude and the achieved power after propagation are almost identical. Consequently, the amplitude calculation in regions 1 and 2 indicates that the soliton fusion can only occur in region 2.

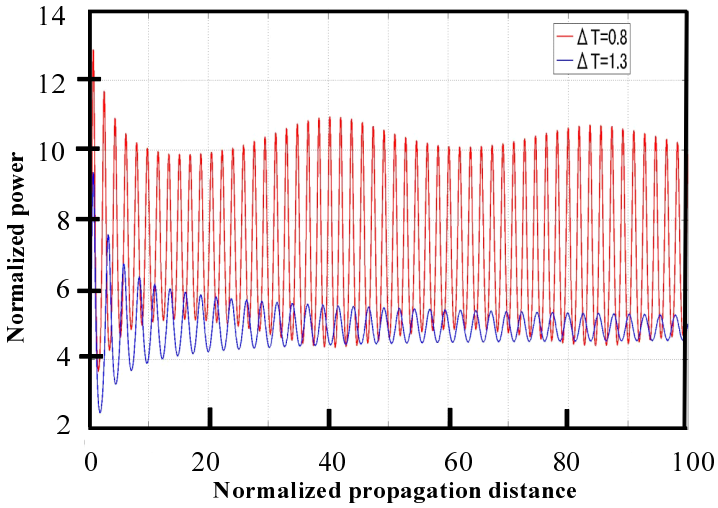

Fig. 5.2: Variation of peak power of the field for the $\Delta T = \Delta\nu$ case.

Fig. 5.3 shows the soliton period calculated using Eq. (2.9) and the interval between the peaks for $\Delta T = \Delta\nu$, where the soliton period increases with the pulse spacing. The analytical and numerical simulation results mutually agree well. The soliton period is increasing with the pulse spacing.

The initial conditions of $\Delta T = \Delta\nu$ is assumed in the above. In order to investigate the soliton fusion phenomenon in more detail, the similar simulation was conducted for various ΔT and $\Delta\nu$ over a wide range. The results are presented in Fig. 5.4. Most of the soliton parameters which generate soliton fusion exist above $\Delta\nu \geq 0.88\Delta T$. Repulsing solitons are appearing in region 3. The initial conditions of the pulse spacing and the frequency separation to produce either soliton

fusion or co-propagating solitons are expected to be positioned over a range below the blue solid line in Fig. 5.4. Optical solitons in region 2 can be related to generation of optical rogue waves through the soliton fusion process.

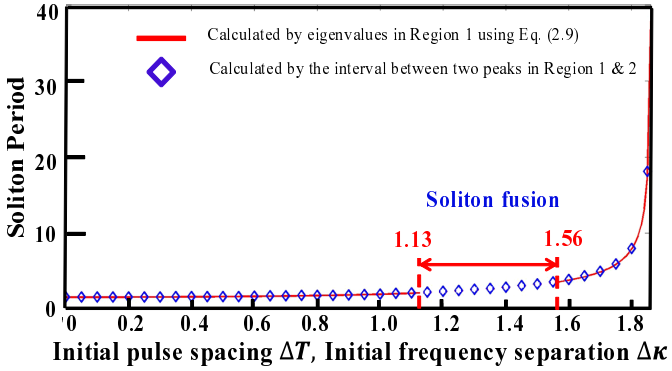

Fig. 5.3: Soliton period for the $\Delta T = \Delta\nu$ case.

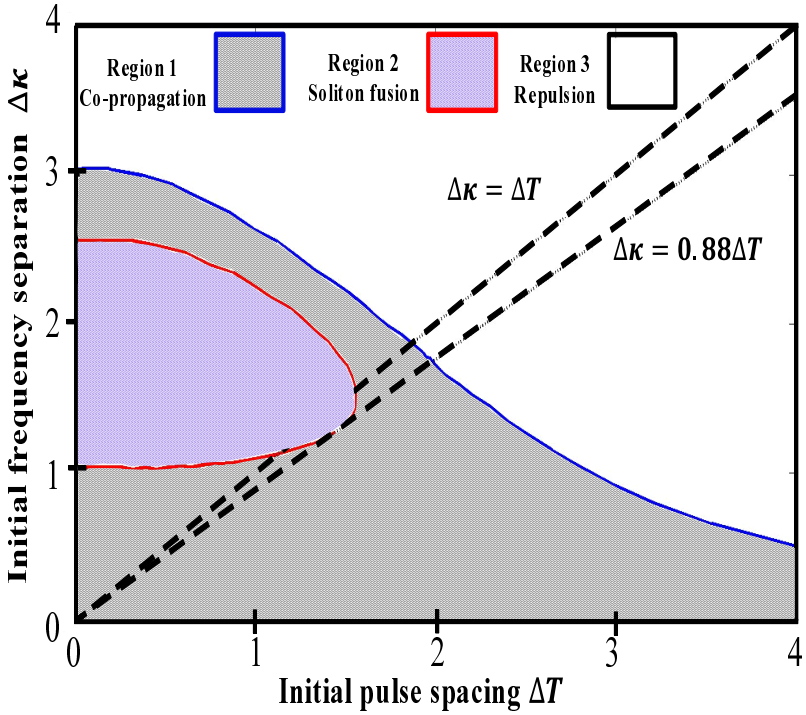

Fig. 5.4: Ranges classified with respect to ΔT and $\Delta\nu$ for $\Delta\theta = 0$ case.

5.3 Impact of Frequency Separation and Phase Difference on Soliton Fusion

The effects of the phase difference on the fusion process of two simultaneously launched solitons are investigated in this section. An initial time interval of $\Delta T = 1.3$ is chosen as a specific

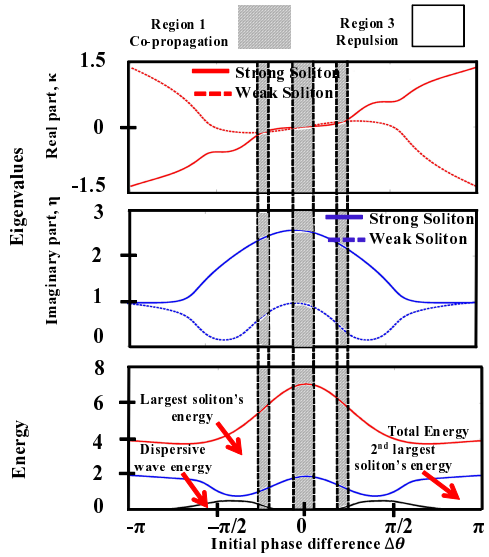

(a) $\Delta\nu = \Delta\theta$ case.

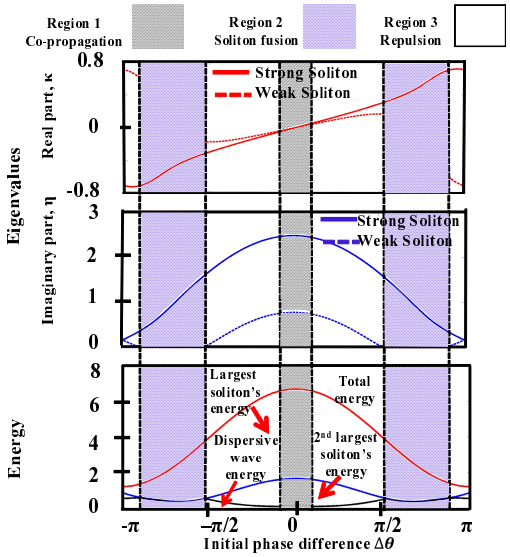

(b) $\Delta\nu = 0.5$ case.

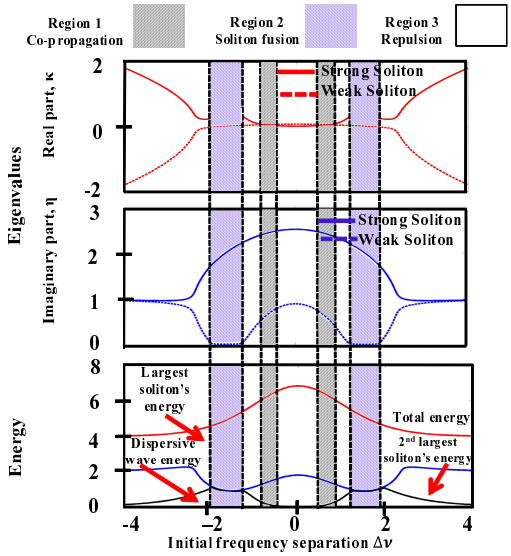

(c) $\Delta\theta = 0.125\pi$ case.

Fig. 5.5: Variation of eigenvalues and energy assignment for three cases when $\Delta T = 1.3$.

case for the soliton fusion, as in the preceding section. First, the real and imaginary parts of discrete eigenvalues and the energy are calculated using Eq. (2.26) with $\Delta\nu = \Delta\theta$. The result is shown in Fig. 5.5(a). Soliton fusion cannot be observed for phase differences of $-\pi \leq \Delta\theta \leq \pi$ in this case. Next, conditions of $\Delta\nu = 0.5$ and $\Delta\theta = 0.125\pi$ are examined. The results are portrayed respectively in Figs. 5.5(b) and (c). Soliton fusion is apparent when $0.52\pi \leq |\Delta\theta| \leq 0.91\pi$ in the $\Delta\nu = 0.5$ case, and is observed when $1.29 \leq |\Delta\nu| \leq 1.95$ in the $\Delta\theta = 0.125\pi$ case. Tables 5.2 and 5.3 present the respective overviews of the $\Delta\nu = 0.5$ and $\Delta\theta = 0.125\pi$ cases for $\Delta T = 1.3$.

In order to investigate the soliton fusion phenomenon more precisely, the relation between the observed phenomena and the initial conditions of the phase difference and the frequency separation was examined. Such an evolution map is expected to indicate particular features, revealing signatures of the soliton fusion. The results are presented in Fig. 5.6, where region 2

denotes a parameter region in which the soliton fusion is observed.

The numerical simulation results were confirmed by observing variation of the peak power of the field. Two specific cases $\Delta\theta = 3\pi/4$ in region 2 and $\Delta\theta = \pi/2$ in region 3 for $\Delta\nu = 0.5$ were studies in more detail. The peak power as a function of the propagation distance for those two specific cases are presented in Fig. 5.7. In the $\Delta\theta = \pi/2$ case, the peak power oscillates with the propagation distance, because two solitons coexist. The power in the $\Delta\theta = 3\pi/4$ case approaches 0.47 with the propagation distance. The power calculated from the amplitude is $(0.68)^2 = 0.46$. The observed and the calculated amplitudes are almost identical. Eventually, fusion can occur only in region 2.

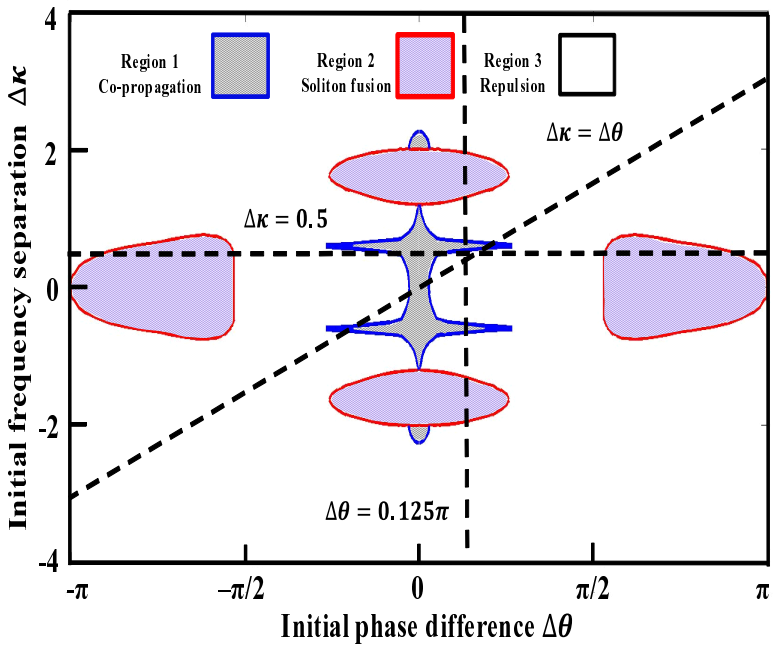

Fig. 5.6: Classified ranges with respect to $\Delta\theta$ and $\Delta\nu$ for the $\Delta T = 1.3$ case.

Table 5.2: Overview of $(\Delta T, \Delta\nu) = (1.3, 0.5)$ case.

Region	1	2	3
$\Delta\theta$	$\lvert\Delta\theta\rvert \leq 0.08\pi$	$0.52\pi \leq \lvert\Delta\theta\rvert \leq 0.91\pi$	$0.08\pi < \lvert\Delta\theta\rvert < 0.52\pi$ & $0.91\pi < \lvert\Delta\theta\rvert \leq \pi$
No. of solitons	2	1	2
Observed phenomenon	Co-propagation	Fusion	Repulsion

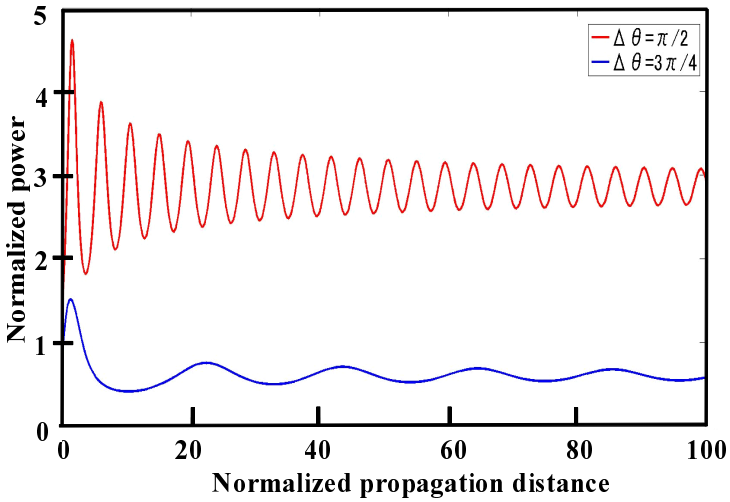

Fig. 5.7: Variation of peak power of the field for $\Delta\nu = 0.5$ and $\Delta T = 1.3$.

Table 5.3: Overview of $(\Delta T, \Delta\theta) = (1.3, 0.125\pi)$ case.

Region	1	2	3
$\Delta\nu$	$0.70 \leq \lvert\Delta\nu\rvert \leq 0.79$	$1.29 \leq \lvert\Delta\nu\rvert \leq 1.95$	$\lvert\Delta\nu\rvert < 0.70$ & $0.79 < \lvert\Delta\nu\rvert < 1.29$ & $\lvert\Delta\nu\rvert > 1.95$
No. of solitons	2	1	2
Observed phenomenon	Co-propagation	Fusion	Repulsion

5.4 Discussion on Numerical Simulation Result Authentication

Soliton fusion dramatically demonstrates a role of the initial conditions in interactions between optical pulses. Pulses are fused into a single pulse when the pulse spacing and the frequency separation are nearly zero [65]. Our numerical simulation results revealed that the amount of the pulse spacing, the frequency separation, and the phase difference engender the occurrence of soliton fusion. The energy conservation law was also be used to quantify our numerical simulation results.

A detailed description of the pulse spacing and the frequency separation in the $\Delta\theta = 0$ case is summarized in Table 5.4, which concludes that soliton fusion occurs only in region 2. The table also classifies κ and η in each region. Two solitons exist in region 1 and region 3. Region 2 has only one soliton because the weaker soliton is distinguished completely. A dispersive wave is strongly irradiated when the weaker soliton disappears. The detailed characteristics for the frequency separation and the phase difference for $\Delta T = 1.3$ are presented in Table 5.5. Variation of κ and η can be summarized as shown in Table 5.5. Two solitons exist in region 3. Only one soliton exists in region 2, which supports the generation of soliton fusion.

Table 5.4: Variations of κ and η for the $\Delta\theta = 0$ case.

Region	1	2	3
No. of solitons	2	1	2
κ	$\kappa_1 = \kappa_2 = 0$	$\kappa_1 = 0$	$\kappa_1 = -\kappa_2$
η	$\eta_1 \neq \eta_2$	η_1 only	$\eta_1 = \eta_2 = 1$
Observed phenomenon	Co-propagation	Fusion	Repulsion

Table 5.5: Variations of κ and η for the $\Delta T = 1.3$ case.

Region	1	2	3
No. of solitons	2	1	2
κ	$\kappa_1 = \kappa_2$	κ_1 only	$\kappa_1 \neq \kappa_2$
η	$\eta_1 \neq \eta_2$	η_1 only	$\eta_1 \neq \eta_2$
Observed phenomenon	Co-propagation	Fusion	Repulsion

Delicate initial conditions were necessary to observe fusion processes. Solitons cannot be separated by further propagation once they are mutually fused. This fact should be taken into account in developing analytical models for soliton interactions governed by the NLSE.

Typical oblong shapes of some oceanic rogue waves resemble the shapes of optical rogue waves generated because of soliton fusion [12]. In optical communication systems in general, it is desired to launch pulses with a close temporal spacing for high data rates. However, mutual interactions of closely spaced co-propagating solitons can degrade the performance of soliton transmission systems [93].

5.5 Conclusions

The effects of the pulse spacing, the frequency separation, and the phase difference between solitary pulses on the soliton fusion phenomena have been studied based on eigenvalue analysis. The results show that the fusion process is quite sensitive to the initial condition of these parameters. Soliton interactions can be changed from attractive to repulsive after collision, depending on soliton parameters. Because of the interactions, solitons are merged together, where the resultant amplitude is significantly greater than the initial amplitude of other solitons. Soliton fusions occurred only in region 2, whereas regions 1 and 3 respectively feature the co-propagation and repulsion of solitons. Co-propagation and soliton fusion regions were identified when $|\Delta\nu| = |\kappa_1 - \kappa_2| < 0.01$ and the imaginary part of the second largest eigenvalue becomes 0 (it is less than 0.03 in the simulation), respectively. Solitons which satisfy the conditions other than the co-propagation and soliton fusion was regarded as repulsive solitons. Fusion of optical solitons can be regarded as a new scenario to generate optical rogue waves.

Chapter 6

Conclusions

This dissertation has been devoted to presentation of an analysis of rogue wave phenomena in optical fiber. A signature feature of rogue waves is their anomalously large amplitude. Work on rogue waves is a dynamic area of research. Rogue wave phenomena in an optical fiber have been analyzed using analytical tools referred to eigenvalues of solitons. Analysis objects, i.e. the nonlinear Schrödinger equation (NLSE)-based model and the higher-order NLSE (HNLSE)-based model, have been explained separately as well as soliton fusion phenomenon, which is the key factor for rogue wave generation, in each chapter. Since the publication of the pioneer paper by Solli *et al.* in 2007, rogue wave phenomena have become a dominant research topic in the field of nonlinear optics.

The third-order dispersion (TOD) of optical fibers renders systems unstable, leading to optical rogue waves. The effect of the TOD have been investigated, the results of which confirmed that the TOD of optical fibers engender generation of these extreme waves. Various mechanisms can be attributed to the rogue wave generation, including soliton collision, soliton fusion, and collision of Akhmediev breather (AB)s. Peregrine solitons and Kuznetsov–Ma solitons have also been reported as prototypes to describe optical rogue waves. Furthermore, wave turbulence was reported as a generation mechanism of rogue waves. By exploiting the eigenvalues of optical solitons, soliton collision has been demonstrated numerically, using the NLSE-based and the HNLSE-based nonlinear evolution models. Moreover, soliton fusion phenomena were analyzed using the same analytical tool. The main results achieved in this research were summarized in Chapters 3–5.

Following the introduction in Chapter 1, Chapter 2 presents the fundamental concepts related to rogue wave generation in optical fiber. The overview of optical solitons, including fundamental and higher-order solitons, were presented at the beginning of Chapter 2. Modulational instability (MI) was discussed as a key nonlinear phenomenon to initiate optical rare and extraordinary high peak power events inside an optical fiber. Soliton fission and interaction processes of solitons were described to inspire an idea on such concepts. Eigenvalue equations associated with the NLSE were discussed as an analytical tool for discussing optical rogue wave generation.

Chapter 3 is devoted to characterization of optical rogue wave generation using the NLSE-based model. In order to obtain an idea of rogue wave phenomena in optical fibers, we assumed a perturbed continuous wave (CW) as an initial waveform, which propagated until a normalized distance of $Z = 2000$ and generated an extraordinary wave generation in a zero TOD case. After

describing the generation of optical rogue waves in the zero TOD case, the effects of the TOD on optical rogue waves were numerically investigated, using the NLSE-based model with a TOD magnitude of $|\sigma| \leq 0.03$. It was shown that the maximally achieved peak power of optical rogue waves depends on the magnitude of the TOD coefficient, such that, as $|\sigma|$ increases from zero, the peak power increases, is maximal around $|\sigma| \simeq 0.02$, and then decreases for $0.02 < |\sigma| \leq 0.03$. The results also showed that the maximally achieved peak power depends only on the absolute value of the TOD, not on its sign. The generation mechanism of optical rogue waves based on the NLSE-based model was validated as the next step of this analysis. The maximum achieved peak power for the previous step was compared with the peak power calculated by the imaginary part of the eigenvalues in the vicinity of rogue wave generation. For $|\sigma| \leq 0.015$, two eigenvalues were observed to have similar values of the imaginary parts. Quasi-soliton collision can be regarded as the optical rogue wave generation mechanism for $|\sigma| \leq 0.015$ in the NLSE-based model. Finally in Chapter 3, the stability of the quasi-solitons against the TOD was demonstrated numerically as a proof-of-evaluation for the considered NLSE-based model.

Chapter 4 describes the numerical simulations, using the HNLSE-based model, to analyze optical rogue wave generated from soliton collision. In Chapter 3, because of the non-integrability of the NLSE, the effects of the TOD on rogue waves were analyzed only for small TOD coefficients. Thereupon, the effects of the TOD and the optical rogue wave generation mechanism for wider range were evaluated using the HNLSE-based model in Chapter 4. Regarding the dependency of the TOD in the HNLSE-based model, the maximum achieved peak power remained almost constant in a range of $|\sigma| \leq 0.075$. For $|\sigma| > 0.075$, the maximum achieved peak power increased gradually with the magnitude of the TOD. The power calculated from the largest two eigenvalues, when a rogue wave is generated, and the maximally achieved peak power were compared, in order to suggest the generation mechanism. Excellent agreement was found between the peak power and eigenvalues for $|\sigma| \leq 0.075$. Consequently, the soliton collision is the dominant mechanism for rogue wave generation for $|\sigma| \leq 0.075$. The stability of solitons were also investigated numerically, using the HNLSE-based model, in Chapter 4. The parameter range for soliton-collision based rogue waves to generate, obtained by the HNLSE-based model, is the five times wider than that obtained by the perturbed NLSE-based model.

Chapter 5 was devoted to demonstration of the effect of initial soliton parameters on soliton fusion phenomena. Soliton fusion can be regarded as a mechanism of optical rogue wave generation. In order to have an idea regarding soliton fusion, the fundamental concepts of soliton interactions were presented. The effects of soliton parameters were evaluated using eigenvalues of the solitons. First, the effects of the temporal spacing and the frequency separation were analyzed. The results apparently showed that the occurrence of soliton co-propagation, soliton fusion, and repulsion is sensitive to these soliton parameters. Soliton fusion occurs in region 2, where the imaginary part of the second largest eigenvalue becomes 0. Because the conditions for the soliton fusion to occur are extremely sensitive to the system parameters, the fusion itself is a very rare event. Next, the effects of the frequency separation and the phase difference were evaluated for a normalized temporal spacing of $\Delta T = 1.3$. According to the results of this evaluation, the initial soliton parameters such as temporal spacing and frequency separation should be small, while appropriate phase difference between two solitons is required to generate soliton fusion. Finally in Chapter 5, the range of the soliton parameter for soliton fusion phenomenon

to occur was found.

Soliton collision and fusion generated optical rogue waves in optical fiber were evaluated theoretically in terms of eigenvalues of solitons. Soliton collision was studied in a framework of classical nonlinear evolution equations: NLSE and HNLSE. Recently, as an approach to evaluate numerical and experimental results, eigenvalues have drawn interest in the field of optics [79]. No report of the relevant literature describes a study that employs eigenvalues to evaluate the rogue wave phenomenon. Suppression of the generation of optical rogue waves is important for optical fiber transmission systems. However, optical rogue waves can be used for some future applications, such as soliton fusion generated optical rogue wave propagation for long distances without distortion. Optical fiber loss was neglected to highlight the nonlinear and dispersive mechanisms of rogue wave formation dynamics, in Eq. (2.29), Eq. (4.2), and elsewhere in this research. Based on the guiding center theory [94], the effect of fiber loss can be omitted. It does not change the conclusions of this research qualitatively.

Appendix A

Normalization of nonlinear Schrödinger equation

The behavior of the complex envelope of a light wave propagating in a fiber can be described by

$$i\frac{\partial E}{\partial z} - \frac{\beta_2}{2}\frac{\partial^2 E}{\partial t^2} + \gamma|E|^2 E = -i\alpha E + i\frac{\beta_3}{6}\frac{\partial^3 E}{\partial t^3} \ . \tag{A.1}$$

Here, z [m], t [s], $E(z,t)$ [$\sqrt{\mathrm{W}}$], β_2 [s^2/m], β_3 [s^3/m], γ [$1/(\mathrm{m}\cdot W)$], and α [$1/\mathrm{m}$]are respectively represent the propagation distance, the time moving with the group velocity, the complex envelope of electric field, the group velocity dispersion (GVD), third order dispersion (TOD), nonlinear coefficient, and fiber loss coefficient. Here, by using the reference time t_0 [s], we define the normalized time T, normalized distance Z, and normalized complex envelope of electric field u as shown below:

$$\begin{cases} T=\dfrac{t}{t_0} \ , \\ Z=\dfrac{|\beta_2|}{{t_0}^2} z \ , \\ u=t_0\sqrt{\dfrac{\gamma}{|\beta_2|}}E \ . \end{cases} \tag{A.2}$$

Then, Eq. (A.1) can be converted into the following equation in anomalous dispersion ($\beta_2 < 0$) region.

$$i\frac{\partial u}{\partial Z} + \frac{1}{2}\frac{\partial^2 u}{\partial T^2} + |u|^2 u = -i\Gamma u + i\sigma\frac{\partial^3 u}{\partial T^3} \ , \tag{A.3}$$

where $\Gamma = \dfrac{{t_0}^2\alpha}{|\beta_2|}$ and $\sigma = \dfrac{\beta_3}{6|\beta_2|t_0}$. Consequently, we obtain the normalized equation which governs the behavior of an optical pulse propagating in a fiber.

GVD (β_2 [s^2/m]) and the dispersion parameter related to TOD (D_λ [$\mathrm{ps}/(\mathrm{nm}^2.\mathrm{km})$]) are given by

$$\beta_2 = -\frac{\lambda^2 D}{2\pi c} \ , \tag{A.4}$$

and

$$D_\lambda = -\frac{2D}{\lambda} + \left(\frac{2\pi c}{\lambda^2}\right)^2 \beta_3 \,, \tag{A.5}$$

where λ, D, and c represent the operating wavelength, dispersion parameter, and the speed of light, respectively.

Detailed description of the rogue wave generation in actual fiber transmission lines is also required to extend the results of this research into practical situation. Therefore, the actual values of the maximum achieved peak power, the distance for rogue wave generation, and the dispersion parameter related to TOD are estimated using fiber parameters of (a) dispersion shifted fiber (DSF) and (b) single mode fiber (SMF). $\sigma = 0.015$ case on NLSE-based model is considered as an example to present the actual values corresponding to the normalized values. Optical rogue wave was observed with normalized peak power 22.0 at normalized propagation distance $Z = 1706.37$ for $\sigma = 0.015$ case. t_0 is defined as 10 [ps] for both cases.

Table A.1: Parameters of DSF at wavelength 1550 [nm].

Symbol	Description	value
D	Dispersion Parameter	1.0 [ps/(nm.km)]
γ	Nonlinear Coefficient	0.52 [1/(km.W)]
α	Fiber Loss Coefficient	0.24 [dB/km]

(a) DSF case

Table A.1 presents DSF parameters at wavelength 1550 [nm]. According to Eq. (A.4) and $\sigma = \dfrac{\beta_3}{6|\beta_2|t_0}$, β_2 and β_3 respectively become $\beta_2 = -1.275 \times 10^{-27}$ [s^2/m] and $\beta_3 = -1.148 \times 10^{-39}$ [s^3/m]. Therefore, actual values of the maximum achieved peak power, the distance for rogue wave generation, and the dispersion parameter related to TOD can be obtained as

$$\begin{cases} |E|^2\text{=}27.32 \text{ [dBm]} \,, \\ z\text{=}1.338 \times 10^5 \text{ [km]} \,, \\ D_\lambda\text{=}0.705 \text{ [ps/(nm}^2\text{.km)]} \,. \end{cases} \tag{A.6}$$

Table A.2: Parameters of SMF at wavelength 1550 [nm].

Symbol	Description	value
D	Dispersion Parameter	17.0 [ps/(nm.km)]
γ	Nonlinear Coefficient	0.27 [1/(km.W)]
α	Fiber Loss Coefficient	0.24 [dB/km]

(b) SMF case

Actual values for the maximum achieved peak power, the distance for rogue wave generation, and the dispersion parameter related to TOD are obtained for SMF in this section. Table A.2 presents the SMF parameters at wavelength 1550 [nm]. β_2 and β_3 respectively become $\beta_2 = -2.167 \times 10^{-26}$ [s^2/m] and $\beta_3 = -1.950 \times 10^{-38}$ [s^3/m] for SMF. Therefore, actual value of the maximum achieved peak power, the distance for rogue wave generation, and the dispersion parameter related to TOD can be obtained as

$$\begin{cases} |E|^2\text{=}42.47 \text{ [dBm]} , \\ \\ z\text{=}7874 \text{ [km]} , \\ \\ D_\lambda\text{=}11.978 \text{ [ps/(nm}^2\text{.km)]} . \end{cases} \tag{A.7}$$

Consequently, high peak power optical rogue wave is generated inside SMF compare with the DSF case for $\sigma = 0.015$ case in NLSE-based model.

Finally, the possibility of rogue wave generation is discussed by considering the practical values. Typical value of D_λ of a DSF is approximately 10 times higher than the value listed in (A.6). Calculated σ, which corresponds to the normalized system becomes $\sigma = 0.0015$, for the typical $D_\lambda (= 0.07$ [ps/(nm^2.km)]) of DSF at 1550 [nm]. This is almost similar to zero TOD case in the NLSE-based model. Normalized peak power of 13.0 rogue wave can generate for this case. Therefore, the generating peak power is 13 times the initial waveform. However, $z = 1.338 \times 10^5$ [km] is far beyond the practical conditions. Therefore, rogue waves are scarcely observed in practical DSF systems. On the other hand, typical value of D_λ in SMF is considered to discuss the possibility of rogue wave generation inside SMF. The typical value of D_λ in SMF is $D_\lambda = 0.09$ [ps/(nm^2.km)] at 1550 [nm]. Therefore, σ becomes $\sigma = 0.0012$ for this typical D_λ in SMF at 1550 [nm]. Here also σ almost becomes zero and peak power of 13.0 rogue wave can generate as same as the DSF case. Moreover, the distance for rogue wave generation becomes $z = 7874$ [km]. This z is not far beyond the practical conditions. Therefore, the rogue waves can frequently generate in SMF systems.

Appendix B

Inverse Scattering Method

The inverse scattering method can solve an initial value problem of some partial differential equations including the nonlinear Schrödinger equation (NLSE) [72], [83], [95]. Gardner, Greene, Kruskal, and Miura have reported a method to solve an initial value problem of a nonlinear evolution equation that was first brought to light in the Korteweg-de Vries (KdV) equation given by Eq. (B.1) [96]:

$$\frac{\partial q}{\partial Z} + 6q\frac{\partial q}{\partial T} + \frac{\partial^3 q}{\partial T^3} = 0 \; . \tag{B.1}$$

Here, Z, T, and $q(Z,T)$ respectively represent the normalized quantities of the propagation distance, the time in a frame moving with the group velocity, and the complex envelope of the electric field. First, the KdV equation is transformed to a linear eigenvalue equation and a spatial evolution equation of the eigenfunction with respect to Z. Then, the initial value problem of the KdV equation is solved by utilizing the fact that the eigenvalue is invariant with Z and by adapting the idea of a direct and inverse scattering problem to the eigenvalue equation. This method is designated as inverse scattering. At that time, the inverse scattering was regarded as an effective method to solve only the initial-value problem of the KdV equation. Generalization of the inverse scattering method by Lax, Zakharov and Shabat found that inverse scattering method can also be used to solve the initial value problem of the NLSE [86] given by

$$i\frac{\partial V}{\partial Z} + \frac{1}{2}\frac{\partial^2 V}{\partial T^2} + |V|^2 V = 0 \; , \tag{B.2}$$

where Z, T, and $V(Z,T)$ respectively represent the normalized quantities of the propagation distance, the time in a frame moving with the group velocity, and the complex envelope of the electric field. With the direct and inverse scattering ideas, Eq. (B.2) can be solved for any given initial value $V(Z,0)$, the solution of which decays rapidly as $|T| \to \infty$. Moreover, this inverse scattering method is applicable to solve an initial value problem of the modified KdV (mKdV) equation and the sine-Gordon equation [98]. These results demonstrated the feasibility and the versatility of the inverse scattering method to solve certain physically interesting nonlinear partial differential equations. Shortly thereafter, Ablowitz, Kaup, Newell, and Segur (AKNS) developed a method to solve an initial value problem of a broad class of nonlinear evolution equations using that approach [83]. They were designated as inverse scattering transform (IST).

For example, it turns out the KdV, the mKdV, the NLSE, and the sine-Gordon equations can all be known to be related to one master eigenvalue problem.

B.1 Lax's Approach

The nonlinear evolution equation given by

$$\frac{\partial V}{\partial Z} = K(V) \tag{B.3}$$

is discussed in this section. In the above equation, K is a nonlinear operator acting on a scalar function $V(Z,T)$. Here, we introduce linear operators L and M that depend on the solution $V(Z,T)$ of Eq. (B.3). Assuming that L and M satisfy an operator equation given by

$$i\frac{\partial L}{\partial Z} = \Big[M, L\Big] = ML - LM \ , \tag{B.4}$$

then operator L satisfies the following eigenvalue equation:

$$L\Psi = \zeta\Psi \ , \tag{B.5}$$

where ζ represents an eigenvalue and Ψ expresses an eigenfunction. In Eq. (B.5), the eigenvalue ζ is independent of Z and the variation of eigenfunction Ψ with respect to Z satisfies

$$i\frac{\partial \Psi}{\partial Z} = M\Psi \ . \tag{B.6}$$

For a given L, Lax shows how to construct an associated operator M which satisfies Eq. (B.4). This is designated as Lax's approach and L and M are called Lax pair.

B.2 AKNS Formulation

The difficulties in Lax's approach are that one must guess a suitable L and then find an M to satisfy Eq. (B.4). As an alternative, AKNS proposed a technique which can be formulated generally as follows. Consider two linear equations of

$$\frac{\partial \mathbf{\Psi}}{\partial T} = N\mathbf{\Psi} \ , \tag{B.7}$$

and

$$\frac{\partial \mathbf{\Psi}}{\partial Z} = M\mathbf{\Psi} \ , \tag{B.8}$$

where $\mathbf{\Psi}$ represents the eigenfunction of an n-dimensional vector. Moreover, N and M are $n \times n$ matrices. Then, cross-differentiation (i.e., taking $\dfrac{\partial}{\partial Z}$ in Eq. (B.7), $\dfrac{\partial}{\partial T}$ in Eq. (B.8) and setting them equal) yields

$$\frac{\partial N}{\partial Z} - \frac{\partial M}{\partial T} + NM - MN = 0 \ . \tag{B.9}$$

This equation is fundamentally equivalent to Eq. (B.4). It turns out that, for a given N, a simple deductive procedure can be used to find M such that Eq. (B.9) contains a nonlinear evolution equation. For Eq. (B.9) to be effective, the associated operator N is expected to have a parameter that plays the role of an eigenvalue, say ζ, and which obeys $\dfrac{d\zeta}{dZ} = 0$.

A 2×2 eigenvalue problem is discussed here. The scattering problem of Zakharov and Shabat is modified as

$$\begin{pmatrix} \dfrac{\partial \Psi_1}{\partial T} \\ \dfrac{\partial \Psi_2}{\partial T} \end{pmatrix} = \begin{pmatrix} -i\zeta & q \\ r & i\zeta \end{pmatrix} \begin{pmatrix} \Psi_1 \\ \Psi_2 \end{pmatrix} . \tag{B.10}$$

It is noteworthy that when $r = -1$ or $r = \pm q^*$ (or $r = \pm q$ if q is real), physically significant nonlinear equations are obtained from the above formalization. Let

$$\begin{pmatrix} \dfrac{\partial \Psi_1}{\partial Z} \\ \dfrac{\partial \Psi_2}{\partial Z} \end{pmatrix} = \begin{pmatrix} A & B \\ C & D \end{pmatrix} \begin{pmatrix} \Psi_1 \\ \Psi_2 \end{pmatrix} \tag{B.11}$$

be an evolution equation corresponding to Eq. (B.10) with respect to Z, where A, B, C, and D respectively denote scalar functions independent of $\mathbf{\Psi}$. For Eqs. (B.10) and (B.11) to be compatible, a certain set of conditions should be satisfied on A, B, C, and D. Assuming that cross-differentiation of Eq. (B.10) and Eq. (B.11) are equal and that the eigenvalues are independent of Z, we obtain

$$\begin{cases} \dfrac{\partial A}{\partial T} = qC - rB \ , \\ \dfrac{\partial B}{\partial T} = -i2\zeta B + \dfrac{\partial q}{\partial Z} - 2qA \ , \\ \dfrac{\partial C}{\partial T} = i2\zeta C + \dfrac{\partial r}{\partial Z} + 2rA \ , \\ D = -A \ . \end{cases} \tag{B.12}$$

If A, B, and C are determined to satisfy Eq. (B.12), then the solvable nonlinear evolution equation Eq. (B.9) can be derived.

Because the eigenvalue ζ can have an arbitrary value (it might be small), we can assume an exact truncated power series in terms of ζ as a solution of Eq. (B.12). A simple expansion that yields an representative nonlinear evolution equation is expressed as

$$\begin{cases} A = A_3\zeta^3 + A_2\zeta^2 + A_1\zeta + A_0 \ , \\ B = B_3\zeta^3 + B_2\zeta^2 + B_1\zeta + B_0 \ , \\ C = C_3\zeta^3 + C_2\zeta^2 + C_1\zeta + C_0 \ . \end{cases} \tag{B.13}$$

Here, we substitute Eq. (B.13) into Eq. (B.12) and equate coefficients of the power of ζ.

The above procedure can be applied to any polynomial expansion in ζ. As an example, the results for the most significant cases are quoted. Polynomials in ζ to the third power are expressed

as

$$\begin{cases} A = a_3\zeta^3 + a_2\zeta^2 + \dfrac{1}{2}\left(2a_1 + a_3 qr\right)\zeta + a_0 + \dfrac{1}{2}a_2 qr - \dfrac{i}{4}a_3\left(q\dfrac{\partial r}{\partial T} - \dfrac{\partial q}{\partial T}r\right) , \\ B = ia_3 q\zeta^2 + \left(ia_2 q - \dfrac{1}{2}a_3\dfrac{\partial q}{\partial T}\right)\zeta + ia_1 q - \dfrac{1}{2}a_2\dfrac{\partial q}{\partial T} + \dfrac{i}{4}a_3\left(2q^2 r - \dfrac{\partial^2 q}{\partial T^2}\right) , \\ C = ia_3 r\zeta^2 + \left(ia_2 r - \dfrac{1}{2}a_3\dfrac{\partial r}{\partial T}\right)\zeta + ia_1 r + \dfrac{1}{2}a_2\dfrac{\partial r}{\partial T} + \dfrac{i}{4}a_3\left(2qr^2 - \dfrac{\partial^2 r}{\partial T^2}\right) , \end{cases} \tag{B.14}$$

and the evolution equations of

$$\begin{cases} \dfrac{\partial q}{\partial Z} + \dfrac{i}{4}a_3\left(\dfrac{\partial^3 q}{\partial T^3} - 6qr\dfrac{\partial q}{\partial T}\right) + \dfrac{1}{2}a_2\left(\dfrac{\partial^2 q}{\partial T^2} - 2q^2 r\right) - ia_1\dfrac{\partial q}{\partial T} - 2a_0 q = 0 , \\ \dfrac{\partial r}{\partial Z} + \dfrac{i}{4}a_3\left(\dfrac{\partial^3 r}{\partial T^3} - 6qr\dfrac{\partial r}{\partial T}\right) - \dfrac{1}{2}a_2\left(\dfrac{\partial^2 r}{\partial T^2} - 2qr^2\right) - ia_1\dfrac{\partial r}{\partial T} + 2a_0 r = 0 \end{cases} \tag{B.15}$$

can be found.

Evolution equations of physical interest are obtained as special cases. Taking $a_0 = a_1 = a_2 = 0$, $a_3 = -4i$, and $r = -1$, the KdV equation represented in Eq. (B.1) is obtainable. On the other hand, $a_0 = a_1 = a_2 = 0$, $a_3 = -4i$, and $r = \mp q$, the mKdV equation is obtainable. The $q = iV$ and $r = iV^*$ cases used in this study are summarized below. If $a_0 = a_1 = 0$, $a_2 = -i$, and $a_3 = -4ib_3$ in Eqs. (B.10), (B.11), (B.14), and (B.15), we obtain

$$i\frac{\partial V}{\partial Z} + \frac{1}{2}\frac{\partial^2 V}{\partial T^2} + |V|^2 V = ib_3\left(\frac{\partial^3 V}{\partial T^3} + 6|V|^2\frac{\partial V}{\partial T}\right) . \tag{B.16}$$

In this case, Eqs. (B.10) and (B.11) can be expressed as

$$\begin{cases} \dfrac{\partial \Psi_1}{\partial T} = -i\zeta\Psi_1 + iV\Psi_2 , \\ \dfrac{\partial \Psi_2}{\partial T} = i\zeta\Psi_2 + iV^*\Psi_1 , \end{cases} \tag{B.17}$$

$$\begin{cases} \dfrac{\partial \Psi_1}{\partial Z} = A\Psi_1 + B\Psi_2 , \\ \dfrac{\partial \Psi_2}{\partial Z} = C\Psi_1 - A\Psi_2 , \end{cases} \tag{B.18}$$

where

$$\begin{cases} A = ib_3\left\{4\zeta^3 - 2|V|^2\zeta + i\left(V\dfrac{\partial V^*}{\partial T} - \dfrac{\partial V}{\partial T}V^*\right)\right\} - i\left(\zeta^2 - \dfrac{1}{2}|V|^2\right) , \\ B = ib_3\left\{-4\zeta^2 V - 2i\dfrac{\partial V}{\partial T}\zeta + 2|V|^2 V + \dfrac{\partial^2 V}{\partial T^2}\right\} + i\left(V\zeta + \dfrac{i}{2}\dfrac{\partial V}{\partial T}\right) , \\ C = ib_3\left\{-4\zeta^2 V^* - 2i\dfrac{\partial V}{\partial T}\zeta + 2|V|^2 V^* + \dfrac{\partial^2 V^*}{\partial T^2}\right\} + i\left(V^*\zeta - \dfrac{i}{2}\dfrac{\partial V^*}{\partial T}\right) . \end{cases} \tag{B.19}$$

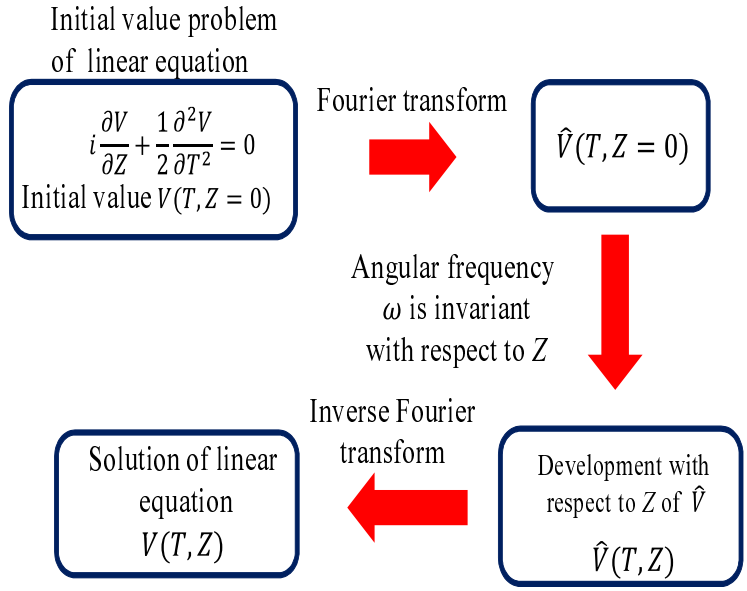

Fig. B.1: Process of solving an initial value problem using Fourier transform.

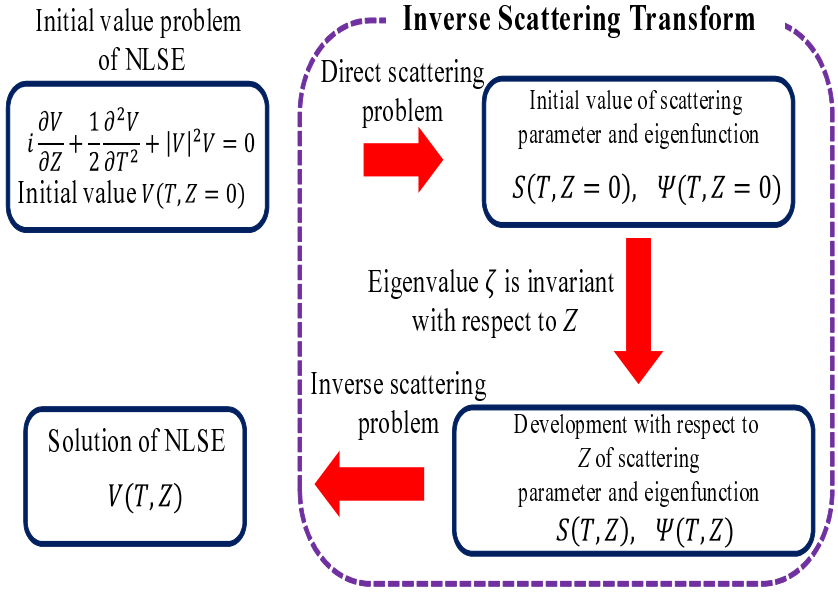

Fig. B.2: Process of solving an initial value problem using IST.

B.3 Inverse Scattering Transform

It is noteworthy that IST can solve an initial value problem for certain classes of nonlinear partial differential equations. It can be viewed as a nonlinear analogue of the Fourier transform. In this section, IST is explained with comparison to the Fourier transform. Here, the following linear evolution equation is discussed:

$$i\frac{\partial V}{\partial Z}=A\left(i\frac{\partial}{\partial T}\right)V=\sum_{n=0}^{\infty}p_n\left(i\frac{\partial}{\partial T}\right)^n V \qquad p_n : \text{is an arbitrary constant .} \tag{B.20}$$

Generally, the Fourier transformation of an initial value $V(T,0)$ is expressed as

$$\tilde{V}(\omega,0)=\frac{1}{\sqrt{2\pi}}\int_{-\infty}^{\infty}V(T,0)e^{-i\omega T}dT\ . \tag{B.21}$$

By performing Fourier transformation onto Eq. (B.20), we have

$$\frac{\partial\tilde{V}}{\partial Z}=-iA(\omega)\tilde{V}\ . \tag{B.22}$$

This equation is solvable, the solution of which is

$$\tilde{V}(\omega,Z)=\tilde{V}(\omega,0)\mathrm{exp}[-iA(\omega)Z]\ , \tag{B.23}$$

describing the development of $\tilde{V}$ along the propagation distance Z. Finally, by calculating the inverse Fourier transform of $\tilde{V}(\omega,Z)$, $V(T,Z)$ is obtainable as

$$\mathrm{V}(T,Z)=\frac{1}{\sqrt{2\pi}}\int_{-\infty}^{\infty}\tilde{V}(\omega,Z)e^{i\omega T}d\omega=\frac{1}{\sqrt{2\pi}}\int_{-\infty}^{\infty}\tilde{V}(\omega,0)e^{i\{\omega T-A(\omega)Z\}}d\omega\ . \tag{B.24}$$

This procedure is presented in Fig. B.1. In contrast, scattering parameter $S(\zeta,Z=0)$ is obtained by solving the direct scattering problem of the eigenvalue equation for a given initial value $V(T,Z=0)$ in IST. Then, the evolution equation of the eigenfunction along Z is used to ascertain the scattering parameter $S(\zeta,Z)$ with respect to Z. Inverse scattering techniques are then applied to obtain the solution $V(T,Z)$ of the original equation. This procedure is presented in Fig. B.2. In the following, the direct scattering problem, the development of the scattering parameter during the propagation, and the inverse scattering problem are presented under separate subsections.

B.3.1 Direct Scattering Problem

Examining the amount of reflection (reflection rate) and penetration (transmission rate) of an incident wave for a given potential is the crux of the direct scattering problem. Solving the scattering problem given in Eq. (B.17) is referred from the direct scattering problem when the initial value $V(T,Z=0)$ for a given potential. The reflected wave for $T\to\infty$ and the transmitted wave for $T\to-\infty$ is determined for the incident wave coming from $T=\infty$. Actually, Eq. (B.17) satisfies the boundary condition $V=0$ for $T\to\infty$. Here, the eigenfunction $\mathbf{\Psi}$ represents the incident wave, the reflected wave, and the transmitted wave. For an assigned $V(T,Z=0)$, the reflection rate and the transmission rate are obtainable by determining the eigenfunction $\mathbf{\Psi}$. For $T\to\infty$, V becomes 0, then Eq. (B.17) can be rewritten as

$$\begin{cases}\dfrac{\partial\Psi_1}{\partial T}=-i\zeta\Psi_1\ ,\\[2ex] \dfrac{\partial\Psi_2}{\partial T}=i\zeta\Psi_2\ .\end{cases} \tag{B.25}$$

First, one can consider a case in which eigenvalue ζ can be represented by a real number ξ. The solution of Eq. (B.25) can be expressed as

$$\begin{cases}\Psi_1(T)=\Psi_{10}\exp\left(-i\xi T\right)\ ,\\[2ex] \Psi_2(T)=\Psi_{20}\exp\left(i\xi T\right)\ ,\end{cases} \tag{B.26}$$

where Ψ_{10} and Ψ_{20} represent integral constants.

From these equations, the solutions of Eq. (B.17), which satisfy the boundary conditions $T \to \infty$, can be represented in terms of $\boldsymbol{\phi}$, $\overline{\boldsymbol{\phi}}$, $\boldsymbol{\chi}$, and $\overline{\boldsymbol{\chi}}$ as:

$$\begin{cases} \boldsymbol{\phi}(\xi,T) = \begin{pmatrix} \phi_1(\xi,T) \\ \phi_2(\xi,T) \end{pmatrix} = \begin{pmatrix} 1 \\ 0 \end{pmatrix} \exp\left(-i\xi T\right) & (T \to -\infty)\ , \\ \overline{\boldsymbol{\phi}}(\xi,T) = \begin{pmatrix} \phi_2^*(\xi,T) \\ -\phi_1^*(\xi,T) \end{pmatrix} = \begin{pmatrix} 0 \\ -1 \end{pmatrix} \exp\left(i\xi T\right) & (T \to -\infty)\ , \end{cases} \tag{B.27}$$

$$\begin{cases} \boldsymbol{\chi}(\xi,T) = \begin{pmatrix} \chi_1(\xi,T) \\ \chi_2(\xi,T) \end{pmatrix} = \begin{pmatrix} 0 \\ 1 \end{pmatrix} \exp\left(i\xi T\right) & (T \to \infty)\ , \\ \overline{\boldsymbol{\chi}}(\xi,T) = \begin{pmatrix} \chi_2^*(\xi,T) \\ -\chi_1^*(\xi,T) \end{pmatrix} = \begin{pmatrix} 1 \\ 0 \end{pmatrix} \exp\left(-i\xi T\right) & (T \to \infty)\ , \end{cases} \tag{B.28}$$

where $\boldsymbol{\phi}$, $\overline{\boldsymbol{\phi}}$, $\boldsymbol{\chi}$, and $\overline{\boldsymbol{\chi}}$ are called the Jost functions. $\boldsymbol{\phi}$, $\overline{\boldsymbol{\phi}}$, $\boldsymbol{\chi}$, and $\overline{\boldsymbol{\chi}}$ are linearly independent. It is noteworthy that $\boldsymbol{\phi}$ and $\overline{\boldsymbol{\phi}}$ can be expressed when one set of the above equations is chosen as the base of the solutions of Eq. (B.17). Using appropriate coefficients $a(\xi)$ and $b(\xi)$ as, $\boldsymbol{\phi}$ and $\overline{\boldsymbol{\phi}}$ can be expressed by using $\boldsymbol{\chi}$ and $\overline{\boldsymbol{\chi}}$ as

$$\begin{cases} \boldsymbol{\phi}(\xi,T) = a(\xi)\overline{\boldsymbol{\chi}}(\xi,T) + b(\xi)\boldsymbol{\chi}(\xi,T)\ , \\ \overline{\boldsymbol{\phi}}(\xi,T) = -a^*(\xi)\boldsymbol{\chi}(\xi,T) + b^*(\xi)\overline{\boldsymbol{\chi}}(\xi,T)\ . \end{cases} \tag{B.29}$$

Here, a and b satisfy $|a(\xi)|^2 + |b(\xi)|^2 = 1$. Then, $\boldsymbol{\chi}$ and $\overline{\boldsymbol{\chi}}$ can be represented as

$$\begin{cases} \boldsymbol{\chi}(\xi,T) = -a(\xi)\overline{\boldsymbol{\phi}}(\xi,T) + b^*(\xi)\boldsymbol{\phi}(\xi,T)\ , \\ \overline{\boldsymbol{\chi}}(\xi,T) = a^*(\xi)\boldsymbol{\phi}(\xi,T) + b(\xi)\overline{\boldsymbol{\phi}}(\xi,T)\ . \end{cases} \tag{B.30}$$

The above are the solutions for an incident wave arriving from $T = \pm\infty$ and scattered by the potential $V(Z=0,T)$. In the following, we consider a case in which an incident wave comes from $T = \infty$. The first equation of Eq. (B.29) represents a solution of Eq. (B.17) when Eq. (B.29) satisfies the following boundary conditions:

$$\begin{cases} \boldsymbol{\phi}(\xi,T) = \begin{pmatrix} \phi_1(\xi,T) \\ \phi_2(\xi,T) \end{pmatrix} = \begin{pmatrix} \exp\left(-i\xi T\right) \\ 0 \end{pmatrix} & (T \to -\infty)\ , \\ \boldsymbol{\phi}(\xi,T) = \begin{pmatrix} \phi_1(\xi,T) \\ \phi_2(\xi,T) \end{pmatrix} = \begin{pmatrix} a(\xi)\exp\left(-i\xi T\right) \\ b(\xi)\exp\left(i\xi T\right) \end{pmatrix} & (T \to \infty)\ . \end{cases} \tag{B.31}$$

Here, scattering caused by the potential V is shown in Fig. B.3. Incident wave comes from $T \to \infty$ and scatter due to the potential V. Transmitted wave propagates to $T \to -\infty$, while reflected

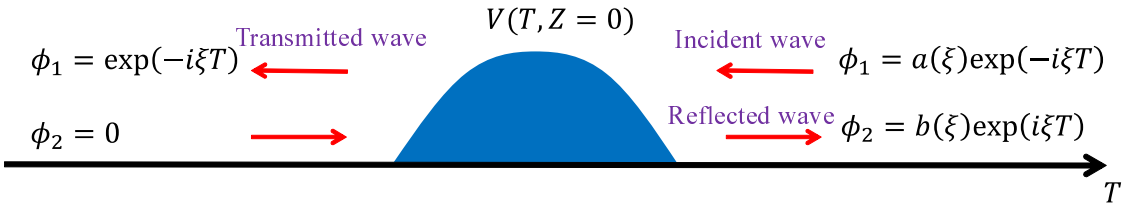

Fig. B.3: Scattering caused by potential $V(T, Z=0)$.

wave reflects to $T \to \infty$. No electric field comes from$T \to -\infty$. $a(\xi)\exp(-i\xi T)$ and $b(\xi)\exp(i\xi T)$ in Eq. (B.31), respectively represent the incident wave and reflected wave at $T \to \infty$ as shown in Fig. B.3.

Next, real eigenvalue ξ is replaced with complex eigenvalue $\zeta = \xi + i\alpha$ (α: real number). In Eqs. (B.27) and (B.28), even if ξ is replaced by $\xi + i\alpha$, $\boldsymbol{\phi}(\xi, T)$ and $\boldsymbol{\chi}(\xi, T)$ are not divergent for $\alpha > 0$, and then analytic continuation is made in the complex upper half-plane. Moreover, when $\overline{\boldsymbol{\phi}}(\xi, T)$ and $\overline{\boldsymbol{\chi}}(\xi, T)$ are not divergent for $\alpha < 0$, then analytic continuation is possible in the complex lower half-plane. When ξ is replaced with $\xi + i\alpha$ in the second equation of Eq. (B.31) in the complex upper half-plane, we obtain

$$\boldsymbol{\phi}(\zeta, T) = \begin{pmatrix} a(\zeta)\exp(-i\zeta T + \alpha T) \\ b(\zeta)\exp(i\zeta T - \alpha T) \end{pmatrix} . \tag{B.32}$$

For $a(\zeta) \neq 0$, $\boldsymbol{\phi} \to \infty$ with $T \to \infty$, which seems strange result as a boundary condition. Therefore, $a(\zeta)$ should be 0 for this case.

The complex eigenvalues of Eq. (B.17) become discrete when $a(\zeta) = 0$. Then, we write eigenvalue ζ as ζ_n $(n = 1, 2..., N)$. Setting $\boldsymbol{\phi}_n(T) \equiv \boldsymbol{\phi}(\zeta_n, T)$, $\overline{\boldsymbol{\phi}}_n(T) \equiv \overline{\boldsymbol{\phi}}(\zeta_n, T)$, $\boldsymbol{\chi}_n(T) \equiv \boldsymbol{\chi}(\zeta_n, T)$, and $\overline{\boldsymbol{\chi}}_n(T) \equiv \overline{\boldsymbol{\chi}}(\zeta_n, T)$, we rewrite Eq. (B.29) and Eq. (B.30) as

$$\begin{cases} \boldsymbol{\phi}_n(T) = b(\zeta_n)\boldsymbol{\chi}_n(T) , \\ \overline{\boldsymbol{\phi}}_n(T) = b^*(\zeta_n^*)\overline{\boldsymbol{\chi}}_n(T) , \\ \boldsymbol{\chi}_n(T) = b^*(\zeta_n^*)\boldsymbol{\phi}_n(T) , \\ \overline{\boldsymbol{\chi}}_n(T) = b(\zeta_n)\overline{\boldsymbol{\phi}}_n(T) . \end{cases} \tag{B.33}$$

In summary, $a(\zeta)$, $b(\zeta)$ and $r(\xi)$, $\gamma(\zeta_n)$ in a direct scattering problem can be determined for a direct scattering problem for the initial value $V(T, Z=0)$. Scattering parameter $r(\xi)$ and $\gamma(\zeta_n)$ are calculable by the following equations consisting of $a(\zeta)$ and $b(\zeta)$:

$$\begin{cases} r(\xi, Z=0) = \dfrac{b(\xi, Z=0)}{a(\xi, Z=0)} , \\ \gamma_n(Z=0) = \gamma(\zeta_n, Z=0) = \dfrac{b(\zeta_n, Z=0)}{a'(\zeta_n, Z=0)} , \end{cases} \tag{B.34}$$

where

$$a'(\zeta_n, Z=0) = \left.\frac{\partial a(\zeta, Z=0)}{\partial \zeta}\right|_{\zeta=\zeta_n} . \tag{B.35}$$

B.3.2 Development with Respect to Distance of the Scattering Parameter

This subsection describes the behavior of the scattering parameter along the propagation distance. The evolution equations of the eigenfunction $\boldsymbol{\Psi}$ with respect to Z, given by Eq. (B.18), are used to determine the scattering parameter's spatial variation. First, based on the boundary condition of $V = 0$ for $|T| \to \infty$, we rewrite Eq. (B.18) as

$$\begin{cases} \dfrac{\partial \Psi_1}{\partial Z} = -i\zeta^2 \Psi_1 \ , \\ \dfrac{\partial \Psi_2}{\partial Z} = i\zeta^2 \Psi_2 \ . \end{cases} \tag{B.36}$$

Next, the dependency of the eigenfunction on Z is expressed in a form of the Jost functions as

$$\begin{cases} \boldsymbol{\phi}^{(Z)}(\zeta, T, Z) = \boldsymbol{\phi}(\zeta, T) \exp\left(-i\zeta^2 Z\right) \ , \\ \overline{\boldsymbol{\phi}}^{(Z)}(\zeta, T, Z) = \overline{\boldsymbol{\phi}}(\zeta, T) \exp\left(i\zeta^2 Z\right) \ , \\ \boldsymbol{\chi}^{(Z)}(\zeta, T, Z) = \boldsymbol{\chi}(\zeta, T) \exp\left(i\zeta^2 Z\right) \ , \\ \overline{\boldsymbol{\chi}}^{(Z)}(\zeta, T, Z) = \overline{\boldsymbol{\chi}}(\zeta, T) \exp\left(-i\zeta^2 Z\right) \ , \end{cases} \tag{B.37}$$

where $\boldsymbol{\phi}^{(Z)}$ satisfies Eq. (B.18) as

$$\begin{cases} \dfrac{\partial \phi_1^{(Z)}}{\partial Z} = \left(\dfrac{\partial \phi_1}{\partial Z} - i\zeta^2 \phi_1 \right) \exp\left(-i\zeta^2 Z\right) = \left\{ i \left(\dfrac{|V|^2}{2} - \zeta^2 \right) \phi_1 + \left(i\zeta V - \dfrac{1}{2} \dfrac{\partial V}{\partial T} \right) \phi_2 \right\} \exp\left(-i\zeta^2 Z\right) \ , \\ \dfrac{\partial \phi_2^{(Z)}}{\partial Z} = \left(\dfrac{\partial \phi_2}{\partial Z} - i\zeta^2 \phi_2 \right) \exp\left(-i\zeta^2 Z\right) = \left\{ \left(i\zeta V^* - \dfrac{1}{2} \dfrac{\partial V^*}{\partial T} \right) \phi_1 - i \left(\dfrac{|V|^2}{2} - \zeta^2 \right) \phi_2 \right\} \exp\left(-i\zeta^2 Z\right) \ . \end{cases} \tag{B.38}$$

The above equation is summarized in a matrix form as

$$\frac{\partial \boldsymbol{\phi}}{\partial Z} = \begin{pmatrix} i\dfrac{|V|^2}{2} & i\zeta V - \dfrac{1}{2} \dfrac{\partial V}{\partial T} \\ i\zeta V^* - \dfrac{1}{2} \dfrac{\partial V^*}{\partial T} & i \left(2\zeta^2 - \dfrac{|V|^2}{2} \right) \end{pmatrix} \boldsymbol{\phi} \ . \tag{B.39}$$

Partial derivative with respect to Z of the second equation in Eq. (B.31) and Eq. (B.39) is regarded as equal for $T \to \infty$. Using Eq. (B.36),

$$\begin{pmatrix} \dfrac{\partial a}{\partial Z} \exp\left(-i\zeta T\right) \\ \dfrac{\partial b}{\partial Z} \exp\left(i\zeta T\right) \end{pmatrix} = \begin{pmatrix} 0 \\ 2i\zeta^2 b \exp\left(i\zeta T\right) \end{pmatrix} \tag{B.40}$$

can be obtained. By solving Eq. (B.40), a and b can be represented as

$$\begin{cases} a(\zeta, Z) = a(\zeta, Z = 0) \ , \\ b(\zeta, Z) = b(\zeta, Z = 0) \exp\left(2i\zeta^2 Z\right) \ . \end{cases} \tag{B.41}$$

Substituting Eq. (B.41) into Eq. (B.34), the scattering parameters can be expressed as

$$\begin{cases} r(\xi, Z) = \dfrac{b(\xi, Z)}{a(\xi, Z)} = \dfrac{b(\xi, Z = 0)}{a(\xi, Z = 0)} \exp\left(2i\xi^2 Z\right) = r(\xi, Z = 0) \exp\left(2i\xi^2 Z\right) \ , \\ \gamma_n(Z) = \dfrac{b(\zeta_n, Z)}{a'(\zeta_n, Z)} = \dfrac{b(\zeta_n, Z = 0)}{a'(\zeta_n, Z = 0)} \exp\left(2i\zeta^2 Z\right) = \gamma_n(Z = 0) \exp\left(2i\zeta^2 Z\right) \ . \end{cases} \tag{B.42}$$

B.3.3 Inverse Scattering Problem

Determining the solution $V(T,Z)$ from the scattering parameters which were obtained in the previous subsection is referred as inverse scattering problem. The linear integral equation is derived first to find eigenfunctions from the scattering parameters as follows.

When both sides of the first equation of Eq. (B.29) are divided by $a\left(\xi\right)\left(\xi-\zeta\right)$ and then are inversely Fourier transformed, the following equation is obtained.

$$\int_{-\infty}^{\infty}\frac{1}{a(\xi)}\frac{\boldsymbol{\phi}(\xi,T)}{(\xi-\zeta)}\exp\left(i\xi T\right)d\xi=\int_{-\infty}^{\infty}\frac{\overline{\boldsymbol{\chi}}(\xi,T)}{\xi-\zeta}\exp\left(i\xi T\right)d\xi+\int_{-\infty}^{\infty}r(\xi)\frac{\boldsymbol{\chi}(\xi,T)}{\xi-\zeta}\exp\left(i\xi T\right)d\xi\ . \tag{B.43}$$

Then, $a(\zeta')=0$ when $\zeta'=\zeta_n$. Performing complex integration onto the left hand side yields the following equation:

$$\int_{-\infty}^{\infty}\frac{1}{a(\xi)}\frac{\boldsymbol{\phi}(\xi,T)}{(\xi-\zeta)}\exp\left(i\xi T\right)d\xi=i2\pi\sum_{n=1}^{N}\gamma_n\frac{\boldsymbol{\chi}_n(T)}{\zeta_n-\zeta}\exp\left(i\zeta_n T\right)-i\pi\begin{pmatrix}1\\0\end{pmatrix}\ . \tag{B.44}$$

On the other hand, the integration of the first term on the right hand side becomes

$$\int_{-\infty}^{\infty}\frac{\overline{\boldsymbol{\chi}}(\xi,T)}{\xi-\zeta}\exp\left(i\xi T\right)d\xi=-i2\pi\overline{\boldsymbol{\chi}}(\zeta,T)\exp\left(i\zeta T\right)+i\pi\begin{pmatrix}1\\0\end{pmatrix}\ . \tag{B.45}$$

By substituting Eq. (B.44) and Eq. (B.45) into Eq. (B.43),

$$\overline{\boldsymbol{\chi}}(\zeta,T)\exp\left(i\zeta T\right)=\begin{pmatrix}1\\0\end{pmatrix}-\frac{i}{2\pi}\int_{-\infty}^{\infty}r(\xi)\frac{\boldsymbol{\chi}(\xi,T)}{\xi-\zeta}\exp\left(i\xi T\right)d\xi-\sum_{n=1}^{N}\gamma_n\frac{\boldsymbol{\chi}_n(T)}{\zeta_n-\zeta}\exp\left(i\zeta_n T\right) \tag{B.46}$$

can be obtained. Then, the following integral equation is obtainable from Eq. (B.46):

$$\begin{cases}\chi_1(\zeta,T,Z)\exp\left(-i\zeta T\right)=-\dfrac{i}{2\pi}\displaystyle\int_{-\infty}^{\infty}\frac{r^*(\xi,Z)\chi_2^*(\xi,T,Z)}{\xi-\zeta}\exp\left(-i\xi T\right)d\xi\\ \qquad\qquad\qquad\qquad+\displaystyle\sum_{n=1}^{N}\frac{\gamma_n^*(Z)\chi_{n2}^*(T,Z)}{\zeta_n^*-\zeta}\exp\left(-i\zeta_n^* T\right)\ ,\\ \chi_2(\zeta,T,Z)\exp\left(-i\zeta T\right)=1+\dfrac{i}{2\pi}\displaystyle\int_{-\infty}^{\infty}\frac{r^*(\xi,Z)\chi_1^*(\xi,T,Z)}{\xi-\zeta}\exp\left(-i\xi T\right)d\xi\\ \qquad\qquad\qquad\qquad-\displaystyle\sum_{n=1}^{N}\frac{\gamma_n^*(Z)\chi_{n1}^*(T,Z)}{\zeta_n^*-\zeta}\exp\left(-i\zeta_n^* T\right)\ .\end{cases} \tag{B.47}$$

The above equations show that eigenfunctions χ_1 and χ_2 can be calculated for a given discrete eigenvalue ζ_n and scattering parameters $r(\xi,Z)$ and $\gamma_n(Z)$.

Here, eigenfunction $(\chi_1,\chi_2)^{\mathrm{T}}$ is assumed to be expressed as

$$\begin{cases}\chi_1=f_1\exp\left(i\zeta T\right)\ ,\\ \chi_2=f_2\exp\left(i\zeta T\right)\ .\end{cases} \tag{B.48}$$

According to Eq. (B.17),

$$\begin{cases}\left(\dfrac{\partial f_1}{\partial T}+i\zeta f_1\right)\exp\left(i\zeta T\right)=\left(-i\zeta f_1+iVf_2\right)\exp\left(i\zeta T\right)\ ,\\ \left(\dfrac{\partial f_2}{\partial T}+i\zeta f_2\right)\exp\left(i\zeta T\right)=\left(iV^*f_1+i\zeta f_2\right)\exp\left(i\zeta T\right)\end{cases} \tag{B.49}$$

can be obtained. By arranging these equations in proper order,

$$\begin{cases} \dfrac{\partial f_1}{\partial T} = -i2\zeta f_1 + iV f_2 \ , \\ \dfrac{\partial f_2}{\partial T} = iV^* f_1 \end{cases} \tag{B.50}$$

can be derived. For $T \to \infty$, $(\chi_1, \chi_2)^{\mathrm{T}} \to (0, \exp(i\zeta T))^{\mathrm{T}}$ as given in Eq. (B.28). Therefore, $(f_1, f_2)^{\mathrm{T}}$ tends to $(0,1)^{\mathrm{T}}$ in Eq. (B.48). When f_1 and f_2 are expanded by ζ for $|\zeta| \gg 1$, f_1 and f_2 respectively becomes

$$\begin{cases} f_1 = \dfrac{f_1^{(1)}}{\zeta} + \dfrac{f_1^{(2)}}{\zeta^2} + \cdots , \\ f_2 = 1 + \dfrac{f_2^{(1)}}{\zeta} + \dfrac{f_2^{(2)}}{\zeta^2} + \cdots . \end{cases} \tag{B.51}$$

Substitute Eq. (B.51) into Eq. (B.50),

$$\begin{cases} f_1^{(1)} = \dfrac{V}{2} \ , \\ f_2^{(1)} = -\dfrac{i}{2}\displaystyle\int_T^\infty |V(T', Z)|^2 dT' \end{cases} \tag{B.52}$$

can be obtained. Using Eq. (B.48) and Eq. (B.51),

$$\boldsymbol{\chi} \exp(-i\zeta T) = \begin{pmatrix} \chi_1 \\ \chi_2 \end{pmatrix} \exp(-i\zeta T) = \begin{pmatrix} f_1 \\ f_2 \end{pmatrix} = \begin{pmatrix} 0 \\ 1 \end{pmatrix} - \frac{i}{2\zeta} \begin{pmatrix} iV(T,Z) \\ \displaystyle\int_T^\infty |V(T', Z)|^2 dT' \end{pmatrix} + \cdots . \tag{B.53}$$

Substituting Eq. (B.47) into Eq. (B.53), we have

$$\begin{cases} V(T,Z) = \dfrac{i}{\pi}\displaystyle\int_{-\infty}^\infty r^*(\xi, Z)\chi_2^*(\xi, T, Z)\exp(-i\xi T)d\xi - 2\sum_{n=1}^N \gamma_n^*(Z)\chi_{n2}^*(T,Z)\exp(-i\zeta_n^* T) \ , \\ \displaystyle\int_T^\infty |V(T', Z)|^2 dT' = \frac{1}{\pi}\int_{-\infty}^\infty r(\xi, Z)\chi_1(\xi, T, Z)\exp(i\xi T)d\xi \\ \qquad\qquad -i2\displaystyle\sum_{n=1}^N \gamma_n(Z)\chi_{n1}(T,Z)\exp(-i\zeta_n T) \ . \end{cases} \tag{B.54}$$

From the first equation of Eq. (B.54), potential $V(T,Z)$ can be ascertained using scattering parameters $r(\xi, Z)$, $\gamma_n(Z)$ and eigenfunctions $\chi_2(\xi, T, Z)$, $\chi_{n2}(T,Z)$.

Bibliography

[1] Paul. C. Lin, "A chronology of freaque wave encounters," *Geozika*, vol. 24, no. 1, pp. 57–70, 2007.

[2] C. Kharif and E. Pelinovsky, "Physical mechanisms of the rogue wave phenomenon," *Eur. J. Mech. B/Fluids*, vol. 22, pp. 603–634, 2003.

[3] K. Dysthe, H. E. Krogstad, and P. Müller, "Oceanic Rogue Waves," *Annu. Rev. Fluid Mech.*, vol. 40, pp. 287–310, 2008.

[4] The New York Times, http://www.nytimes.com/

[5] I. Nikolkina and I. Didenkulova, "Rogue waves in 2006-2010," *Nat. Hazards Earth Syst. Sci.*, vol. 11, pp. 2913–2924, 2011.

[6] Japan Meteorological Agency, http://www.jma.go.jp/jma/indexe.html

[7] T. B. Benjamin and J. E. Feir, "The disintegration of wave trains on deep water. Part 1. Theory," *J. Fluid Mech.*, vol. 27, no. 3, pp. 417–430, 1967.

[8] V. E. Zakharov, "Stability of periodic waves of finite amplitude on the surface of a deep fluid," *J. Appl. Mech. Tech. Phys.*, vol. 9, no. 2, pp. 190–194, 1968.

[9] D. R. Solli, C. Ropers, P. Koonath, and B. Jalali, "Optical rogue waves," *Nature*, vol. 450, pp. 1054–1057, 2007.

[10] G. Genty, C. M. de Sterke, O. Bang, F. Dias, N. Akhmediev, and J. M. Dudley, "Collisions and turbulence in optical rogue wave formation," *Phy. Lett. A*, vol. 374, no. 7, pp. 989–996, 2010.

[11] M. Erkintalo, G. Genty, and J. M. Dudley, "Giant dispersive wave generation through soliton collision," *Opt. Lett.*, vol. 35, no. 5, pp. 658–660, 2010.

[12] R. Driben and I. Babushkin, "Accelerated rogue waves generated by soliton fusion at the advanced stage of supercontinuum formation in photonic-crystal fibers," *Opt. Lett.*, vol. 37, no. 24, pp. 5157–5159, 2012.

[13] M. Onorato, S. Residori, U. Bortolozzo, A. Montina, and F. T. Arecchi, "Rogue waves and their generating mechanisms in different physical contexts," *Phys. Rep.*, vol. 528, no. 2, pp. 47–89, 2013.

[14] B. Kibler, K. Hammani, C. Michel, C. Finot, and A. Picozzi, "Rogue waves, rational solitons and wave turbulence theory," *Phy. Lett. A*, vol. 375, no. 35, pp. 3149–3155, 2011.

[15] K. Hammani, B. Kibler, C. Finot, and A. Picozzi, "Emergence of rogue waves from optical turbulence," *Phy. Lett. A*, vol. 374, no. 34, pp. 3585–3589, 2010.

[16] N. Akhmediev, J. M. Dudley, D. R. Solli, and S. K. Turitsyn, "Recent progress in investigating optical rogue waves," *J. Opt.*, vol. 15, no. 6, 06020, 2013.

[17] V. E. Zakharov, V. S. L'vov, and G. Falkovich, *Kolmogorov Spectra of Turbulence*, Springer-Verlag, 1992.

[18] D. H. Peregrine, "Water waves, nonlinear Schrödinger equations and their solutions," *J. Aust. Math. Soc. Ser. B. Appl. Math.*, vol. 25, pp. 16–43, 1983.

[19] E. A. Kuznetsov, "Solitons in a parametrically unstable plasma," *Dokl. Akad. Nauk SSSR*, vol. 236, pp. 575–577, 1977.

[20] Y. C. Ma, "The perturbed plane-wave solutions of the cubic Schrödinger equation," *Stud. Appl. Math.*, vol. 60, pp. 43–58, 1979.

[21] C. Q. Dai and Y. Y. Wang, "Controllable combined Peregrine soliton and Kuznetsov-Ma soliton in PT-symmetric nonlinear couplers with gain and loss," *Nonlinear Dyn.*, vol. 80, pp. 715–721, 2015.

[22] J. Li, J. Han, Y. Du, and C. Q. Dai, "Controllable behaviors of Peregrine soliton with two peaks in a birefringent fiber with higher-order effects," *Nonlinear Dyn.*, vol. 82, pp. 1393–1398, 2015.

[23] J. M. Soto-Crespo, M. Grapinet, P. Grelu, and N. Akhmediev, "Bifurcations and multiple-period soliton pulsations in a passively mode-locked fiber laser," *Phys. Rev. E*, vol. 70, pp. 066612, 2014.

[24] G. P. Agrawal, *Nonlinear Fiber Optics* (Fifth ed.), Academic Press, 2013.

[25] D. R. Solli, G. Herink, B. Jalali, and C. Ropers, "Fluctuations and correlations in modulation instability," *Nature Photon.*, vol. 6, pp. 463–468, 2012.

[26] D. R. Solli, C. Ropers, and B. Jalali, "Measuring single-shot modulation instability and supercontinuum spectra at megahertz rates," *Nonlinearity*, vol. 26, no. 3, pp. R85–R92, 2013.

[27] A. Mussot, A. Kudlinski, M. Kolobov, E. Louvergneaux, M. Douay, and M. Taki, "Observation of extreme temporal events in CW-pumped supercontinuum," *Opt. Express*, vol. 17, no. 63, pp. 17010–17015, 2009.

[28] J. M. Dudley, G. Genty, F. Dias, B. Kibler, and N. Akhmediev, "Modulation instability, Akhmediev Breathers and continuous wave supercontinuum generation," *Opt. Express*, vol. 17, no. 94, pp. 21497–21508, 2009.

[29] J. Dudley, G. Genty, and S. Coen, "Supercontinuum generation in photonic crystal fiber," *Rev. Mod. Phys.*, vol. 78, no. 4, pp. 1135–1184, 2006.

[30] S. V. Smirnov, J. D. Ania-Castanon, T. J. Ellingham, S. M. Kobtsev, S. Kukarin, and S. K. Turitsyn, "Optical spectral broadening and supercontinuum generation in telecom applications," *Opt. Fiber Technol.*, vol. 12, no. 2, pp. 122–147, 2006.

[31] N. Akhmediev, Eds., "Roadmap on optical rogue waves and extreme events," *Journal of Optics*, vol. 18, no. 6, 063001, 2016.

[32] M. Horowitz, Y. Barad, and Y. Silberberg, "Noiselike pulses with a broadband spectrum generated from an erbium-doped fiber laser," *Opt. Lett.*, vol. 22, no. 11, pp. 799-801, 1997.

[33] L. M. Zhao, D. Y. Tang, T. H. Cheng, H. Y. Tam, and C. Lu, "120 nm bandwidth noise-like pulse generation in an erbium-doped fiber laser," *Opt. Commun.*, vol. 281, pp. 157–161, 2008.

[34] O. Pottiez, R. Grajales-Coutiño, B. Ibarra-Escamilla, E. A. Kuzin, and J. C. Hernández-García, "Adjustable noiselike pulses from a figure-eight fiber laser," *Appl. Opt.*, vol. 50, pp. E24–E31, 2011.

[35] A. Boucon, B. Barivau, J. Fatome, C. Finot, T. Sylvestre, M. W. Lee, P. Grelu, and G. Millot, "Noise-like pulses generated at high harmonics in a partially-mode-locked km-long Raman fiber laser," *Appl. Phys. B*, vol. 106, pp. 283–287, 2012.

[36] C. Lecaplain, Ph. Grelu, J. M. Soto-Crespo, and N. Akhmediev, "Dissipative Rogue Waves Generated by Chaotic Pulse Bunching in a Mode-Locked Laser," *Phy. Rev. Lett.*, vol. 108, 233901, 2012.

[37] J. M. Dudly, G. Genty, and S. Coen, "Supercontinuum generation in photonic crystal fiber," *Rev. Mod. Phys.*, vol. 78, pp. 1135–1184, 2006.

[38] R. R. Alfano, "The ultimate white light," *Sci. Am.*, vol. 295, pp. 87–93, 2006.

[39] Y. Han, O. Boyraz, and B. Jalali, "Tera-sample per second real-time waveform digitizer," *Appl. Phys. Lett.*, vol. 87, 241116, 2005.

[40] Y. Shuto, S. Yanagi, S. Asakawa, M. Kobayashi, and R. Nagase, "Simulation of Fiber Fuse Phenomenon in Single-Mode Optical Fibers," *IEEE/OSA J. Lightwave Technol.*, vol. 21, no. 11, pp. 2511–2517, 2003.

[41] J. Wang, S. Gray, D. Walton, and L. Zenteno, "Fiber fuse in high power optical fiber," *Proc. SPIE 7134, Passive Components and Fiber-based Devices V*, 71342E, 2008.

[42] R. Kashyap and K. J. Blow, "Self-propelled self-focusing damage in optical fibers," *Electron. Lett.*, vol. 24, no. 1, pp. 47–49, 1988.

[43] D. P. Hand and P. S. J. Russell, "Solitary thermal shock waves and optical damage in optical fibers: the fiber fuse," *Opt. Lett.*, vol. 13, no. 9, pp. 767–769, 1988.

[44] N. Akhmediev, A. Ankiewicz, and M. Taki, "Waves that appear from nowhere and disappear without a trace," *Phy. Lett. A*, vol. 373, no. 6, pp. 675–678, 2009.

[45] F. Baronio, M. Conforti, A. Degasperis, S. Lombardo, M. Onorato, and S. Wabnitz, "Vector rogue waves and baseband modulation instability in the defocusing regime," *Phys. Rev. Lett.*, vol. 113, 034101, 2014.

[46] A. Ankiewicz, J. M. Soto-Crespo, and N. Akhmediev, "Rogue waves and rational solutions of the Hirota equation," *Phys. Rev. E*, vol. 81, 046602, 2010.

[47] J. M. Soto-Crespo, P. Grelu, and N. Akhmediev, "Dissipative rogue waves: Extreme pulses generated by passively mode-locked lasers," *Phys. Rev. E*, vol. 84, 016604, 2011.

[48] S. Chen, J. M. Soto-Crespo, and P. Grelu, "Dark three-sister rogue waves in normally dispersive optical fibers with random birefringence," *Opt. Express*, vol. 22, no. 22, pp. 27632–27642, 2014.

[49] H. P. Zhu and Y. J. Chen, "Spatiotemporal superposed rogue-wave-like breathers in a (3+1)-dimensional variable-coefficient nonlinear Schrödinger equation," *Nonlinear Analysis: Modeling and Control*, vol. 21, no. 1, pp. 77–91, 2015.

[50] M. Taki, A. Mussot, A. Kudlinski, E. Louvergneaux, M. Kolobov, and M. Douay, "Third-order dispersion for generating optical rogue solitons," *Phys. Lett. A*, vol. 374, pp. 691–695, 2010.

[51] A. Ankiewicz, J. M. Soto-Crespo, M. A. Chowdhury, and N. Akhmediev, "Rogue waves in optical fibers in presence of third-order dispersion, self-steepening, and self-frequency shift," *J. Opt. Soc. Am. B*, vol. 30, no. 1, pp. 87–94, 2013.

[52] Y. Chen and Z. Yan, "Solitonic dynamics and excitations of the nonlinear Schrödinger equation with third-order dispersion in non-Hermitian PT-symmetric potentials," *Scientific Reports*, vol. 6, 23478, 2016.

[53] G. Weerasekara, A. Tokunaga, H. Terauchi, M. Eberhard, and A. Maruta, "Soliton's eigenvalue based analysis on the generation mechanism of rogue wave phenomenon in optical fibers exhibiting weak third order dispersion," *Opt. Express*, vol. 23, no. 1, pp. 143–153, 2015.

[54] N. Akhmediev and E. Pelinovsky, "Editorial-Introductory remarks on Discussion and Debate : Rogue Waves-Towards a Unifying Concept?," *Eur. Phys. J. Spec. Top.*, vol. 185, pp. 1–4, 2010.

[55] R. Driben and N. Zhavoronkov, "Effective Soliton Fusion Process at the Advanced Stage of Supercontinuum Generation in Photonic Crystal Fibers," *Optics and Photonics Journal*, vol. 2, pp. 211–215, 2012.

[56] S. Wang, X. Tang, and S. Lou, "Soliton fission and fusion: Burgers equation and Sharma-Tasso-Olver equation," *Chaos, Solitons, and Fractals*, vol. 21, pp. 231–239, 2004.

[57] Y. Jin-Ping, "Fission and Fusion of Solitons for the (1+1)-Dimensional Kupershmidt Equation," *Commun. Theor. Phys.*, vol. 35, no. 4, pp. 405–408, 2001.

[58] S. Gatz and J. Herrmann, "Soliton Collision and Soliton Fusion in Dispersive Linear and Quadratic Intensity Refraction Index Change," *IEEE J. Quantum Electron.*, vol. 28, no. 7, pp. 1732–1738, 1992.

[59] C. Dai and C. Liu, "Solitary wave fission and fusion in the (2+1)-dimensional generalized Broer-Kaup system," *Nonlinear Analysis: Modelling and Control*, vol. 17, no. 3, pp. 271–279, 2012.

[60] C. Rotschild, B. Alfassi, O. Cohen, and M. Segev, "Long-range interactions between optical solitons," *Nature Physics*, vol. 21, pp. 769–774, 2006.

[61] J. Pfeiffer, M. Schuster, A. A. Abdumalikov, Jr., and A. V. Ustinov, "Observation of Soliton Fusion in a Josephson Array," *Phys. Rev. Lett.*, vol. 96, 034103, 2006.

[62] C. Zheng and L. Chen, "Solitons with fission and fusion behaviors in a variable coefficient Broer-Kaup system," *Chaos, Solitons and Fractals*, vol. 24, pp. 1347–1351, 2005.

[63] W. Krolikowski and S. A. Holmstrom, "Fusion and birth of spatial solitons upon collision," *Opt. Lett.*, vol. 22, no. 6, pp. 369–371, 1997.

[64] A. I. Konyukhov, M. A. Dorokhova, L. A. Melnikov, and A. S. Plastun, "Inelastic collision and fusion of optical solitons in dispersion oscillating fiber," *Laser Phys. Lett.*, vol. 12, 055103, 2015.

[65] S. R. Friberg, "Soliton fusion and steering by the simultaneous launch of two different-color solitons," *Opt. Lett.*, vol. 16, no. 19, pp. 1484–1486, 1991.

[66] A. Hasegawa and F. Tappert, "Transmission of stationary nonlinear optical pulses in dispersive dielectric fibers. I. anomalous dispersion," *Appl. Phys. Lett.*, vol. 23, no. 3, pp. 142–144, 2010.

[67] Y. Kodama, A. Maruta, and A. Hasegawa, "Long distance communications with solitons," *Quantum Opt.*, vol. 6, no. 6, pp. 463–516, 1994.

[68] P. V. Mamyshev and L. F. Mollenauer, "Soliton collisions in wavelength-division-multiplexed dispersion-managed systems," *Opt. Lett.*, vol. 24, no. 7, pp. 448–450, 1999.

[69] H. Sugahara, H. Kato, T. Inoue, A. Maruta, and Y. Kodama, "Optimal dispersion management for a wavelength-division-multiplexed optical soliton transmission system," *IEEE/OSA J. Lightwave Technol.*, vol. 17, no. 9, pp. 1547–1559, 1999.

[70] D. J. Kaup, B. A. Malomed, and J. Yang, "Interchannel pulse collision in a wavelength division multiplexed system with strong dispersion management," *Opt. Lett.*, vol. 23, no. 20, pp. 1600–1602, 1999.

[71] A. Maruta, Y. Nonaka, and T. Inoue, "Symmetric Bi-Soliton solution in a dispersion-managed system," *Electron. Lett.*, vol. 37, no. 22, pp. 1357–1358, 2001.

[72] J. Satsuma and N. Yajima, "Initial value problems of one-dimensional self-modulation of nonlinear waves in dispersive media," *Prog. Theor. Phys. Suppl.*, no. 55, pp. 284–306, 1974.

[73] G. B. Whitham, "Nonlinear dispersive waves," *Proc. Roy. Soc.*, vol. 283, no. 1393, pp. 238–261, 1965.

[74] L. A. Ostrovskii and E. Yakubovich, "Averaged laser equations and their stationary solutions," *Sov. Phys. Tech. Phys.*, vol. 46, no. 3, pp. 963–969, 1964.

[75] V. I. Bespalov and V. I. Talanov, "Filamentary Structure of Light Beams in Nonlinear Media," *JETP Lett.*, vol. 3, no. 3, pp. 307–309, 1966.

[76] V. I. Karpman, "Self-modulation of Nonlinear Plane Waves in Dispersive Media," *JETP Lett.*, vol. 6, no. 3, pp. 277–279, 1967.

[77] A. Mussot, A. Kudlinski, M. Kolobov, E. Louvergneaux, M. Douay, and M. Taki, "Observation of extreme temporal events in CW-pumped supercontinuum," *Opt. Express*, vol. 17, no. 19, pp. 17010–17015, 2009.

[78] A. Hasegawa and Y. Kodama, *Solitons in Optical Communications*, Oxford University Press, 1995.

[79] J. M. Soto-Crespo, N. Devine, and N. Akhmediev, "Integrable Turbulence and Rogue waves: Breathers or Solitons?," *Phys. Rev. Lett.*, vol. 116, 103901, 2016.

[80] V. E. Zakharov and A. B. Shabat, "Interaction between solitons in a stable medium," *Sov. Phys. JETP*, vol. 37, no. 5, pp. 62–69, 1972.

[81] M. J. Ablowitz and P. A. Clarkson, *Solitons, Nonlinear Evolution Equations, and Inverse Scattering*, Cambridge University Press, New York, 1991.

[82] V. V. Voronovich, V. I. Shrira, and G. Thomas, "Can bottom friction suppress freak wave formation?," *J. Fluids Mech.*, vol. 604, pp. 263–296, 2008.

[83] M. J. Ablowitz and H. Segur, *Solitons and the Inverse Scattering Transform*, SIAM, Philadelphia, 1981.

[84] M. J. Ablowitz, D. J. Kaup, A. C. Newell, and H. Segur, "The inverse scattering transform-Fourier analysis for nonlinear problems," *Stud. Appl. Math.*, vol. 53, pp. 249–315, 1974.

[85] J. R. Taylor, Eds., *Optical Solitons Theory and Experiment*, Cambridge University Press, New York, 1992.

[86] V. E. Zakharov and A. B. Shabat, "Exact theory of two-dimensional self-focusing and one-dimensional self-modulation of waves in nonlinear media," *Sov. Phys. JETP*, vol. 34, no. 1, pp. 118–134, 1972.

[87] Y. Kodama, M. Romagnoli, S. Wabnitz, and M. Midrio, "Role of third-order dispersion on soliton instabilities and interactions in optical fibers," *Opt. Lett.*, vol. 19, no. 3, pp. 165–167, 1994.

[88] Y. Kodama, "Optical Solitons in a Monomode Fiber," *J. Stat. Phys.*, vol. 39, pp. 597–614, 1985.

[89] Y. Kodama and A. Hasegawa, "Nonlinear pulse propagation in a monomode dielectric guide," *IEEE J. Quantum Electron.*, vol. QE-23, no. 5, pp. 510–524, 1987.

[90] J. M. Soto-Crespo, N. Devine, N. P. Hoffmann, and N. Akhmediev, "Double peak rogue waves of the Sasa-Satsuma equation in a chaotic wave field," *Proc. of Advanced Photonics*, JM5A.47, 2014.

[91] G. Weerasekara and A. Maruta, "Characterization of optical rogue wave based on solitons' eigenvalues of the integrable higher-order nonlinear Schrödinger equation.," Opt. Commun., vol. 382, pp. 639–645, 2017.

[92] D. W. Jordan and P. Smith, *Nonlinear Ordinary Differential Equations*, Oxford University Press, 1999.

[93] J. P. Gordan, "Interaction forces among solitons in optical fibers," *Opt. Lett.*, vol. 8, no. 11, pp. 596–598, 1983.

[94] A. Hasegawa and Y. Kodama, "Guiding-center soliton in optical fibers," *Opt. Lett.*, vol. 15, no. 24, pp. 1443–1445, 1990.

[95] A. C. Newell, *Topics in Current Physics*, Springer-Verlag, 1980.

[96] C. S. Gardner, J. M. Green, M. D. Kruskal, and R. M. Miura, "Method for solving the Korteweg-de Vries equation," *Phys. Rev. Lett.*, vol. 19, pp. 1095–1097, 1967.

[97] P. D. Lax, "Integrals of nonlinear equations of evolution and solitary waves," *Comm. Pure Appl. Math.*, vol. 21, pp. 467–490, 1968.

[98] M. Wadati, "The modefied Korteweg-de Vries equation," *J. Phys. Soc. Japan*, vol. 34, no. 5, pp. 1289–1296, 1973.

[99] Y. Kodama and M. J. Ablowitz, "Perturbation of solitons and solitary waves," *Stud. Appl. Math.*, vol. 64, no. 3, pp. 225–245, 1981.

Acronyms

AB	Akhmediev breather
CCDF	complementary cumulative distribution function
CW	continuous wave
DSF	dispersion shifted fiber
EDF	erbium doped fiber
GVD	group velocity dispersion
HNLSE	higher-order nonlinear Schrödinger equation
IOS	intensive optical isolator
MI	modulational instability
MLL	mode locked laser
NLSE	nonlinear Schrödinger equation
OC	output coupler
PBS	polarization beam splitter
PC	polarization controller
PD	photo detector
PDF	probability density function
SC	supercontinuum
SMF	single mode fiber
SPM	self-phase modulation
SSFM	split-step Fourier method
SWH	significant wave height

List of Publications

I. Peer-reviewed Journals

1. Gihan Weerasekara, Akihiro Tokunaga, Hiroki Terauchi, Marc Eberhard, and Akihiro Maruta, "Soliton's eigenvalue based analysis on the generation mechanism of rogue wave phenomenon in optical fibers exhibiting weak third order dispersion," *Opt. Express*, vol. 23, no. 1, pp. 143–153, Jan. 2015.

2. Gihan Weerasekara and Akihiro Maruta, "Characterization of optical rogue wave based on solitons' eigenvalues of the integrable higher-order nonlinear Schrödinger equation," *Opt. Commun.*, vol. 382, pp. 639–645, Jan. 2017.

II. Peer-reviewed International Conferences

1. Koji Morita, Gihan Weerasekara, Takahiro Kodama, Satoshi Shimizu, Naoya Wada, and Ken-ichi Kitayama, "Massive/Recognition of 2-D Label Using Optical Code and Wavelength," in *Proc. on Optoelectronics and Communications Conference and Photonics in Switching (OECC/PS 2013)*, Kyoto, Japan, MT2-4, July 2013.

2. Gihan Weerasekara, Akihiro Tokunaga, Hiroki Terauchi, Marc Eberhard, and Akihiro Maruta, "Analysis of Rogue Wave Phenomenon based on Soliton's Eigenvalue," in *Proc. Nonlinear Photonics*, Barcelona, Spain, July 2014.

3. Gihan Weerasekara and Akihiro Maruta, "The eigenvalue based analysis of rogue wave phenomena in the frame work of integrable higher-order nonlinear Schrödinger equation," in *Proc. Nonlinear Optics*, Hawaii, USA, July 2015.

4. Gihan Weerasekara and Akihiro Maruta, "Characterization of soliton fusion phenomenon based on solitons' eigenvalue," in *Proc. 21st Optoelectronics and Communications Conference / International Conference on Photonics in Switching 2016 (OECC/PS 2016)*, Niigata, Japan, July 2016.

III. Domestic Conferences

1. Gihan Weerasekara, Yuki Yoshida, and Ken-ichi Kitayama, "Experimental Demonstration of 1×2 Switching of Fixed-length Variable-capacity OFDM Payload Packet," in *IEICE Technical Committee on Photonic Network*, Student Workshop, Kitami Institute of Technology, Japan, Aug. 2012.

2. Gihan Weerasekara, Akihiro Tokunaga, Hiroki Terauchi, Akihiro Maruta, and Marc Eberhard, "Analysis of Rogue wave phenomenon in Optical Fiber Based on Soliton Theory," in *IEICE General Conf.*, B-10-8, Niigata, Japan, March 2014.

3. Gihan Weerasekara, Akihiro Tokunaga, Hiroki Terauchi, Akihiro Maruta, and Marc Eberhard, "Analysis of Rogue Wave Phenomenon in Optical Fiber Based on Soliton's Eigenvalue," in *IEICE Technical Committee Meeting on Optical Communication Systems*, OCS 2014-22, Oita, Japan, June 2014.

4. Gihan Weerasekara and Akihiro Maruta, "Analysis of Rogue Wave Phenomenon in Optical Fiber Based on Soliton's Eigenvalue," in *IEICE Optical Communication Systems Symposium*, P-5, Mishima, Japan, Dec. 2015.

5. Gihan Weerasekara and Akihiro Maruta, "Analysis of Rogue Wave Phenomenon in Optical Fiber Based on Soliton's Eigenvalue," in *IEICE General Conf.*, B-10-74, Kyushu, Japan, March 2016.

6. Gihan Weerasekara and Akihiro Maruta, "Optical rogue wave generation caused by soliton fusion phenomenon," in *IEICE Technical Committee Meeting on Photonic Network*, Mie, Japan, Jan. 2017.

Short Biography

Gihan Weerasekara was born on Sep. 16, 1986 in Kandy, Sri Lanka. He received his B.Sc. degree from the Department of Electronic and Information Engineering, Faculty of Engineering, Osaka University, Japan in 2012. He received his M.E. degree from the Department of Electrical, Electronic and Information Engineering, Graduate School of Engineering, Osaka University, Japan in 2014, after which he started work to earn his Ph.D. degree in Information and Communications Technology from the Graduate School of Engineering, Osaka University, Japan. In 2007, he was selected as a scholar of the Ministry of Education, Culture, Sports, Science, and Technology (MEXT) in Japan. His research interests include nonlinear optics, photonic label processing, optical packet switching network, and digital signal processing.